THE EFFECTS OF SAMPLING, RECONSTRUCTION, AND T_2 MODULATION FOR POLAR K-SPACE ACQUISITIONS IN MAGNETIC RESONANCE IMAGING

by

M. Louis Lauzon
Department of Medical Biophysics

Submitted in partial fulfillment
of the requirements for the degree of
Doctor of Philosophy

Faculty of Graduate Studies
The University of Western Ontario
London, Ontario
February 1998

Abstract

Magnetic resonance imaging is a powerful imaging modality whereby tissue can be characterized according to various contrast mechanisms, most notably T_2-weighted contrast. The T_2-weighted images are very useful clinically, but the major disadvantage is that these high-quality images often require long imaging times.

The Cartesian RARE-mode acquisition proposed by Hennig retains the soft-tissue contrast-to-noise ratio (CNR) and signal-to-noise ratio (SNR) of conventional T_2-weighted images, but at a reduced acquisition time. Moreover, non-Cartesian sampling schemes offer further advantages in motion and flow artifact suppression, and efficient use of gradients.

In this treatise, the viability of T_2-weighted polar **k**-space sampling acquisitions is assessed and compared for projection reconstruction (PR-MRI) and concentric circles (CC-MRI). We analyze the fundamental aspects including sampling and image reconstruction effects such as aliasing, resolution, and SNR, and we investigate the T_2-weighting contrast of PR-MRI and CC-MRI when imaging in RARE-mode.

The Fourier aliasing effects of uniform polar sampling are explained from the 2D principal point spread function (PSF). This is determined by assuming equally-spaced concentric rings in **k**-space. The 2D polar effects such as replication, smearing, truncation artifacts, and sampling requirements are characterized.

Although the 2D polar sampling PSF leads to some subtle aliasing effects and artifacts, these effects can be suppressed depending on the choice of reconstruction algorithm one uses. For uniform polar sampling, both gridding (GRD) and convolution backprojection (CBP) are applicable. The respective strengths and weaknesses

of these algorithms are analyzed, compared, and discussed. Provided that the image resolution and the SNR are considered together, these algorithms perform similarly. But, their aliasing behaviour is different because GRD is a 2D Fourier inversion algorithm, whereas CBP is based upon a 1D Fourier inversion.

The effective echo times (TE) and resulting T_2 contrast curves of RARE-mode PR-MRI and CC-MRI are derived. The effective TE of RARE-mode PR-MRI is shown to be highly dependent on T_2, the echo spacing (ESP), and the echo train length (ETL). By comparison, the effective TE of RARE-mode CC-MRI is not nearly as sensitive to ESP and ETL, especially for large objects within the field of view.

Finally, we propose a novel yet general method of correcting for the T_2 modulation effects of RARE-mode sequences to allow the acquisition of high SNR, high CNR, properly T_2-weighted images.

Keywords: polar k-space, principal point spread function, gridding and convolution backprojection reconstruction, resolution, SNR, aliasing, and T_2 modulation

To my family and friends for always believing in me,
supporting me, encouraging me when I needed it most,
and for giving me the strength to persevere with my studies.

Acknowledgements

Although graduate studies is a long journey, one does not travel alone. Many kind and helpful souls have guided and aided me along the way. I wish to acknowledge their help and support throughout the many years.

First, I wish to thank my supervisor Dr. Brian K. Rutt who took me under his wing and taught me the fundamentals of MRI and signal processing. His patience, nurturing, and encouragement throughout enabled me to complete this degree. Under his tutelage, I honed my scientific writing abilities, a much-needed skill.

Secondly, I'd like to pay homage to the people of the University of Western Ontario (UWO) Medical Biophysics Department, of the JP Robarts Research Imaging Labs, and of the University Hospital Radiology Department. Not wanting to omit or overlook anyone, I would simply like to extend my thanks and gratitude to all who (1) helped me with experimental and theoretical developments, (2) helped me with computer software and hardware issues, (3) helped me prepare seminars, talks, posters, and papers, (4) taught me anything and everything about anything, (5) gave me encouragement, and (6) shared life's little secrets with me.

Needless to say, many thanks are extended to those who provided financial support, in particular the Natural Sciences and Engineering Research Council of Canada, the Medical Research Council of Canada, and the UWO Faculty of Graduate Studies and Medical Biophysics Department.

Finally, I wish to thank my family and friends who always believed in me and encouraged me to better myself as a scientist, a researcher, and a person. Without their help, thoughts, and timely advice, I would not be where I am today.

Contents

Certificate of Examination ii

Abstract iii

Acknowledgements vi

Table of Contents vii

List of Tables ix

List of Figures x

1 Introduction **1**
1.1 Brief MR History 1
1.2 Background Theory 2
1.2.1 Signal Equation 2
1.2.2 Fourier Theory 5
1.3 Polar Sampling 9
1.3.1 Historical Perspective 9
1.3.2 Projection Slice Theorem 10
1.3.3 Projection Reconstruction 11
1.3.4 Concentric Circles and Spirals 13
1.4 Research Goal 15
1.5 Thesis Overview 16
1.6 References 18

2 Sampling Effects **24**
2.1 Introduction 24
2.2 Theory 26
2.2.1 Weighting of δ-Functions 27
2.2.2 Ring Samples and the Principal Polar PSF 30
2.3 Results 37
2.3.1 Polar PSF Intuition 38
2.3.2 Radial Aliasing Effects 41
2.4 Discussion 50
2.5 References 53

3 Reconstruction Effects **56**
3.1 Introduction 56
3.2 Theory 58
3.2.1 Gridding 58
3.2.2 Convolution Backprojection 66
3.3 Tradeoffs 73
3.4 Results 76
3.5 Non-Equidistant k_r Sampling 80
3.6 Discussion 85
3.7 Appendices 87
3.7.1 App. A - CBP Integral 87
3.7.2 App. B - CBP MTF 89
3.8 References 93

4 T_2 Modulation Effects **96**
4.1 Introduction 96
4.2 Theory 98
4.2.1 Projection Reconstruction 103
4.2.2 Concentric Circles 116
4.3 Results 132
4.3.1 Projection Reconstruction 132
4.3.2 Concentric Circles 137
4.3.3 In Vivo Comparison 142
4.4 Discussion 144
4.5 Appendix 146
4.5.1 Effective TE for Cartesian RARE-Mode 146
4.6 References 153

5 Conclusions and Discussion **154**
5.1 Sampling Effects 155
5.2 Reconstruction Effects 157
5.3 T_2 Modulation Effects 159
5.4 Future Perspectives 161
5.5 References 166

Glossary **167**

Vita **169**

List of Tables

1.1 Basic Fourier transform theorems 6

2.1 Energy components of synthetic disk phantoms 49

3.1 Theoretical variance and SNR values for GRD and CBP 71
3.2 Agarose/$NiCl_2$ phantom T_1 and T_2 values 76
3.3 Experimental SNR measurements relative to a ±32kHz filter 78
3.4 Experimental noise measurements relative to an 11cm FOV 79
3.5 Experimental SNR measurements of CBP relative to GRD 79

4.1 PR-MRI signal intensity fraction verification (Tubes 1–3) 135
4.2 PR-MRI signal intensity fraction verification (Tubes 4–6) 135
4.3 PR-MRI signal intensity fraction verification (Tubes 7–9) 136
4.4 CC-MRI signal intensity fraction verification (Tubes 1–3) 140
4.5 CC-MRI signal intensity fraction verification (Tubes 4–6) 140
4.6 CC-MRI signal intensity fraction verification (Tubes 7–9) 141

List of Figures

2.1 K-space sampling rings 31
2.2 Principal polar PSF profile 32
2.3 Normalized principal polar PSF main lobe $s_0(r)$ 34
2.4 Normalized principal polar PSF ringlobe $s_j(r)$ 35
2.5 Normalized Cartesian PSF 38
2.6 Synthetic disk phantom aliasing 42
2.7 Synthetic elliptical phantom aliasing 44
2.8 Synthetic two-disk phantom aliasing 46
2.9 Principal polar PSF arising from the ringlobes only 48

3.1 Synthetic, uniform disk profiles using GRD and CBP 64
3.2 Convolution backprojection MTFs 69
3.3 Polar k-space sampling trajectories 82
3.4 Synthetic, noise-free, phantom images 83
3.5 Comprehensive development of the CBP MTF 91

4.1 Conventional spin echo k-space representation 101
4.2 RARE-mode spin echo k-space representation 102
4.3 PR-MRI T_2-weighted banding approach 103
4.4 PR-MRI T_2 impulse response function for the banding approach . . . 104
4.5 PR-MRI image reconstruction effect for the banding approach 105
4.6 PR-MRI T_2-weighted sequential approach 105
4.7 PR-MRI T_2 impulse response function for the sequential approach . . 106
4.8 PR-MRI image reconstruction effect for the sequential approach . . . 107
4.9 PR-MRI T_2-weighted interleaved approach 107
4.10 PR-MRI T_2 impulse response function for the interleaved approach . 108
4.11 PR-MRI image reconstruction effect for the interleaved approach . . 109
4.12 PR-MRI signal intensity fraction curves 111
4.13 PR-MRI signal intensity fraction synthetic phantom images 112
4.14 PR-MRI effective TE curves 113
4.15 PR-MRI effective signal intensity curves 115
4.16 CC-MRI T_2-weighted banding approach 116
4.17 CC-MRI T_2 impulse response function for the banding approach . . . 117
4.18 CC-MRI image reconstruction effect for the banding approach 118
4.19 CC-MRI T_2-weighted smoothly decaying approach 119
4.20 CC-MRI T_2 impulse response function for the smooth approach . . . 120

4.21 CC-MRI image reconstruction effect for the smooth approach 121
4.22 CC-MRI T_2-weighted non-monotonic approach 122
4.23 CC-MRI image reconstruction effect for the non-monotonic approach 122
4.24 CC-MRI signal intensity fraction curves 125
4.25 CC-MRI signal intensity fraction N_r dependence 126
4.26 CC-MRI signal intensity fraction synthetic phantom images 127
4.27 CC-MRI effective TE curves 129
4.28 CC-MRI effective signal intensity curves 131
4.29 PR-MRI T_2 tube phantom images for ETL={1,4,8} echoes 134
4.30 Stimulated echo artifact of CC-MRI acquisition 137
4.31 CC-MRI T_2 tube phantom images for ETL={1,4,8} echoes 139
4.32 Cartesian, PR-MRI, and CC-MRI head images for ETL={1,8} echoes 143
4.33 SW-MRI signal intensity fraction curves 147
4.34 SW-MRI effective TE curves 150
4.35 SW-MRI effective signal intensity curves 152

5.1 Synthetic conventional SE and RARE-mode SW-MRI images 163
5.2 Isolated T_2 species from two RARE-mode acquisitions 164

Chapter 1

Introduction

1.1 Brief MR History

Nuclear magnetic resonance (NMR) was first observed in 1945 by two independent groups, one being the Stanford research group headed by Bloch [1], and the other being the Masachusetts Institute of Technology (MIT) research group under the leadership of Purcell [2]. Their pioneering achievements were recognized in 1952, for which both Bloch and Purcell shared the 1952 Nobel Prize in Physics.

From 1946 onwards, NMR became a viable and useful tool in probing the chemical composition of materials. Although a comprehensive explanation of the theory of NMR is beyond the scope of this treatise, many books have been written on the subject, among them the two "bibles of NMR" by Slichter [3] and Abragam [4].

In 1973, the State University of New York at Stony Brook research group headed by Lauterbur succeeded in forming images using NMR [5]. They realized that because the resonant frequency is proportional to the magnetic field strength, a magnetic field *gradient* yields multiple resonant frequencies, each one corresponding to a *spatial* location in the imaging field of view (FOV).

Since its inception in 1973, there have been numerous studies and advancements in the field of MR imaging (MRI). In fact, the progress has been so rapid that a complete bibliographic listing is not feasible here. However, for an in-depth historical review of MRI, the textbooks by Morris [6] and Brey [7] prove to be very informative.

1.2 Background Theory

Unlike most other imaging modalities modalities, MRI data acquisition occurs in Fourier space, and the image is calculated from the inverse Fourier transform. Fourier theory, then, plays an important role in understanding MRI image effects.

In this section, the MRI signal equation is developed which shows the explicit Fourier nature of MRI. Furthermore, some basic yet useful concepts of Fourier theory are presented.

1.2.1 Signal Equation

Let us first review the underlying theory of MRI. The governing phenomenological equations that describe magnetic resonance are the Bloch Equations [8], namely

$$\frac{d\mathbf{m}}{dt} = \gamma(\mathbf{m}\times\mathbf{B}) - \frac{m_x}{T_2}\hat{x} - \frac{m_y}{T_2}\hat{y} + \frac{m_o - m_z}{T_1}\hat{z} \tag{1.1}$$

where $\mathbf{B} = (B_x, B_y, B_z)$ is the magnetic field strength, $\mathbf{m} = (m_x, m_y, m_z)$ is the magnetization spin-density, m_o is the equilibrium magnetization spin-density along the z-axis, γ is the gyromagnetic ratio, T_1 is the spin-lattice relaxation time constant, *i.e.* the characteristic time of regrowth back to equilibrium in the z-direction, and T_2 is the spin-spin relaxation time constant, *i.e.* the characteristic time of dephasing of the magnetization in the transverse plane. Note that $\mathbf{m}$, $\mathbf{B}$ and their corresponding components are functions of space and time, whereas m_o, T_1, and T_2 are functions of space only.

In 1956, Torrey [9] adapted the Bloch equations to include diffusion effects, and in 1965 Stejskal [10] included velocity effects in the so-called modified Bloch-Torrey equations, namely

$$\frac{d\mathbf{m}}{dt} = \gamma(\mathbf{m}\times\mathbf{B}) - \frac{m_x}{T_2}\hat{x} - \frac{m_y}{T_2}\hat{y} + \frac{m_o - m_z}{T_1}\hat{z} - (\nabla\cdot\mathbf{v})\,\mathbf{m} + \nabla\cdot\mathbf{D}\cdot\nabla\mathbf{m} \tag{1.2}$$

where $\mathbf{v}$ and $\mathbf{D}$ represent the velocity vector and diffusion tensor, respectively. In this treatise, however, we will not concern ourselves with diffusion or velocity, but

will focus primarily on sampling effects and T_2 modulation effects. Therefore, the signal equation is derived from Eq.(1.1) only. The expansion of Eq.(1.1) into its components describes the temporal evolution of the magnetization:

$$\begin{aligned}
\frac{dm_x}{dt} &= \gamma\,(m_y B_z - m_z B_y) - \frac{m_x}{T_2} \\
\frac{dm_y}{dt} &= \gamma\,(m_z B_x - m_x B_z) - \frac{m_y}{T_2} \\
\frac{dm_z}{dt} &= \gamma\,(m_x B_y - m_y B_x) + \frac{m_o - m_z}{T_1}
\end{aligned} \tag{1.3}$$

In MR, we are interested in both the *longitudinal* and *transverse* components of the magnetization vector. We define them as follows, where the spatial and temporal dependences are given explicitly:

$$\begin{aligned}
\mathbf{m}_{long} &\equiv m_z(\mathbf{r},t) \\
\mathbf{m}_{trans} &\equiv m_{xy}(\mathbf{r},t) = m_x(\mathbf{r},t) + i\,m_y(\mathbf{r},t)
\end{aligned} \tag{1.4}$$

where $i=\sqrt{-1}$. After the radiofrequency (RF) pulse has been turned off, the magnetic field strength components are $B_x=0$, $B_y=0$, and $B_z(\mathbf{r},t)=B_o+\Delta B_z(\mathbf{r})+\mathbf{G}(t)\cdot\mathbf{r}$, where B_o is the DC magnetic field strength, $\Delta B_z(\mathbf{r})$ are z-directional field inhomogeneities, and $\mathbf{G}(t)=(G_x,G_y,G_z)$ is the time-dependent gradient field necessary for spatial localization. By specifying the initial conditions of the magnetization after the RF pulse as $m_{xy}(\mathbf{r},0)=m^o_{xy}(\mathbf{r})$ and $m_z(\mathbf{r},0)=m^o_z(\mathbf{r})$, we find

$$m_z(\mathbf{r},t) = m_o(\mathbf{r}) + \left(m^o_z(\mathbf{r}) - m_o(\mathbf{r})\right)\epsilon^{-t/T_1(\mathbf{r})} \tag{1.5}$$

$$m_{xy}(\mathbf{r},t) = m^o_{xy}(\mathbf{r})\,\epsilon^{-t/T_2(\mathbf{r})}\,\epsilon^{-i\gamma B_o t}\epsilon^{-i\gamma\Delta B_z(\mathbf{r})\,t}\,\epsilon^{-i\gamma\int_t \mathbf{G}(\tau)\,d\tau\cdot\mathbf{r}} \tag{1.6}$$

Eq.(1.5) is simple and straightforward. It describes the regrowth of m_z from its initial value of $m^o_z(\mathbf{r})$ at time $t=0$ back to its equilibrium value of $m_o(\mathbf{r})$ as $t\rightarrow\infty$. Note that there is no phase modulation of m_z during its temporal evolution.

In Eq.(1.6), the ϵ^{-t/T_2} term describes an amplitude modulation (T_2 decay), while all other exponential terms describe a phase modulation. More specifically, the phase factor $\epsilon^{-i\gamma B_o t}$ describes the oscillatory (or precessional) behaviour of the transverse

magnetization about the z-axis at the Larmor frequency γB_o. The term $e^{-i\gamma\Delta B_z(\mathbf{r})t}$ imposes a position-dependent precessional perturbation (*i.e.* an off-resonance) effect on the magnetization. Finally, by defining $\mathbf{k}(t)=\frac{\gamma}{2\pi}\int_t \mathbf{G}(\tau)\,d\tau$, the last term can be written as $e^{-2\pi i\,\mathbf{k}\cdot\mathbf{r}}$ which, as it turns out, is the Fourier kernel.

The above model is correct for liquid-like systems, but not for solids. Since biological systems consist of about 80% water and solids do not contribute much signal due to very short T_2, this model is adequate for MRI purposes.

Now, the *acquired* signal (say M) is actually the *sum* of the transverse magnetization at all positions *within* the excited region (as determined by the RF coil). If we demodulate the acquired signal at the Larmor frequency, which effectively amounts to multiplying by the phase factor $e^{+i\gamma B_o t}$, then

$$\begin{aligned} M(\mathbf{k},t) &= \int_{-\infty}^{+\infty} m_{xy}^{o}(\mathbf{r})\, e^{-t/T_2(\mathbf{r})}\, e^{-i\gamma\Delta B_z(\mathbf{r})\,t}\, e^{-2\pi i\mathbf{k}\cdot\mathbf{r}}\, d\mathbf{r} \\ &= \mathcal{F}\left\{ m_{xy}^{o}(\mathbf{r})\, e^{-t/T_2(\mathbf{r})}\, e^{-i\gamma\Delta B_z(\mathbf{r})\,t} \right\} \end{aligned} \tag{1.7}$$

where $\mathcal{F}$ is the Fourier transform (FT) operator since $e^{-2\pi i\,\mathbf{k}\cdot\mathbf{r}}$ is the Fourier kernel. This is the MRI *signal equation* which defines the acquired data in terms of the spatial frequencies in Fourier space, more commonly known as **k**-space. The MR image, $I(\mathbf{r})$, is then calculated from the inverse Fourier transform (IFT) of $M(\mathbf{k},t)$, namely

$$I(\mathbf{r}) = \mathcal{F}^{-1}\left\{ M(\mathbf{k},t) \right\} \tag{1.8}$$

$M(\mathbf{k},t)$ and $I(\mathbf{r})$ form an FT pair and depict the current formalism in MRI: (1) acquire the data in **k**-space, and (2) take the IFT to reconstruct the MR image.

The MR image characteristics will depend on the magnetization spin-density $m_{xy}^{o}(\mathbf{r})$, on $T_2(\mathbf{r})$, and on the off-resonance $\Delta B_z(\mathbf{r})$ as evidenced by Eqs.(1.7,1.8). Also, from Eqs.(1.3), we see that m_x, m_y, and m_z are coupled so that the transverse magnetization also bears $T_1(\mathbf{r})$ information. Consequently, the reconstructed MR image characteristics will also depend on $T_1(\mathbf{r})$.

1.2.2 Fourier Theory

As shown in the previous section, the MRI acquisition process occurs in Fourier space, and one must transform to the image domain via the IFT. Fourier theory, then, is the cornerstone of MRI image reconstruction.

Although many books have been written on the various topics of Fourier analysis and theory, this section merely touches on the more important aspects of Fourier transforms. The reader is referred to Papoulis [11] and/or Bracewell [12] for an in-depth analysis of continuous Fourier theory, and to Brigham [13] for the discrete Fourier transform theory.

Fourier Integral

The Fourier transform of the one-dimensional (1D) function $f(x)$ is given as $F(k_x)$. These are defined as

$$F(k_x) = \int_{-\infty}^{+\infty} f(x)\, e^{-2\pi i x k_x}\, dx, \quad f(x) = \int_{-\infty}^{+\infty} F(k_x)\, e^{+2\pi i x k_x}\, dk_x \qquad (1.9)$$

The $e^{\pm 2\pi i x k_x}$ term is the Fourier transformation kernel and represents the complex sinusoid $\cos(2\pi x k_x) \pm i \sin(2\pi x k_x)$. Now, $f(x)$ and $F(k_x)$ are a Fourier transform pair, where x and k_x are Fourier conjugates. For x in units of length, k_x is in units of reciprocal length, often termed the spatial frequency.

Clearly, one can generalize the above integrals to multiple dimensions. For example, in 3D $f(x, y, z)$ transforms to $F(k_x, k_y, k_z)$ according to

$$F(k_x, k_y, k_z) = \int_{-\infty}^{+\infty} \int_{-\infty}^{+\infty} \int_{-\infty}^{+\infty} f(x, y, z)\, e^{-2\pi i [x k_x + y k_y + z k_z]}\, dx dy dz \qquad (1.10)$$

Furthermore, we do not necessarily have to restrict ourselves to Cartesian coordinates. One can transform either (x, y, z) or (k_x, k_y, k_z) or both to different coordinate systems, whereby Eq.(1.10) adopts a new form. For example, one can transform to polar coordinates to gain further insight into the aspects of polar sampling.

Fourier Theorems

The power of Fourier theory lies in its easily-derived theorems. The theorems (in 1D) are simply stated without derivations, although they can be derived from basic principles and Eq.(1.9). For a more thorough list, the reader is referred to Chapter 6 of Bracewell [12].

Table 1.1: Basic Fourier transform theorems

Theorem	$f(x)$	$F(k_x)$
Scaling	$f(ax)$	$\frac{1}{\|a\|} F\left(\frac{k_x}{a}\right)$
Addition	$f(x)+g(x)$	$F(k_x)+G(k_x)$
Shift	$f(x-a)$	$e^{-2\pi i a k_x} F(k_x)$
Convolution	$f(x) \star g(x)$	$F(k_x)\,G(k_x)$

Parseval	$\int_{-\infty}^{+\infty} \|f(x)\|^2\,dx = \int_{-\infty}^{+\infty} \|F(k_x)\|^2\,dk_x$

The theorems of Table 1.1 can easily be generalized to multiple dimensions. They are used throughout this treatise.

Discrete Fourier Theory

In general, one does not measure the continuous (*i.e.* analog) signal $f(x)$, but rather a sampled (*i.e.* digital) signal, say $f_s(x)$, which is a discrete representation of $f(x)$. Mathematically, we can express this discretization as the multiplication of the continuous signal with a sampling function $s(x)$ consisting of a series of impulse functions, often called δ-functions. For example, if $f(x)$ is sampled at P locations, then

$$\begin{aligned} f_s(x) &= f(x)\,s(x) = f(x)\sum_{p=1}^{P}\delta(x-x_p) = \sum_{p=1}^{P} f(x_p)\,\delta(x-x_p) \\ &= \left\{f(x_1), f(x_2), \ldots, f(x_P)\right\} \end{aligned} \tag{1.11}$$

One clearly sees the discrete nature of $f_s(x)$ owing to the sifting property of the δ-function. *i.e.* $\int_a^b f(x)\,\delta(x-x')\,dx = f(x')$ if $a < x' < b$. Using the Fourier convolution theorem from Table 1.1, we obtain

$$F_s(k_x) \;=\; F(k_x) \star S(k_x) \;=\; \int_{-\infty}^{+\infty} F(u)\,S(k_x - u)\,du \qquad (1.12)$$

where $F(k_x)$ and $S(k_x)$ are the FTs of $f(x)$ and $s(x)$, respectively, and $\star$ represents the convolution operation. Convolution is simply this: (1) take the mirror image of one of the functions, (2) slide this mirrored function to position u, (3) multiply this with the un-mirrored function, and (4) calculate the area. This gives one value (at position u) of the convolution integral. To get the full curve, repeat steps 1–4 for all possible u locations.

One must recognize that the convolution operation is a "smearing" operation since $F(k_x)$ is possibly smoothed and/or blurred and/or replicated depending on the functional form of $S(k_x)$. In other words, the process of sampling *affects* the overall appearance of the reconstructed function. Note that convolution with a single δ-function returns the original function centred on that δ-function, and so no blurring or replication occurs. But, since the Fourier conjugate of a δ-function is a constant extending over all space, this is the same as having sampled continuously over an infinite extent, which is impractical.

In practice, one samples only a finite number of points. This can be thought of as multiplying a function of infinite extent with some truncation window. And, since multiplication in one domain engenders convolution in the other, we see that finite extent sampling may corrupt the true signal: this is called a truncation artifact.

The above effects are very well known in the case of Cartesian sampling, as expounded upon by Brigham [13]. For a historical perspective, the reader is referred to the original Nyquist paper of 1928 [14] which describes the aliasing (replication) phenomenon. To prevent aliasing, Nyquist stated that "the sampling rate must be at least twice as large as the largest frequency component". The reader is forewarned that the above-mentioned definition of the Nyquist criterion applies to Cartesian sam-

pling, but that this definition may not necessarily apply to non-Cartesian sampling. In fact, a generalized Nyquist criterion may not exist in a similar form; consequently, sampling criteria for non-Cartesian acquisitions may be more stringent than those of Cartesian acquisitions.

Note that in MRI, the sampling procedure occurs in **k**-space as opposed to image space. Therefore, blurring, replication, and truncation artifacts show up in the reconstructed image. In summary, the sampling function determines the basic signal processing properties in the resultant image. Using Fourier theory, one can characterize the resolution, signal-to-noise, contrast-to-noise, aliasing, T_1 and T_2 modulations, and off-resonance effects in the reconstructed images. Moreover, because of the flexibility of data acquisition, one may acquire the MR **k**-space data in various non-rectilinear fashions. This allows the possibility of exploring potential advantages and benefits of non-rectilinear Fourier theory and analysis.

1.3 Polar Sampling

In this section, a brief historical perspective of polar sampling is given, and its close relationship to computed tomography is described. Also, a bibliographic review of the salient works on polar sampling in MRI is given.

1.3.1 Historical Perspective

The idea of using linear magnetic field gradients dates back to the early 1950s [15, 16, 17]. However, about 20 years elapsed before Lauterbur [5] and Mansfield [18] independently realized that the NMR signal (often called the free induction decay, or FID) could be encoded with structural information of the spin system by using these same linear magnetic field gradients.

With the theoretical development of section 1.2.1, one can now appreciate the Fourier nature of the spatial encoding process. In the early 1970s, though, this formalism was not yet well established. Nevertheless, Lauterbur reasoned that the (inverse) FT of the collected FID acquired with a linear magnetic field gradient at angle θ represents a *projection* at angle θ through the object being imaged. By varying the projection angle from 0° to 180°, one can generate a complete set of projections through the object in analogy to computed tomography (CT) data.

In MRI the projections are calculated from the inverse Fourier transform of the acquired radial **k**-space lines, while in CT the projections are acquired directly in image space. The projection data can then be reconstructed using the convolution backprojection algorithm, an in-depth review of which is given by Herman [19].

Lauterbur proposed that his imaging technique be called zeugmatography, which was taken from the Greek word zeugma meaning "that which is used for joining". However, the term projection reconstruction MRI (PR-MRI) is probably more appropriate. By use of the projection (or central) slice theorem [20], we next show that PR-MRI and CT data represent **k**-data on a polar grid.

1.3.2 Projection Slice Theorem

The projection slice theorem is most easily understood with an example [21]. The 2D functions $f(x,y)$ and $F(k_x,k_y)$ form an FT pair, whereby

$$F(k_x,k_y) = \int_{-\infty}^{+\infty}\int_{-\infty}^{+\infty} f(x,y)\,e^{-2\pi i[xk_x+yk_y]}\,dxdy \tag{1.13}$$

An arbitrary *projection* of $f(x,y)$ can be obtained by coordinate transformation (*e.g.* a rotation) followed by integration along one of the coordinates. For example, if we integrate along the y-axis and project $f(x,y)$ onto the x-axis (*i.e.* $\theta=0$), then the projection $p_{\theta=0}(x)$ is

$$p_{\theta=0}(x) = \int_{-\infty}^{+\infty} f(x,y)\,dy \tag{1.14}$$

so that its FT pair, $P_{\theta=0}(k_x)=\mathcal{F}\left\{p_{\theta=0}(x)\right\}$, is given by

$$\begin{aligned} P_{\theta=0}(k_x) &= \int_{-\infty}^{+\infty} p_{\theta=0}(x)\,e^{-2\pi ixk_x}\,dx = \int_{-\infty}^{+\infty}\left[\int_{-\infty}^{+\infty} f(x,y)\,dy\right]e^{-2\pi ixk_x}\,dx \\ &= \int_{-\infty}^{+\infty}\int_{-\infty}^{+\infty} f(x,y)\,e^{-2\pi i[xk_x+yk_y]}\,dxdy\Big|_{k_y=0} \\ &= F(k_x,0) \end{aligned} \tag{1.15}$$

The IFT of $P_{\theta=0}(k_x)$ returns the projection $p_{\theta=0}(x)$ given by $\mathcal{F}^{-1}\left\{F(k_x,0)\right\}$. An important property of the Fourier transform is that it preserves orthogonal transformations, including rotations [12]. Thus, the projection of $f(x,y)$ at any angle can be computed as the IFT of the 1D radial line in $F(k_x,k_y)$ passing *through the origin* and at the *same angle* θ.

In retrospect, then, the FT of each image domain projection at angle θ represents one radial line in k-space at the same angle θ. Thus, PR-MRI and CT data are both polar sampling acquisitions. The difference is that in MRI one samples the FT of the projections in k-space, while in CT one samples the image domain projections directly. The ensuing ramifications of this subtlety are examined in the Reconstruction Effects chapter.

1.3.3 Projection Reconstruction

As mentioned previously, the beginnings of MR imaging are attributed to Lauterbur [5] who acquired the Fourier transform of projections through the object, namely radial k_r-lines in k-space. Throughout the history of MRI, PR-MRI has proven to be useful and beneficial in many clinical situations.

Projection reconstruction MRI is advantageous in acquiring images of short T_1 and T_2 species. Ra [22, 23] used a hybrid PR-MRI and 2DFT imaging method to measure the short T_2 components of sodium ^{23}Na within the ranges 0.7–3.0ms and 16–30ms at 1.5 Tesla. The hybrid sequence involved a PR-MRI acquisition for the xy-directions, and a 2DFT approach in the slice (or z) direction.

Lung parenchyma imaging, like sodium imaging, is limited by low proton density and short T_2 components. Furthermore, susceptibility and motion artifacts also corrupt the image. But, signal intensity from the lung parenchyma, visibility of pulmonary structures, and signal-to-noise ratio (SNR) are improved using PR-MRI [24, 25]. Also, the imaging of boron ^{11}B (which has a T_2 on the order of 640μs) was achieved by Glover [26] for potential application to boron neutron capture therapy, a technique suggested for treating certain brain cancers.

Another advantage of PR-MRI is the suppression of flow and motion artifacts as compared to conventional 2DFT imaging methods. This is mostly due to the inherent signal averaging of low spatial frequencies from oversampling of central k-space data. Nishimura [27] found that PR-MRI is an effective method of eliminating the displacement artifact arising from flowing spins. Glover [28] also showed that PR-MRI techniques have intrinsic advantages over 2DFT methods with respect to diminished artifacts from respiratory motion.

Gmitro [29] used a PR-MRI diffusion-weighted technique to reduce the sensitivity to global translational motion of the object, while Glover [30] developed a consistent PR technique to reduce streak artifacts by applying consistency criteria to the acquired k-data.

Furthermore, the motion artifacts in functional MRI (fMRI) were compared for 2DFT, PR-MRI, and spiral scans [31]. The motions arise from the pulsations of the brain which cause pulsatile phase shifts in the acquired **k**-data. It was shown that PR-MRI and spiral methods exhibited reduced artifacts compared to conventional 2DFT imaging.

In addition, the projection reconstruction **k**-space trajectory lends itself to RARE-mode acquisition (also known as Fast Spin Echo and/or Turbo Spin Echo). RARE is the acronym of *R*apid *A*cquisition with *R*elaxed *E*nhancement in which the acquisition time is shorter than in conventional spin echo acquisitions. This is achieved by assigning multiple echoes in the spin echo train to different regions of **k**-space. The ramifications of RARE-mode polar acquisitions are examined in the T_2 Modulation Effects chapter. Early on, Hall [32] devised a T_2-weighted RARE PR-MRI sequence. In 1994, Rasche [33] analyzed and applied RARE-mode PR-MRI to abdominal and cardiac imaging. This provided a familiar contrast behaviour at a reduced scan time.

Hafner [34] proposed a simple fast imaging scheme based on low angle pulse excitation PR-MRI called BLAST (back-projection low angle shot) imaging applicable for imaging of both solids and liquids. The PR-MRI technique has also been used as a chemical-shift imaging method [35] whereby the PREP (projection reconstruction echo planar) imaging sequence was used to obtain fluorine images.

Still, projection reconstruction MRI can be disadvantageous, especially in the presence of magnetic field inhomogeneities [36]. For 2DFT, these inhomogeneities lead to geometrical distortions which can be corrected for easily, whereas in PR-MRI the inhomogeneities produce complicated distortions and a loss of spatial resolution (*i.e.* blurring in the image). Nevertheless, PR-MRI offers great promise in the imaging of short T_2 species, and in motion artifact suppression.

Therefore, a fundamental in-depth understanding of the image effects such as aliasing, resolution, SNR, and T_2 modulation effects are deemed necessary to establish the full potential of PR-MRI acquisitions.

1.3.4 Concentric Circles and Spirals

Polar sampling can be achieved by orienting the readout direction along the radial direction and repeating this acquisition for different discrete angles (such as in PR-MRI), or by orienting the readout direction along the azimuthal direction and repeating the acquisition for different radii. This second method is termed concentric circles MRI, or CC-MRI, and is a close relative of spiral imaging.

Concentric circles and spiral **k**-space trajectories were first conceptualized by Ljunggren [37], and later implemented by Matsui [38] and Ahn [39], respectively. These trajectories are advantageous in that the point spread functions due to T_2 decay are circularly symmetric, and the sequences exhibit a decreased sensitivity to flow artifacts.

The problems of reconstructing a 2D function from a set of spiral samples were addressed by Yudilevich and Stark [40], but a more general reconstruction method known as gridding [41, 42, 43] was further exploited by Jackson and Meyer [44, 45]. Gridding is a flexible algorithm that can be used to reconstruct any non-Cartesian **k**-space data set including spiral, PR-MRI, and CC-MRI acquisitions.

Many studies have been performed using spiral **k**-space trajectories including Meyer [44] who investigated coronary arterial disease, Gatehouse [46] and Pike [47] who examined spiral phase contrast methods for blood flow and velocity imaging, respectively, and Noll [48] who mapped cortical activation and showed that artifacts were reduced as compared to conventional imaging. Also, Block [49] shortened the acquisition time by developing a T_2-weighted RARE spiral sequence.

As a simplification to understanding the effects of spiral sampling, concentric circles can be used. One advantage is that the samples lie on circles at discrete radial locations. This allows an easier analysis of sampling effects such as SNR, resolution, and aliasing, and allows for different reconstruction algorithms (*e.g.* gridding and convolution backprojection) to be used. CC-MRI also lends itself to RARE-mode acquisitions whereby the T_2 modulation is circularly symmetric and isotropic.

Matsui [38] developed a concentric circles approach to **k**-space sampling using only half the number of pulses required by conventional 2DFT MR imaging. Moreover, since the readout is in the azimuthal direction (as opposed to the radial direction), fewer excitations are needed than in PR-MRI since the number of azimuthal samples is typically $\pi/2$ times greater than the number of radial samples. Azhari [50] contrasted CC-MRI with "half-Fourier" 2DFT methods and showed that for equal acquisition times, CC-MRI provides about a 17% increase in SNR.

One must be cautious in applying the understanding of CC-MRI effects to those of spiral MRI. This is especially true in terms of image aliasing since the respective point spread functions due to sampling are not identical, although they are similar. However, the T_2 modulation effects are nearly identical for CC-MRI and spiral MRI.

The importance of this treatise lies in the general formalism that is established to analyze the sampling, reconstruction, and T_2 modulation effects for polar **k**-space data. MRI data acquisition involves a number of tradeoffs which may affect the reconstructed image. In order to optimize the image quality and minimize any image artifacts, it is imperative that one understand (1) the fundamental effects of the data acquisition process, and (2) the MR physics associated with it.

This treatise attempts to lay some theoretical foundations to best understand the tradeoffs involved. Since many possible acquisition schemes are possible, here we limit ourselves to polar sampling with the intention that the conceptual formalism established herein be applied to other MRI acquisition schemes.

1.4 Research Goal

Magnetic resonance imaging is a powerful imaging modality that allows various soft-tissue contrast based primarily on proton density, T_1 or T_2 (the characteristic MR relaxation times), diffusion, or a combination of these characteristics. The so-called T_2-weighted images are very useful clinically; but, the major disadvantage is that these high-quality, diagnostically-interpretable images often require long imaging times.

The development and optimization of fast and ultrafast techniques [51, 52, 53, 54] allow shorter acquisition times. However, these methods generally suffer from reduced image contrast and/or low SNR. The acquisition sequence proposed by Hennig [55], often termed RARE, retains the soft-tissue contrast and SNR of T_2-weighted images, but with a reduced acquisition time in comparison to conventional T_2-weighted images.

Currently, non-Cartesian **k**-space sampling schemes such as spiral acquisitions [39, 40, 44], projection reconstruction [5, 32, 26], and concentric circles [38] are becoming more common. In particular, projection reconstruction and concentric circles schemes lend themselves easily to RARE-mode acquisitions.

The hypothesis is that polar sampling schemes, and more specifically RARE-mode polar sampling, are a viable alternative to acquiring high contrast, high SNR, T_2-weighted MR images. In this treatise, the research goal is to analyze the fundamental aspects of polar **k**-space sampling, namely sampling and image reconstruction effects such as aliasing, image resolution and signal-to-noise, and investigate the T_2 modulation effects when imaging in RARE-mode. The theoretical analysis is substantiated with experimental verification.

Our aim is to establish a firm theoretical framework to properly characterize the spatial effects of MR data acquisition and to lay the conceptual foundations of how one should characterize T_2 modulation (a temporal effect). The fundamental understanding gained herein leads us to a potentially powerful, yet general and simple T_2 demodulation method.

1.5 Thesis Overview

In this treatise, the research goal is to analyze the fundamental aspects of polar k-space sampling dealing with image resolution, SNR, aliasing effects, and T_2 modulation effects.

In the Sampling Effects chapter, the 2D Fourier aliasing effects of uniform polar sampling (*i.e.* equally-spaced radial and azimuthal samples) are explained. The primary focus is on the radial effects, and so the principal polar point spread function (PSF) is evaluated by assuming equally-spaced *ring* samples in k-space. Analytical derivations of the polar PSF are given, an intuitive approach is presented, and the aliasing effects are discussed, demonstrated, and numerically substantiated. This chapter is a published manuscript:

> **Lauzon ML**, and Rutt BK, "Effects of Polar Sampling in K-Space", *Magn Reson Med* **36**, 940–949 (1996).

In the Reconstruction Effects chapter, the resolution, SNR and aliasing characteristics of the gridding and convolution backprojection reconstruction algorithms are compared and contrasted for polar k-space sampling. This includes an in-depth analysis of modulation transfer functions and noise propagation, and a description of the aliasing effects of polar k-data reconstructed with the respective reconstruction algorithms. Practical SNR improvements with either reconstruction method are discussed, and the theoretical expectations are verified both numerically and experimentally. Moreover, the potential benefits of a hybrid gridding and convolution backprojection reconstruction algorithm applicable to radially non-equidistant but azimuthally equidistant polar k-data are analyzed and discussed. This chapter is a submitted manuscript currently (February 1998) under review:

> **Lauzon ML**, and Rutt BK, "Polar Sampling in K-Space: Reconstruction Effects", submitted to *Magn Reson Med* on January 8^{th}, 1997, and revised November 5^{th}, 1997.

In the T_2 Modulation Effects chapter, the amplitude modulation effects of RARE-mode polar sampling for projection reconstruction and concentric circles are analyzed. The T_2-weighting and T_2 impulse response function analytical formalism is presented. Also, the effective echo times are derived, which allows one to characterize the effective T_2-weighted contrast curves. The theoretical expectations are substantiated by numerical simulations, and verified experimentally. The ramifications of T_2-weighting pertaining to polar acquisitions are discussed.

In the Conclusions and Discussion chapter, a summary of the more pertinent and salient points of this treatise are presented. The results regarding overall image quality are discussed. Also, a possible future direction in the area of T_2-demodulated MR imaging is presented.

1.6 References

[1] F. Bloch. W.W. Hansen. M. Packard. Nuclear induction. *Phys. Rev.* **69**. 127 (1946).

[2] E.M. Purcell. H.C. Torrey. R.V. Pound. Resonance absorption by nuclear magnetic moments in a solid. *Phys. Rev.* **69**. 37–38 (1946).

[3] C.P. Slichter. "Principles of Magnetic Resonance. 3^{rd} Edition". Springer Verlag. New York. 1990.

[4] A. Abragam. "The Principles of Nuclear Magnetism". Clarendon Press. Oxford. 1994.

[5] P.C. Lauterbur. Image formation by induced local interactions: examples employing nuclear magnetic resonance. *Nature* **242**. 190–191 (1973).

[6] P.G. Morris. "Nuclear Magnetic Resonance Imaging in Medicine and Biology". Clarendon Press. Oxford. 1986.

[7] W.S. Brey (Ed.). "Magnetic Resonance in Perspective: Highlights of a Quarter Century". Academic Press. San Diego. 1996.

[8] F. Bloch. Nuclear induction. *Phys. Rev.* **70(7-8)**. 460–474 (1946).

[9] H.C. Torrey. Bloch equations with diffusion terms. *Phys. Rev.* **104(3)**. 563–565 (1956).

[10] E.O. Stejskal. Use of spin echoes in a pulsed magnetic-field gradient to study anisotropic. restricted diffusion and flow. *J. Chem. Phys.* **43(10)**. 3597–3603 (1965).

[11] A. Papoulis. "The Fourier Integral and its Applications". McGraw-Hill. New York. 1962.

[12] R.N. Bracewell. "The Fourier Transform and its Applications". McGraw Hill. New York. 1986.

[13] E.O. Brigham. "The Fast Fourier Transform". Prentice-Hall. Englewood Cliffs. N.J.. 1974.

[14] H. Nyquist. Certain topics in telegraph transmission theory. *Trans. AIEE* **47**. 617–644 (1928)(February).

[15] R. Gabillard. Mesure du temps de relaxation T_2 en présence d'une inhomogénéité de champ magnétique supérieure à la largeur de raie. *C. R. Acad. Sci.* **232**. 1551–1553 (1951).

[16] R. Bradford. C. Clay. E. Strick. A steady-state transient technique in nuclear induction. *Phys. Rev.* **84(1)**. 157–158 (1951).

[17] H.Y. Carr. E.M. Purcell. Effects of diffusion on free precession in nuclear magnetic resonance experiments. *Phys. Rev.* **94(3)**. 630–638 (1954).

[18] P. Mansfield. P.K. Grannell. NMR diffusion in solids? *J. Phys* **C6**. L422 (1973).

[19] G.T. Herman. "Image Reconstruction from Projections: The Fundamentals of Computerized Tomography". Academic Press. New York. 1980.

[20] R.N. Bracewell. Strip integration in radio astronomy. *Aust. J. Phys.* **9**. 198–217 (1956).

[21] S. Dunne. S. Napel. B. Rutt. Interactive display of volumetric data by fast Fourier projection. *Comput. Med. Imag. Graph.* **16(4)**. 237–251 (1992).

[22] J.B. Ra. S.K. Hilal. Z.H. Cho. A method for *in vivo* MR imaging of the short T_2 component of sodium-23. *Magn. Reson. Med.* **3**. 296–302 (1986).

[23] J.B. Ra. S.K. Hilal. C.H. Oh. An algorithm for MR imaging of the short T_2 fraction of sodium using the FID signal. *J. Comput. Assist. Tomogr.* **13(2)**. 302–309 (1989).

[24] C.J. Bergin. J.M. Pauly. A. Macovski. Lung parenchyma: projection reconstruction MR imaging. *Radiology* **179(3)**. 777–781 (1991).

[25] S.L. Gewalt. G.H. Glover. L.W. Hedlund. G.P. Cofer. J.R. MacFall. G.A. Johnson. MR microscopy of the rat lung using projection reconstruction. *Magn. Reson. Med.* **29**. 99–106 (1993).

[26] G.H. Glover. J.M. Pauly. K.M. Bradshaw. Boron-11 imaging with a three-dimensional reconstruction method. *J. Magn. Reson. Imag.* **2(1)**. 47–52 (1992).

[27] D.G. Nishimura. J.I. Jackson. J.M. Pauly. On the nature and reduction of the displacement artifact in flow images. *Magn. Reson. Med.* **22**. 481–492 (1991).

[28] G.H. Glover. J.M. Pauly. Projection reconstruction techniques for reduction of motion effects in MRI. *Magn. Reson. Med.* **28**. 275–289 (1992).

[29] A.F. Gmitro. A.L. Alexander. Use of a projection reconstruction method to decrease motion sensitivity in diffusion-weighted MRI. *Magn. Reson. Med.* **29**. 835–838 (1993).

[30] G.H. Glover. D.C. Noll. Consistent projection reconstruction (CPR) techniques for MRI. *Magn. Reson. Med.* **29**. 345–351 (1993).

[31] G.H. Glover. A.T. Lee. Motion artifacts in fMRI: comparison of 2DFT with PR and spiral scan methods. *Magn. Reson. Med.* **33**. 624–635 (1995).

[32] L.D. Hall. S. Sukumar. Rapid data-acquisition technique for NMR imaging by the projection-reconstruction method. *J. Magn. Reson.* **56**. 179–182 (1984).

[33] V. Rasche. D. Holz. W. Schepper. Radial turbo spin echo imaging. *Magn. Reson. Med.* **32**. 629–638 (1994).

[34] S. Hafner. Fast imaging in liquids and solids with the back-projection low angle shot (BLAST) technique. *Magn. Reson. Imag.* **12(7)**. 1047–1051 (1994).

[35] M. Doyle. P. Mansfield. Chemical-shift imaging: a hybrid approach. *Magn. Reson. Med.* **5**. 255–261 (1987).

[36] M. O'Donnell. W.A. Edelstein. NMR imaging in the presence of magnetic field inhomogeneities and gradient field nonlinearities. *Med. Phys.* **12(1)**. 20–26 (1985).

[37] S. Ljunggren. A simple graphical representation of Fourier-based imaging methods. *J. Magn. Reson.* **54**. 338–343 (1983).

[38] S. Matsui. H. Kohno. NMR imaging with a rotary field gradient. *J. Magn. Reson.* **70**. 157–162 (1986).

[39] C.B. Ahn. J.H. Kim. Z.H. Cho. High-speed spiral-scan echo planar NMR imaging. *IEEE Trans. on Med. Imag.* **5(1)**. 2–7 (1986).

[40] E. Yudilevich. H. Stark. Spiral sampling: theory and an application to magnetic resonance imaging. *J. Opt. Soc. Amer. A* **5(4)**. 542–553 (1988).

[41] W.N. Brouw. Aperture synthesis. *in* "Methods in Computational Physics. volume 14" (B. Alder. S. Fernbach. and M. Rotenberg. Eds.). pp. 131–175. Academic Press. New York. 1975.

[42] F.R. Schwab. Optimal gridding visibility data in radio interferometry. *in* "Indirect Imaging". (J.A. Roberts. Ed.). pp. 333–346. Cambridge University Press. New York. 1983.

[43] J.D. O'Sullivan. A fast sinc function gridding algorithm for Fourier inversion in computer tomography. *IEEE Trans. on Med. Imag.* **4(4)**. 200–207 (1985).

[44] C.H. Meyer. B.S. Hu. D.G. Nishimura. A. Macovski. Fast spiral coronary artery imaging. *Magn. Reson. Med.* **28**, 202–213 (1992).

[45] J.I. Jackson, C.H. Meyer, D.G. Nishimura, A. Macovski, Selection of a convolution function for Fourier inversion using gridding. *IEEE Trans. on Med. Imag.* **10(3)**, 473–478 (1991).

[46] P.D. Gatehouse, D.N. Firmin, S. Collins, D.B. Longmore, Real time blood flow imaging by spiral scan phase velocity mapping. *Magn. Reson. Med.* **31**, 504–512 (1994).

[47] G.B. Pike, C.H. Meyer, T.J. Brosnan, N.J. Pelc, Magnetic resonance velocity imaging using a fast spiral phase contrast sequence. *Magn. Reson. Med.* **32**, 476–483 (1994).

[48] D.C. Noll, J.D. Cohen, C.H. Meyer, W. Schneider, Spiral k-space MR imaging of cortical activation. *J. Magn. Reson. Imag.* **5(1)**, 49–56 (1995).

[49] W. Block, J. Pauly, D. Nishimura, RARE spiral T_2-weighted imaging. *Magn. Reson. Med.* **37**, 582–590 (1997).

[50] H. Azhari, O.E. Denisova, A. Montag, E.P. Shapiro, Circular sampling: perspective of a time-saving scanning procedure. *Magn. Reson. Imag.* **14(6)**, 625–631 (1996).

[51] P. Mansfield, Multi-planar image formation using NMR spin echoes. *J. Phys. C: Sol. State Phys.* **10**, L55–L58 (1977).

[52] J. Frahm, A. Haase, D. Matthaei, Rapid NMR imaging of dynamic processes using the FLASH technique. *Magn. Reson. Med.* **3**, 321–327 (1986).

[53] A. Macovski, C. Meyer, A novel fast-scanning system. In *Proc of SMRM Fifth Ann Meet (WIP)*, pp. 156–157, Montreal, Canada, 1986.

[54] I.L. Pykett, R.R. Rzedzian, Instant images of the body by magnetic resonance. *Magn. Reson. Med.* **5**, 563–571 (1987).

[55] J. Hennig. A. Nauerth. H. Friedburg. RARE imaging: a fast imaging method for clinical MR. *Magn. Reson. Med.* **3**. 823–833 (1986).

Chapter 2

Sampling Effects

2.1 Introduction

Magnetic resonance imaging (MRI) is a versatile imaging modality which allows various sampling schemes, be they on a Cartesian, polar, spherical, or other non-rectilinear coordinate system. The data are acquired in Fourier space, often termed k-space; the image is the inverse Fourier transform (IFT) of these collected data, which are sampled (*i.e.* discrete) as opposed to continuous. The discretization and the finite extent of acquisition leads to potential aliasing effects and/or artifacts which may adversely affect the image content.

In the majority of MR acquisitions, the data are acquired on a Cartesian coordinate system. Use of the efficient fast Fourier transform (FFT) [1] transforms the Cartesian k-space frequencies to Cartesian image space intensities. The aliasing effects in such cases are well understood [2, 3]. Cartesian acquisitions allow for efficient image reconstruction and exhibit aliasing properties that are easily described by well-known Fourier theorems.

Currently, non-rectilinear sampling schemes are gaining popularity, most notably spiral acquisitions [4, 5, 6], projection reconstruction [7, 8, 9], and concentric circles [10]. These non-rectilinear sampling schemes offer advantages in motion and flow artifact suppression, efficient use of gradients, and fast acquisitions. The disadvantages lie primarily in more complicated image reconstruction and off-resonance effects. In

projection reconstruction MRI, the convolution backprojection algorithm [11, 12] may be used; in general, however, reconstruction involves regridding [13, 14, 15, 16] the k-data onto a Cartesian grid and using the FFT. The gridding process may affect the image [16]; but more fundamentally, non-rectilinear sampling itself will influence the image characteristics.

Here, we explain the two-dimensional (2D) Fourier aliasing effects of uniform polar sampling, whereby the samples are equally-spaced both radially and azimuthally. We focus primarily on radial effects and so assume equally-spaced ring samples in k-space. Previous work has been done by Stark with regards to computed tomography (CT) [17, 18, 19]; here we adopt a different approach pertinent to MR sampled data. In this chapter, no attempt is made at explaining MR physics effects such as off-resonance effects, motion, T_1 and/or T_2 modulations; we deal strictly with the sampling aspects of polar acquisitions. Analytical derivations are given, and their significance is discussed.

2.2 Theory

In Cartesian coordinates, the concept of finding the point spread function (PSF), *i.e.* the Fourier transform of the sampling function, in two (or more) dimensions follows readily from the one-dimensional (1D) case: one performs the 1D-FT independently for each dimension. In polar coordinates, however, the task is more difficult.

A sampling function can be mathematically represented as a superposition of Dirac delta-functions (δ-functions). An important aspect of polar sampling, and non-rectilinear sampling in general, is the weighting associated with each δ-function. This weighting occurs because δ-functions are defined within an integral, and the infinitesimal area of integration must be taken into account in order to properly normalize each δ-sample. In section 2.2.1, we show that this weighting is the Jacobian in transforming to a coordinate system where the δ-spacing is rectilinear.

For polar sampling, the discretization occurs in both the radial and azimuthal directions. However, in the limit of equally-spaced azimuthal samples being infinitesimally close together, we can focus exclusively on the radial effects of polar sampling since we effectively have a superposition of circularly symmetric ring samples. Although the sampling of continuous rings is unrealizable in practice, its FT leads to the *principal* PSF of polar sampling which can be calculated using the Fourier-Bessel (Hankel) transform, a 1D transform. In section 2.2.2, we develop the governing mathematical Fourier formulation. Based on work by Bracewell and Thompson [20], we separate the principal polar PSF into its main lobe and a series of ringlobes.

With the analysis developed in the theory section, we are able to characterize the radial effects of polar aliasing. This includes concepts such as radial sampling requirements, smearing, leakage, and truncation artifacts.

2.2.1 Weighting of δ-Functions

Dirac delta-functions, represented as $\delta(\star)$, were introduced by Dirac in quantum mechanics [21]. Fundamentally, δ-functions (impulses) are defined by their action *within* an integral, namely

$$\int_a^b f(x)\,\delta(x-x')\,dx \;=\; \begin{cases} f(x') & \text{if } a < x' < b \\ 0 & \text{otherwise} \end{cases} \tag{2.1}$$

This is called the *sifting* property of δ-functions. Moreover, a δ-function has zero width and infinite height such that the δ-area is unity, *i.e.* $\int_{-\infty}^{+\infty} \delta(x)\,dx = 1$. If one changes the scale of x by a factor ε, say $x \rightarrow x/\varepsilon$, then $\delta(x/\varepsilon) = |\varepsilon|\delta(x)$ [3, p.76]. In other words, a change in scale weights the intensity of the impulse commensurately. In general, we may have a superposition of δ-functions at various locations. For the 1D unit-spaced case, we have the *shah* function, $\text{Ш}(x) \equiv \sum_j \delta(x-j)$. If we scale $\text{Ш}(x)$ in the x-direction from equidistant unit-spacing to ε-spacing, then

$$\begin{aligned} \int \left\{ \sum_j \delta\left(\frac{x}{\varepsilon} - j\right) \right\} dx \;&=\; \int \left\{ \sum_j \delta(x - \varepsilon j)\,|\varepsilon| \right\} dx \qquad \text{by scaling property} \\ &=\; \int \left\{ \sum_j \delta(u-j)\,|\varepsilon| \right\} du \qquad \text{for } u = x/\varepsilon \end{aligned} \tag{2.2}$$

The above equation can be interpreted as follows: the δ-functions have equidistant ε-spacing in the x-coordinate system but are *unit*-spaced in the u-coordinate system. However, in both the x- and u-systems, the δ-functions have a weighting of ε: in the x-system, it arises because of the scaling property of δ-functions, whereas in the u-system, it is the Jacobian $|dx/du|$. For a general superposition of δ-functions of the form $\sum_j \delta[\varepsilon(x) - j]$, we have

$$\begin{aligned} \int \left\{ \sum_j \delta[\varepsilon(x) - j] \right\} dx \;&=\; \int \left\{ \frac{\sum_j \delta(x - x_j)}{|d\varepsilon(x)/dx|} \right\} dx \qquad \text{by scaling property} \\ &=\; \int \left\{ \sum_j \delta(u-j) \left| \frac{dx}{du} \right| \right\} du \qquad \text{for } u = \varepsilon(x) \end{aligned} \tag{2.3}$$

Note that the δ-functions are equidistant and *unit*-spaced in the u-system, but could be non-rectilinear in the x-system. As before, the weighting of the j^{th} δ-function is the Jacobian $|dx/du|_{u=j} \leftrightarrow |d\varepsilon(x)/dx|^{-1}_{x=x_j}$.

Note that when one writes $\sum_j \delta[\xi(x) - j]$, this is in fact a short-hand notation for $\int \sum_j \delta[\xi(x) - j]\,dx$ whereby the δ-functions' intensity and position information are hidden within the $\xi(x)$ term. However, if one makes a coordinate transformation from x to u such that the spacing is linear and unit-spaced in the u-system, we have $\int \sum_j \delta[u - j]\,\mathcal{J}_j\,du$, where $\mathcal{J}_j$ is effectively the Jacobian evaluated at $u=j$. When written in this manner, the intensity ($\mathcal{J}_j$) and position ($u=j$) of each δ-function are obvious, and the short-hand notation is given by $\sum_j \delta[u - j]\,\mathcal{J}_j$. Expressed in the x-system, and because $|d\xi(x)/dx|^{-1}_{x=x_j} = |dx/du|_{u=j} \equiv \mathcal{J}_j$, any one-dimensional sampling function can be written as

$$\sum_j \delta(x - x_j)\,\mathcal{J}_j \tag{2.4}$$

where x_j and $\mathcal{J}_j$ are the location and weighting of the j^{th} δ-function, respectively. Generalizing Eq.(2.4) to n-dimensions, we have

$$\sum_j \delta(\mathbf{x} - \mathbf{x}_j)\,\mathcal{J}_j \qquad \text{with} \qquad \mathcal{J}_j = \left| \begin{array}{ccc} \partial x_1/\partial u_1 & \cdots & \partial x_1/\partial u_n \\ \vdots & \ddots & \vdots \\ \partial x_n/\partial u_1 & \cdots & \partial x_n/\partial u_n \end{array} \right|_{\mathbf{x}=\mathbf{x}_j} \tag{2.5}$$

where $\mathbf{x}_j$ and $\mathcal{J}_j$ are the location and weighting of the j^{th} n-dimensional δ-function, respectively. As in the 1D case, the Jacobian is found by transforming from $\mathbf{x}$-coordinates to $\mathbf{u}$-coordinates such that the δ-functions are unit-spaced and rectilinear in each of the n-dimensions in the $\mathbf{u}$-system.

A few 2D examples may give a better intuition. First, let us look at 2D Cartesian sampling with spacing Δx and Δy in the x- and y-directions, respectively. The transformation requires $u_1 = x/\Delta x$ and $u_2 = y/\Delta y$ so that the Jacobian (and hence the weighting) is $\Delta x \Delta y$:

$$\sum_j \sum_k \delta(x - j\Delta x)\,\delta(y - k\Delta y)\,\Delta x \Delta y \tag{2.6}$$

As a second example, we look at polar sampling where the radial (r) and azimuthal (θ) spacings are Δr and $\Delta\theta$, respectively. The polar coordinates $x_1 = r\cos\theta$, and $x_2 = r\sin\theta$ can be transformed to rectilinear u-coordinates provided that $u_1 = r/\Delta r$,

and $u_2=\theta/\Delta\theta$: the Jacobian is $|r|\Delta r\Delta\theta$ and the polar sampling function is

$$\sum_j \sum_k \delta[x - j\Delta r\cos(k\Delta\theta)]\ \delta[y - j\Delta r\sin(k\Delta\theta)]\ j\,(\Delta r)^2\Delta\theta \qquad (2.7)$$

Note that for polar sampling, the weighting is proportional to the *radial distance* of the sample. One can draw an analogy with parallel-beam computed tomography.

Although CT data are acquired in the image domain, the 1D-FT of each image domain projection at angle θ represents the k-space line at angle θ. To reconstruct the image, each k-line is multiplied by the ramp filter (a function proportional to the radial distance), inverse Fourier transformed, and backprojected. The ramp filter, then, is simply the weighting necessary for polar sampling. Moreover, note that multiplication of the k-lines with the ramp filter is the Fourier conjugate to convolution of the image domain projections with the IFT of the ramp-filter. Thus, the convolution kernel of the CT convolution backprojection algorithm simply applies the necessary polar sampling weighting in the *image* domain.

Mathematically, we can express discretization as the multiplication of a continuous object with a sampling function. Each discrete sample subtends a given area, as given by the Jacobian. In Cartesian sampling, each sample has the same constant area, namely $\Delta x\Delta y$, so that the δ-area for each sample is constant. In equidistant polar sampling, however, the sample size changes as a function of radius. Thus, to normalize the δ-area for each sample, we weight each sample by its areal extent; this is equivalent to correcting for the sampling density.

Finally, note that if we had a non-rectilinear Fourier transform algorithm expressed in u-coordinates, the algorithm would already include the Jacobian: the δ-weighting would effectively be "built-in" to the algorithm. An example is the Hankel transform for circularly symmetric objects whose coordinate system changes from x- and y-coordinates to r-coordinates, as will be shown in section 2.2.2.

In MRI, one can acquire the data in various 2D and/or 3D coordinate systems. To reconstruct the object properly, however, one must weight the samples appropriately depending on the reconstruction algorithm used.

2.2.2 Ring Samples and the Principal Polar PSF

In polar sampling, the coordinates of interest are the radial and azimuthal directions. Typically, one acquires enough azimuthal samples so that the maximum arc-distance between samples is less or equal to the radial spacing. Under these circumstances, the sampling effects are primarily associated with the radial direction only.

To understand the radial effects of polar sampling, we will assume equally-spaced, concentric, continuous ring samples. In effect, we consider the limiting case where the azimuthal sample spacing tends to zero. Since the sampling function exhibits circular properties, it is advantageous to convert the Fourier transform integral from Cartesian to polar coordinates. In MRI, we acquire the data in **k**-space from which the image is computed as the 2D inverse Fourier transform of $S(k_x, k_y)$:

$$s(x, y) = \int_{-\infty}^{+\infty} \int_{-\infty}^{+\infty} S(k_x, k_y)\, \epsilon^{2\pi i[xk_x + yk_y]}\, dk_x dk_y \tag{2.8}$$

where k_x and k_y are the Fourier conjugates of x and y, respectively. If we express the Fourier and image domains in polar notation, namely $k_x = k_r \cos k_\theta$, $k_y = k_r \sin k_\theta$, and $x = r\cos\theta$, $y = r\sin\theta$, with k_r and k_θ the Fourier conjugates of r and θ, respectively, we have [3, p.247]

$$s(r, \theta) = \int_{k_\theta=0}^{2\pi} \int_{k_r=0}^{\infty} S(k_r, k_\theta)\, \epsilon^{2\pi i r k_r \cos(k_\theta - \theta)}\, k_r dk_r dk_\theta \tag{2.9}$$

Furthermore, if $S(k_r, k_\theta)$ is circularly symmetric (which is the case here with concentric rings), *i.e.* $S(k_r, k_\theta) \rightarrow S(k_r)$, then we can integrate over the k_θ variable to obtain the well-known Hankel transform:

$$s(r) = 2\pi \int_0^{\infty} S(k_r) J_0(2\pi r k_r)\, k_r dk_r = \int_0^{\infty} \{2\pi k_r S(k_r)\}\, J_0(2\pi r k_r)\, dk_r \tag{2.10}$$

Note that $S(k_r)$ is *weighted by* the Jacobian $2\pi k_r$ so that the Hankel transform of $S(k_r)$ is the same as the Cartesian Fourier transform of $S(k_x, k_y)$. Thus, the necessary weighting for polar sampling is built-in to this transform.

Assume we sample at the origin of **k**-space ($k_r = 0$) and at M equally-spaced concentric rings, as shown in Figure 2.1. For a radial spacing of Δk_r, the ring positions

are given by

$$\sum_{m=1}^{M} \delta\left(\frac{k_r}{\Delta k_r} - m\right) = \sum_{m=1}^{M} \delta(k_r - m\Delta k_r)\ \Delta k_r \tag{2.11}$$

whose Hankel transform is

$$2\pi(\Delta k_r)^2 \sum_{m=1}^{M} m J_0(2\pi r m \Delta k_r) \tag{2.12}$$

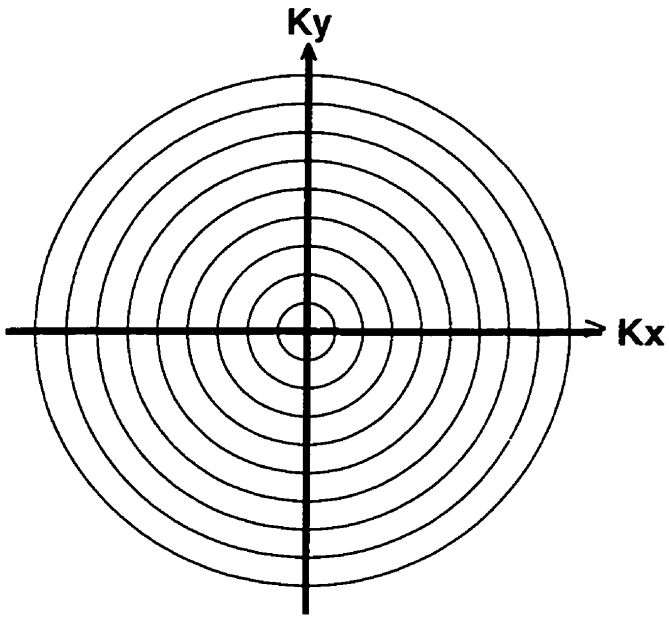

Figure 2.1: K-space sampling rings
Equidistant, concentric sampling rings in k*-space.*

As for the δ-sample at the origin, one might assume the weighting to be identically zero (since $k_r = 0$). However, the weighting function, as discussed in section 2.2.1, describes the *areal extent* of a given sample. If we had sampled continuously in the radial direction, then the weighting would be zero at $k_r = 0$ since the areal extent of a point is zero. But, for finite sampling, the sample has finite area, and so its weighting is $\pi(\Delta k_r/2)^2$. The Fourier transform of the weighted δ-function at the origin is a constant, namely $\pi(\Delta k_r/2)^2$. Since the Fourier transform is a linear operator, the IFT of $S(k_r)$ is given by

$$s(r) = \frac{\pi(\Delta k_r)^2}{4} + 2\pi(\Delta k_r)^2 \sum_{m=1}^{M} m J_0(2\pi r m \Delta k_r) \tag{2.13}$$

Its profile is depicted in Figure 2.2 for $M = 9$, where $s(r)$ is called the *principal* polar PSF, a term coined by Bracewell [20]. Some salient features of $s(r)$ include: (1) discretization by Δk_r in the radial direction leads to radial *ringlobes* at $r = j/\Delta k_r, j = \{1, 2, \ldots\}$. (2) the radial ringlobes are *asymmetric* and decrease in amplitude as r increases. (3) there are approximately M oscillation periods between successive ringlobes, where M is the number of rings: this is a truncation artifact and arises because M is finite. (4) the width of the central (or main) lobe decreases as M increases. (5) the oscillation and ringlobe amplitudes relative to the main lobe decrease as M increases. (6) the main lobe behaves as $J_1(r)/r$, the *jinc* function: this becomes apparent if we let $M \to \infty$ and $\Delta k_r \to 0$ such that $M\Delta k_r \to c$ (a unit-height disk, whose FT is $(2\pi c^2)\,\mathrm{jinc}(2\pi rc)$ [3, p.249]). (7) although $S(k_r)$ is radially-discrete and of finite extent, $s(r)$ is continuous and of infinite extent.

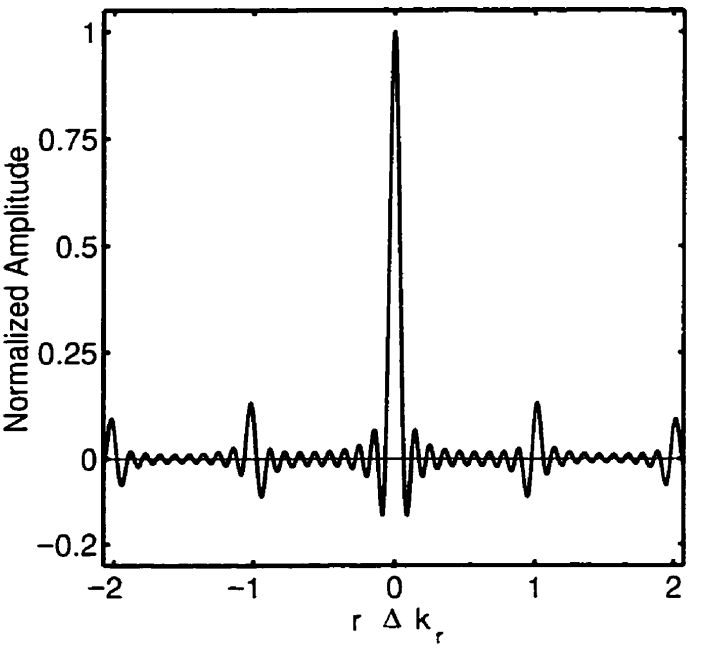

Figure 2.2: Principal polar PSF profile
Principal polar PSF profile for $M = 9$ concentric rings.

Based on work by Bracewell and Thompson [20], we can decompose $s(r)$ of Eq.(2.13) into its main lobe and a series of ringlobes. Using [22, p.952 (8.411)] to

express J_0 in integral form, and introducing the spin-integration operator $\mathcal{Q}$, we have

$$J_0(\rho) = \frac{1}{\pi}\int_0^{\pi} \cos(\rho\cos\beta)\, d\beta \equiv \mathcal{Q}\{\cos\rho\} \tag{2.14}$$

where we define the spin-integrator as

$$\mathcal{Q}\{f(\rho)\} \equiv \frac{1}{\pi}\int_0^{\pi} f(\rho\cos\beta)\, d\beta \tag{2.15}$$

Consequently, Eq.(2.13) can be written as

$$\begin{aligned} s(r) &= \frac{\pi(\Delta k_r)^2}{4} + 2\pi(\Delta k_r)^2 \sum_{m=1}^{M} m\mathcal{Q}\{\cos(2\pi r m\Delta k_r)\} \\ &= \frac{\pi(\Delta k_r)^2}{4} + \mathcal{Q}\left\{\sum_{m=1}^{M} 2\pi(\Delta k_r)^2 m\cos(2\pi r m\Delta k_r)\right\} \\ &= \frac{\pi(\Delta k_r)^2}{4} + \mathcal{Q}\{v(r)\} \end{aligned} \tag{2.16}$$

where $v(r) = \sum_{m=1}^{M} 2\pi(\Delta k_r)^2 m\cos(2\pi r m\Delta k_r)$. By going through the Fourier domain,

$$\begin{aligned} v(r) &= \mathcal{F}^{-1}\{\mathcal{F}\{v(r)\}\} \\ &= \mathcal{F}^{-1}\left\{\sum_{m=1}^{M} \pi(\Delta k_r)^2 m\left[\delta(k - m\Delta k_r) + \delta(k + m\Delta k_r)\right]\right\} \\ &= \mathcal{F}^{-1}\left\{\pi M\Delta k_r\left[\Pi\left(\frac{k}{2M\Delta k_r}\right) - \Lambda\left(\frac{k}{M\Delta k_r}\right)\right]\text{Ш}\left(\frac{k}{\Delta k_r}\right)\right\} \\ &= \pi(M\Delta k_r)^2\left[2\mathrm{sinc}(2Mr\Delta k_r) - \mathrm{sinc}^2(Mr\Delta k_r)\right] \star \left[\Delta k_r\text{Ш}(r\Delta k_r)\right] \\ &= v_0(r) + \sum_{j=1}^{\infty}\left[v_0\left(r - \frac{j}{\Delta k_r}\right) + v_0\left(r + \frac{j}{\Delta k_r}\right)\right] \end{aligned} \tag{2.17}$$

where $\mathcal{F}$ and $\mathcal{F}^{-1}$ denote the forward and inverse Fourier transforms, respectively. $\text{Ш}(k/\Delta k_r)$ represents a series of δ-functions spaced by Δk_r in k-space. $\text{Ш}(r\Delta k_r)$ represents a series of δ-functions spaced by $1/\Delta k_r$ in image space. $\star$ denotes convolution, and

$$v_0(r) = \pi(M\Delta k_r)^2\left[2\mathrm{sinc}(2Mr\Delta k_r) - \mathrm{sinc}^2(Mr\Delta k_r)\right] \tag{2.18}$$

$$\Pi(\rho) = \begin{cases} 1, & |\rho| \le 1/2 \\ 0, & |\rho| > 1/2 \end{cases}, \quad \Lambda(\rho) = \begin{cases} 1 - |\rho|, & |\rho| \le 1 \\ 0, & |\rho| > 1 \end{cases}, \quad \text{and}$$

$$\Pi\left(\frac{\rho}{2}\right) - \Lambda(\rho) = |\rho|\,\Pi\left(\frac{\rho}{2}\right) \tag{2.19}$$

Substituting Eq.(2.17) into Eq.(2.16), we have

$$\begin{aligned} s(r) &= \frac{\pi(\Delta k_r)^2}{4} + \mathcal{Q}\{c_0(r)\} + \sum_{j=1}^{\infty} \mathcal{Q}\left\{c_0\left(r - \frac{j}{\Delta k_r}\right) + c_0\left(r + \frac{j}{\Delta k_r}\right)\right\} \\ &= \frac{\pi(\Delta k_r)^2}{4} + s_0(r) + \sum_{j=1}^{\infty} s_j(r) \end{aligned} \tag{2.20}$$

where s_0 and s_j are the spin integrations of $c_0(r)$ and the summation terms, respectively, and the constant term $\pi(\Delta k_r)^2/4$ arose because of the δ-sample at the origin of k-space. We next study $s_0(r)$ and $s_j(r)$ individually to gain further insight.

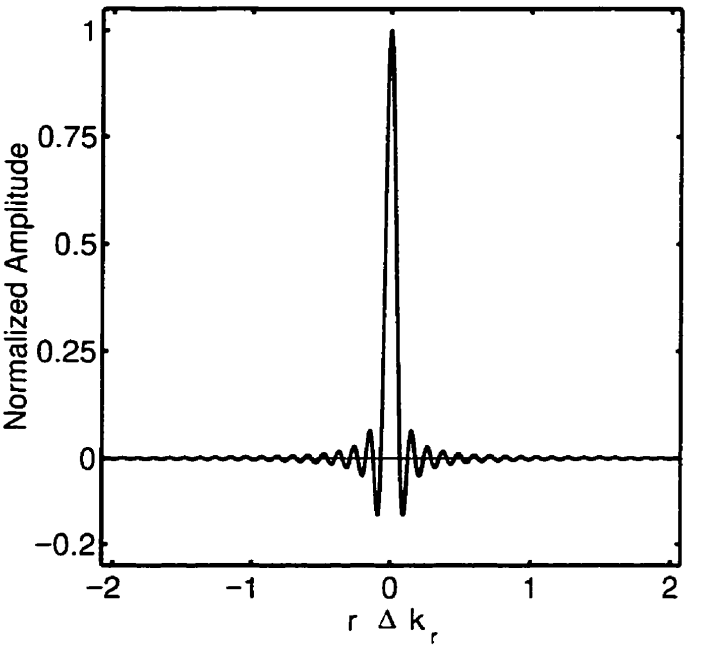

Figure 2.3: Normalized principal polar PSF main lobe $s_0(r)$
Normalized principal polar PSF main lobe $s_0(r)$ for $M = 9$ concentric rings.

To simplify $s_0(r)$, we make use of the spin-integral theorem [20, app.B] which states that $\mathcal{Q}\{c(r)\} = \mathcal{H}\{\mathcal{F}_c\{c(r)\}/(\pi k_r)\}$, where $\mathcal{F}_c$ and $\mathcal{H}$ denote the Fourier cosine and Hankel operators, respectively. Since the Fourier cosine transform of $c_0(r)$ is $\pi|k_r|\prod(k_r/[2M\Delta k_r])$, we have

$$\begin{aligned} s_0(r) &= \mathcal{H}\left\{\prod\left(\frac{k_r}{2M\Delta k_r}\right)\right\} = 2\pi \int_0^{M\Delta k_r} J_0(2\pi r k_r)\; k_r dk_r \\ &= 2\pi(M\Delta k_r)^2 \,\mathrm{jinc}(2\pi M r \Delta k_r) \end{aligned} \tag{2.21}$$

which is the Hankel transform of a unit height disk of radius $M\Delta k_r$. Note the jinc-like behaviour of the main lobe, as expected: $s_0(r)$ appears in Figure 2.3.

To investigate the ringlobes $s_j(r)$, one can apply the spin-integral theorem (as stated above) to $[\upsilon_0(r-j/\Delta k_r) + \upsilon_0(r+j/\Delta k_r)]$ to show that

$$\begin{aligned} s_j(r) &= \mathcal{H}\left\{2\cos\left(\frac{2\pi j k_r}{\Delta k_r}\right)\Pi\left(\frac{k_r}{2M\Delta k_r}\right)\right\} \\ &= 4\pi\int_0^{M\Delta k_r}\cos\left(\frac{2\pi j k_r}{\Delta k_r}\right)J_0(2\pi r k_r)\; k_r dk_r \end{aligned} \tag{2.22}$$

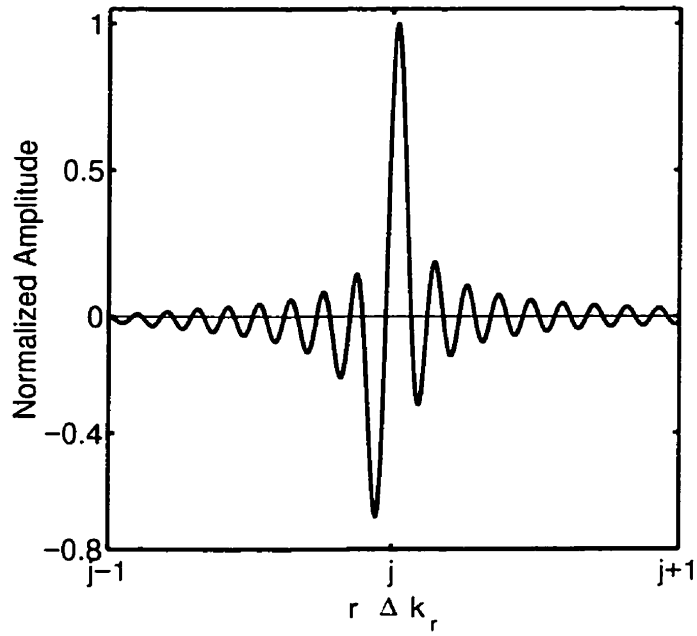

Figure 2.4: Normalized principal polar PSF ringlobe $s_j(r)$
Normalized principal polar PSF ringlobe $s_j(r)$ for $M = 9$ concentric rings.

An analytical expression of the above function is not readily available, although Bracewell and Thompson [20] have approximated this function near $j/\Delta k_r$. Nevertheless, one can numerically evaluate the above equation to get a visual representation of $s_j(r)$, as shown in Figure 2.4. Note that all ringlobes are similar in appearance, although their amplitudes will be different depending on the ringlobe order j. From Bracewell and Thompson's approximation, the maximum amplitude of s_j is about $2.25(M\Delta k_r)^2/\sqrt{\pi M j}$. Comparison of two ringlobes shows that their relative amplitudes scale as the square-root of the ratio of ringlobe orders, *i.e.* $|s_{j_1}|/|s_{j_2}| \simeq \sqrt{j_2/j_1}$.

Furthermore, the ringlobe amplitude relative to that of the main lobe, whose amplitude is $\pi(M\Delta k_r)^2$, is given by

$$|s_j| \simeq \frac{2.25}{\pi\sqrt{\pi M j}} |s_0| \tag{2.23}$$

For M-values of 64–128 rings (as would be typical in MRI), the peak amplitude of $s_1(r)$ is about 5.1%–3.6% of the main lobe peak amplitude.

In summary, the principal polar PSF can be decomposed into its main lobe whose behaviour is jinc-like, and a series of asymmetric ringlobes at $j/\Delta k_r$ whose peak amplitudes decay as j increases. Knowledge of the principal polar PSF, its constituents, and its characteristics allows us to investigate the aliasing effects incurred by polar sampling, as discussed in the next section.

2.3 Results

In the theory section, we mathematically characterized the behaviour and composition of the principal polar point spread function. In contrast, this section attempts to give an intuitive understanding of the behaviour of the principal polar PSF. We also discuss the ensuing effects in the image domain.

Since rectilinear sampling is well understood, section 2.3.1 relates the polar PSF behaviour to known concepts of the rectilinear PSF. This section, albeit brief, attempts to give some insight as to how the ringlobes and oscillations arise when sampling on a finite polar grid, and why the ringlobes are asymmetric and decrease in amplitude.

The radial aliasing effects of polar sampling are investigated in section 2.3.2. From the Fourier convolution theorem [3, p.108], we study how the principal polar PSF leads to radial replication and smearing. The concept of an effective field of view or baseband is expounded upon, which leads to the polar radial sampling requirement. Finally, we discuss how the image replicates get folded back (or aliased) into the baseband which can severely corrupt the image.

2.3.1 Polar PSF Intuition

When discussing sampling theory, we invariably talk about rectilinear (Cartesian) sampling. Conceptually, then, it is advantageous to relate the principal polar PSF to the Cartesian PSF. Moreover, the principal polar PSF was derived from the 1D Hankel transform: we therefore develop an intuition based on the 1D Cartesian point spread function.

In section 2.2.2, we assumed sampling at the origin and at M concentric rings spaced by Δk_r (*i.e.* $\Delta k_\theta \rightarrow 0$). For 1D Cartesian sampling, this corresponds to a finite sampling comb of $(2M+1)$ samples which can be expressed as $\sum_{-M}^{M} \delta(k_x - m\Delta k_r)$. The Fourier expansion, and hence the Cartesian PSF, is given by

$$\int_{-\infty}^{+\infty} \left\{ \sum_{m=-M}^{M} \delta(k_x - m\Delta k_r) \right\} \epsilon^{2\pi i x k_x}\, dk_x = \sum_{m=-M}^{M} \epsilon^{2\pi i m x \Delta k_r} = \frac{\sin(\pi[2M+1]x\Delta k_r)}{\sin(\pi x \Delta k_r)} \tag{2.24}$$

which is depicted in Figure 2.5 for $M = 9$.

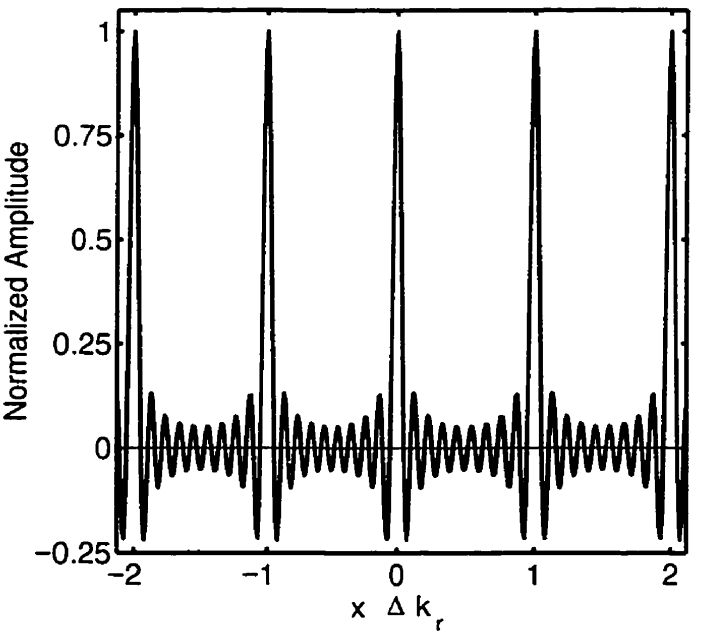

Figure 2.5: Normalized Cartesian PSF
Normalized Cartesian PSF for $M = 9$, i.e. $(2M+1) = 19$ rectilinear sample points.

We next draw some parallels with the principal polar PSF of Eq.(2.13) and Figure 2.2. The first observation is that in both the polar and Cartesian cases, we have replicates at multiples of $1/\Delta k_r$. For Cartesian sampling, the replicates are exact duplicates of the main lobe. For polar sampling, however, the replicates (*i.e.* ringlobes) differ from the main lobe in both shape and amplitude.

A second observation is that M oscillation periods occur between successive replicates: for Cartesian sampling, it is *exactly* M periods, while for polar sampling it is only *approximate*. These oscillations arise because we sample over a limited extent in k-space. This can be understood if we limit the Cartesian sampling comb: $\mathrm{III}(k_x/\Delta k_r) \times \Pi(k_x/[2M\Delta k_r])$. Its FT is of the form $\mathrm{III}(x\Delta k_r) \star \mathrm{sinc}(Mx\Delta k_r)$, where we have used the Fourier convolution theorem. The rect function (Π), then, makes the Cartesian sampling comb finite but gives rise to sinc-like oscillations in the PSF. In general, a finite sampling extent results in oscillations in the PSF, often termed a truncation artifact.

Moreover, because the complex exponentials are purely periodic, Cartesian sampling leads to a coherent summation. In other words, the Cartesian replicates resemble the main lobe in all respects. In contrast, the Bessel functions' non-purely periodic nature leads to destructive interference upon summation. This incoherence creates asymmetric polar ringlobes of decreasing amplitude.

The Cartesian and principal polar PSFs are expressed as summations of complex exponentials and weighted zero-order Bessel functions of the first kind, respectively:

$$\mathrm{PSF}_c \simeq \sum_{m=-M}^{M} \epsilon^{2\pi i m x \Delta k_r} \qquad \mathrm{PSF}_p \simeq \sum_{m=1}^{M} m J_0(2\pi r m \Delta k_r) \tag{2.25}$$

Since both the complex exponentials and Bessel functions are continuous functions of infinite extent and M is finite, their respective PSFs are also continuous and infinite.

Since Cartesian replicates are duplicates of one another, their energy is the same. By analogy, then, we assume that all polar ringlobes have the same energy, even though their amplitudes differ. This can be justified using Eq.(2.22) and realizing that the volume under each ringlobe is given by the Hankel transform of $s_j(\mathbf{r})$ evaluated

at k_r=0: in doing so, one obtains a volume of 2 (arbitrary) units regardless of the ringlobe order j. For equal volumes, then, we assume that their energies must also be equal. If we further assume that each ringlobe is concentrated at a radius $j/\Delta k_r$, then the energy is given by its circumference times its amplitude-squared, namely $2\pi|s_j|^2 j/\Delta k_r$. To obtain a constant energy independent of the ringlobe order, $|s_j|$ must be proportional to $1/\sqrt{j}$, as was stated in section 2.2.2.

The intuition mentioned above, albeit mathematically imprecise, supports (in a hand-waving manner) the concepts developed in section 2.2.2. We next discuss the image effects and artifacts of polar sampling in **k**-space.

2.3.2 Radial Aliasing Effects

Since MR data are discrete, it can be expressed as the multiplication of the continuous k-data $O(\mathbf{k})$ with a sampling function $S(\mathbf{k})$ as $O(\mathbf{k}) \times S(\mathbf{k})$. From the Fourier convolution theorem [3, p.108], the MR image is given by $o(\mathbf{r}) \star s(\mathbf{r})$, where $o(\mathbf{r}) = \mathcal{F}\{O(\mathbf{k})\}$ is the object in the image domain, $s(\mathbf{r}) = \mathcal{F}\{S(\mathbf{k})\}$ is the PSF, and $\star$ represents the convolution operation.

As an example, let the field of view (FOV) be $1/\Delta k_r$ and the object be a circular disk of radius $0.375/\Delta k_r$, as shown in Figure 2.6(a). The effect of sampling with concentric rings spaced by Δk_r is shown in Figure 2.6(b). Note that the limits are $\pm 1.5/\Delta k_r$, *i.e.* we display three times the expected FOV limits of $\pm 0.5/\Delta k_r$: the effect of the main lobe and of the first ringlobe are therefore observable. The salient features of the magnitude image are: (1) the original object appears at the centre, (2) a bright ring surrounds the object at a radius of $0.625/\Delta k_r$, (3) a non-zero, non-constant, low amplitude signal appears between the object and the bright ring, (4) immediately beyond the bright ring, there is a region of almost no signal, (5) beyond this dark band, a shaded region appears out to a radius of $1.375/\Delta k_r$, and (6) the disk's intensity profile is no longer uniform, but rather concave.

These features can be understood if we simplify the principal polar PSF to consist of δ-functions only, since convolution with a δ-function replicates (and scales) the object centred on that particular δ-function. Thus, we simplify the principal polar PSF as follows: let the main lobe be described by a unit-intensity δ-function, and let the first ringlobe be approximated by a ring of negative and positive δ-functions at $1/\Delta k_r - \Delta r$ and $1/\Delta k_r$, respectively, where Δr is the spacing in the image domain ($[2M+1]\Delta r = 1/\Delta k_r$). The intensity of the "δ-rings" are on the order of $2.25/[\pi\sqrt{M\pi}]$.

The convolution of the object with this simplified PSF is readily understood. The central δ-function replicates the object at $r = 0$, which explains salient feature (1). The δ-rings scale, replicate, and distribute the object circularly which produces a "smearing effect". The sum of these smeared replicates yields the image.

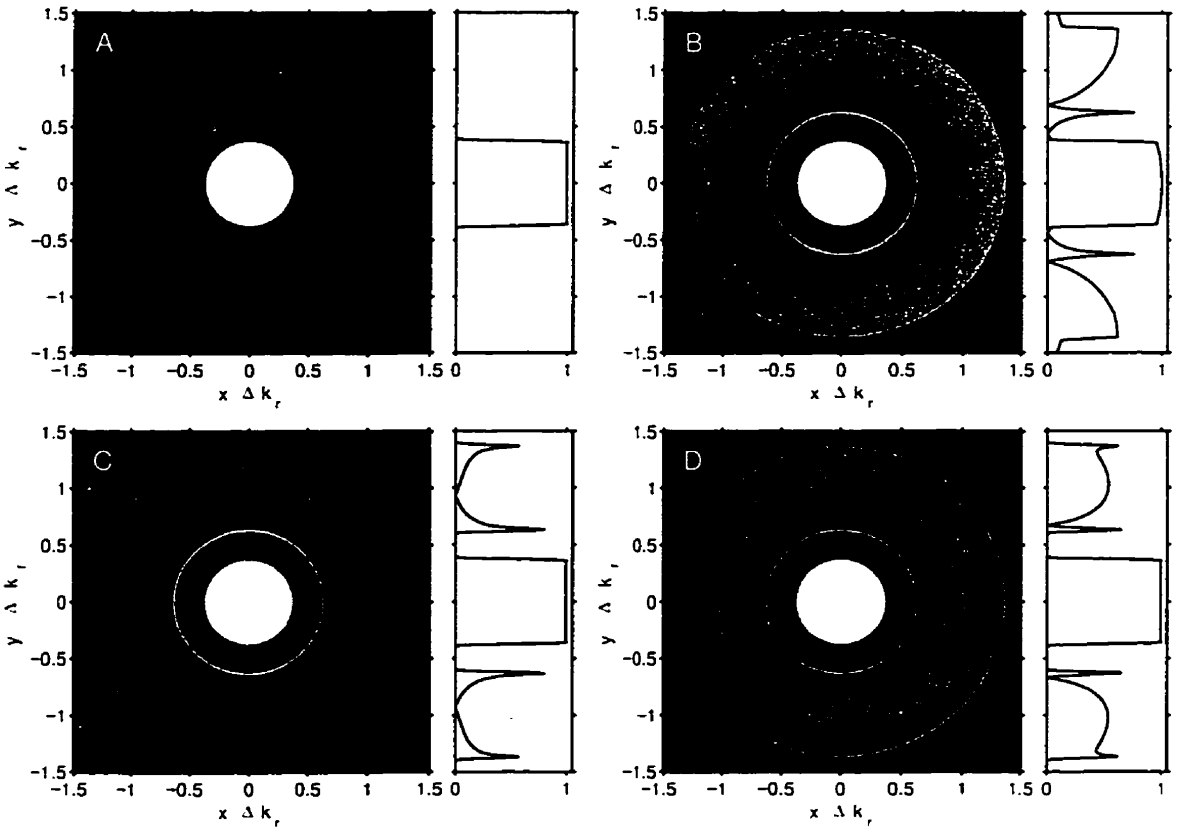

Figure 2.6: Synthetic disk phantom aliasing

Magnitude image and profile of a synthetic disk phantom of radius $0.375/\Delta k_r$. *(a) Original object. (b) Disk convolved with the principal polar PSF. (c) Disk convolved with the simplified PSF consisting of a* δ*-function at* $r=0$, *and two equal intensity but opposite polarity* δ*-rings at* $1/\Delta k_r - \Delta r$ *and* $1/\Delta k_r$. *(d) Disk convolved with the simplified PSF consisting of a* δ*-function at* $r=0$, *and two different intensity and opposite polarity* δ*-rings at* $1/\Delta k_r - \Delta r$ *and* $1/\Delta k_r$. *Note that we display out to three times the effective FOV.*

If the δ-rings have equal intensity but opposite polarity, then the edges of the object will remain intact, as shown in Figure 2.6(c). Since the object is a disk of radius $0.375/\Delta k_r$ and the object gets *smeared* circularly at a radius of $1/\Delta k_r$, the bright edge rings appear at $(1\pm0.375)/\Delta k_r$. This explains the bright ring at $0.625/\Delta k_r$, namely salient feature (2), and why the shaded region appears out to radius of $1.375/\Delta k_r$, as stated in salient feature (5).

To mimic the asymmetry of the ringlobe, the negative δ-ring is given an intensity of about 90% that of the positive δ-ring. This value was chosen since from Figure (2.4), the normalized ringlobe values at $j/\Delta k_r - \Delta r$ and $j/\Delta k_r$ are approximately -0.670 and 0.742, respectively, whose *magnitudes* differ by about 10%. The resultant smeared image appears in Figure 2.6(d). The shading described in salient feature (5) is now clearly present. Furthermore, the asymmetry gives rise to a dark region just beyond the bright ring at $0.625/\Delta k_r$. The asymmetry explains salient features (4) and (5).

Salient features (3) and (6) arise because the true polar PSF is not as simple as a δ-function at $r = 0$ and δ-rings at $r \simeq 1/\Delta k_r$. As mentioned before, the object gets smeared *throughout*. In general, then, sampling on a finite polar grid produces circularly smeared artifacts, circular ringing (a truncation artifact due to sampling over a finite extent), and circular blurring (since the PSF's main lobe has a finite width). However, as the number of ring samples increases, the blurring decreases (since the width of the main lobe decreases), and the amount of ringing also diminishes since one effectively samples over a larger extent in k-space.

One important aspect of convolution to note is that the object being smeared is not rotated as it gets smeared circularly. For example, let the object be an elliptical disk whose major and minor radii are $0.375/\Delta k_r$ and $0.25/\Delta k_r$, respectively, with the major axis in the x-direction. The resultant smeared image appears in Figure 2.7. Note that the bright ring surrounding the object is an ellipse with major and minor radii $(1-0.25)/\Delta k_r$ and $(1-0.375)/\Delta k_r$, respectively, with the major axis in the y-direction. Also, the dark band just beyond this bright ring is no longer circularly

symmetric. Furthermore, the outer shaded region is an ellipse of major and minor radii of $(1+0.375)/\Delta k_r$ and $(1+0.25)/\Delta k_r$, respectively, with the major axis in the x-direction. Now, if the object had been rotated as it was smeared, the bright ring, the dark band, and the outer shaded region would have been circularly symmetric, which is clearly not the case.

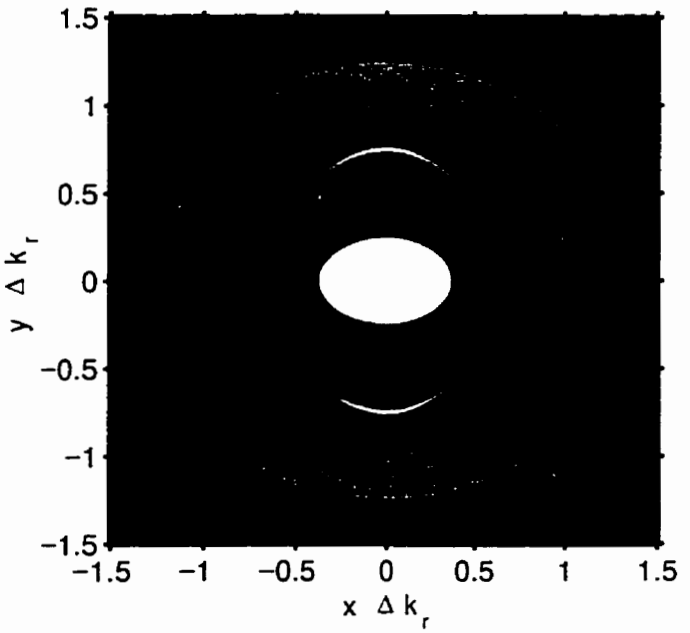

Figure 2.7: Synthetic elliptical phantom aliasing
Magnitude image of a synthetic elliptical phantom convolved with the principal polar PSF. Note that we display out to three times the effective FOV.

Disks and ellipses exhibit circular properties. Therefore, we expect circular smearing effects, as shown in Figures 2.6 and 2.7. If the object is not circular or elliptical, though, the smearing effects assume a more complex pattern.

Since the first ringlobe occurs at $1/\Delta k_r$ and the object gets smeared circularly, the inner edge of the smeared replicate occurs at $(1/\Delta k_r - r_{max})$, where r_{max} is the maximum radial extent of the object. If r_{max} is greater than $0.5/\Delta k_r$, then the replicate appears atop the original object. Thus, the effective FOV (baseband) in polar sampling is a *circle* of radius $0.5/\Delta k_r$. This is analogous to Cartesian sampling with a k_x- and k_y-spacing of Δk_r, where the baseband extends from $-0.5/\Delta k_r$ to

$+0.5/\Delta k_r$: in Cartesian sampling, however, the FOV is *rectangular*.

In the aforementioned examples, the extent r_{max} of the object never exceeded $0.5/\Delta k_r$, the effective polar FOV radius. If, however, the object consists of two disks of radius $0.2/\Delta k_r$ shifted by $0.25/\Delta k_r$ in both the x- and y-directions as depicted in Figure 2.8(a), then r_{max} is about $0.554/\Delta k_r$, which extends beyond the effective FOV radius. The resultant smeared image appears in Figure 2.8(b).

Note that each disk taken separately looks similar to Figure 2.6(b): a bright ring surrounds the disk, followed by a dark band, and a shaded region. These features are centred with respect to the disk in question. The full image, then, is a superposition of two translated smeared disk images. Clearly, the bright rings intersect the disks, *i.e.* part of the replicates emanating from the first ringlobe are *aliased* into the effective field of view.

The polar radial sampling requirement is therefore analogous to the Cartesian sampling criterion: one must sample above the Nyquist rate. In other words, if the radial spacing in k-space is Δk_r, the object must be limited to within a circle of diameter $1/\Delta k_r$ in the image domain to avoid polar aliasing.

However, we have shown that the finite number of samples M leads to an oscillatory behaviour in the PSF. For finite Cartesian sampling, the oscillations are sinc-like, where the zero-crossings are equidistant. This property leads to a coherent summation upon convolution of the Cartesian PSF and the object, and yields the familiar Gibb's ringing artifact in the x- and y-directions.

For finite polar sampling, though, the jinc-like oscillations in the polar PSF have non-equidistant zero-crossings in the radial direction (by virtue of the Bessel functions not being purely periodic). Consequently, the polar PSF produces a radial ringing (or truncation) artifact, but also leads to signal leakage/aliasing: this effect was observed by the appearance of a low non-zero background signal and the disk's intensity assuming a concave rather than uniform pattern.

This means that even if the Nyquist criterion (as defined for Cartesian sampling) is

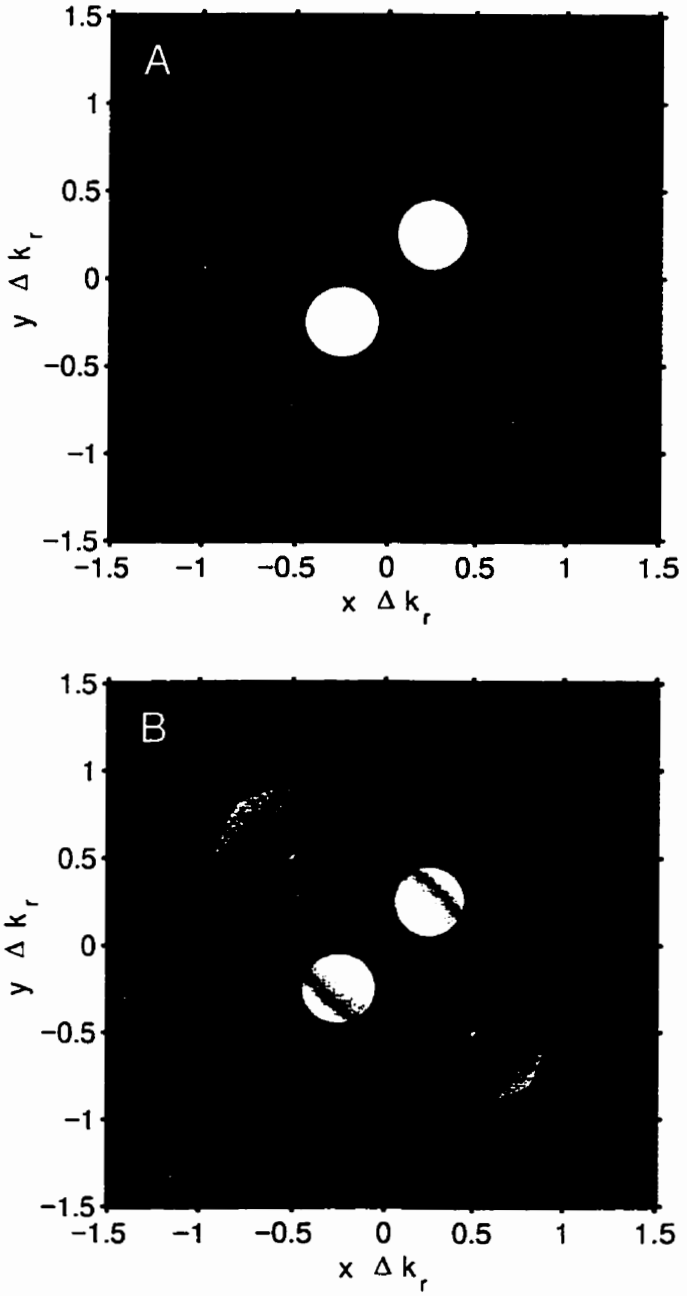

Figure 2.8: Synthetic two-disk phantom aliasing

Magnitude image of a synthetic phantom consisting of two translated disks. (a) Original object. (b) Two translated disks convolved with the principal polar PSF. Note that we display out to three times the effective FOV.

met in the k_r-direction, *i.e.* that the sample spacing Δk_r is such that the radial extent of the object is fully contained within the baseband, the ringlobes will introduce some aliasing (and leakage) artifacts into the image. This occurs because convolution of the object with the ringlobes distributes ringlobe energy into the effective FOV. This is a consequence of the Nyquist criterion being defined *strictly* for Cartesian sampling.

Note that when one considers the sampling as a 2D polar sampling effect, as done here, the Nyquist criterion must be modified and/or generalized. The end result is that the 2D polar sampling effects do not follow the Cartesian Nyquist criterion, and thus some form of polar aliasing and/or leakage artifact results. The amount of aliased signal will depend on the object's size, geometry and intensity, and will vary according to pixel location.

From Eq.(2.20), the principal polar PSF is the sum of the main lobe and the ringlobes, which can be written as $\mathrm{PSF} = \mathrm{PSF}_{s_0} + \mathrm{PSF}_{s_j}$. In so doing, we have

$$\begin{aligned} \mathrm{PSF}_{s_0} &= \frac{\pi(\Delta k_r)^2}{4} + 2\pi(M\Delta k_r)^2\,\mathrm{jinc}(2\pi M r\Delta k_r) \\ \mathrm{PSF}_{s_j} &= 2\pi(\Delta k_r)^2 \sum_{m=1}^{M} m J_0(2\pi r m\Delta k_r) - 2\pi(M\Delta k_r)^2\,\mathrm{jinc}(2\pi M r\Delta k_r) \end{aligned} \quad (2.26)$$

where we have grouped the constant term arising from the δ-sample at the origin with the main lobe. These PSFs appear in Figures 2.3 (minus the additive constant) and 2.9, respectively, for $M = 9$ concentric rings.

The MR image is then given by $o(\mathbf{r}) \star [\mathrm{PSF}_{s_0} + \mathrm{PSF}_{s_j}]$. Since convolution is a linear operator, we can write this as

$$o(\mathbf{r}) \star \mathrm{PSF}_{s_0} + o(\mathbf{r}) \star \mathrm{PSF}_{s_j} = I_0(\mathbf{r}) + I_j(\mathbf{r}) \quad (2.27)$$

where I_0 and I_j are the image components arising from the object convolved with the main lobe PSF and ringlobe PSF, respectively. In terms of energy, we have

$$\begin{aligned} \mathcal{E}_{tot}(\mathbf{r}) &= |I_0(\mathbf{r}) + I_j(\mathbf{r})|^2 = |I_0(\mathbf{r})|^2 + |I_j(\mathbf{r})|^2 + \left[I_0(\mathbf{r})I_j^*(\mathbf{r}) + I_0^*(\mathbf{r})I_j(\mathbf{r})\right] \\ &= \mathcal{E}_0(\mathbf{r}) + \mathcal{E}_j(\mathbf{r}) + \mathcal{E}_{0j}(\mathbf{r}) \end{aligned} \quad (2.28)$$

where $\mathcal{E}_{tot}$, $\mathcal{E}_0$, $\mathcal{E}_j$, and $\mathcal{E}_{0j}$ represent the total energy, the main lobe energy, the ringlobe energy, and the cross-term main lobe/ringlobe energy, respectively, and the $*$

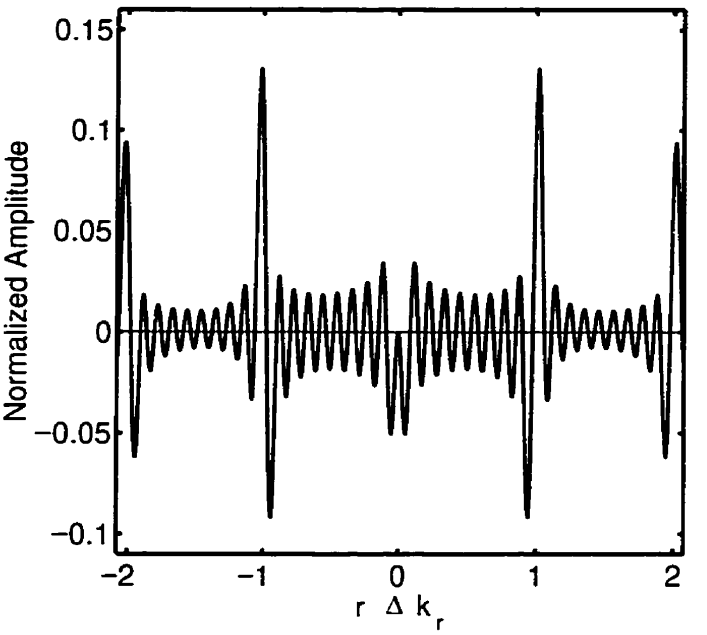

Figure 2.9: Principal polar PSF arising from the ringlobes only
Principal polar PSF arising from the ringlobes only for $M = 9$ concentric rings assuming that the amplitude of the amplitude of the full PSF is normalized to unity.

superscript indicates the complex conjugate. Note that $\mathcal{E}_0$ and $\mathcal{E}_j$ are always positive, while $\mathcal{E}_{0_j}$ can be positive or negative. Also, the energy content is object-dependent: in other words, depending on the object's size and geometry, the energy contributed by each component will vary.

The main lobe energy is given by $\mathcal{E}_0(\mathbf{r})$, while the aliased energy can be determined from $\mathcal{E}_j(\mathbf{r}) + \mathcal{E}_{0_j}(\mathbf{r})$ within the effective FOV of radius $0.5/\Delta k_r$. Similarly, one can determine the total energy contributed by each component within the effective FOV. For example, Table 2.1 summarizes the main and aliased energy contributions for disk phantoms of varying radii sampled on a polar grid. Note that here $\mathcal{E}_{0_j}$ takes on strictly positive values. More importantly, though, is the fact that as the disk radius increases, the expected uniform intensity assumes a concave shape. Note that although we have observed the Nyquist criterion (as described/defined previously) in the k_r-direction, the aliasing can become quite severe for large objects with respect to the field of view.

Table 2.1: Energy components of synthetic disk phantoms
Energy components and values within the baseband for synthetic disk phantoms of varying radii.

Radius	$\mathcal{E}_0$	$\mathcal{E}_j$	$\mathcal{E}_{0j}$	$\mathcal{E}_{tot}$
$0.05/\Delta k_r$	0.995	0.001	0.004	1.000
$0.10/\Delta k_r$	0.979	0.003	0.018	1.000
$0.15/\Delta k_r$	0.956	0.007	0.037	1.000
$0.20/\Delta k_r$	0.919	0.012	0.069	1.000
$0.25/\Delta k_r$	0.877	0.019	0.104	1.000
$0.30/\Delta k_r$	0.828	0.028	0.144	1.000
$0.35/\Delta k_r$	0.757	0.041	0.202	1.000
$0.40/\Delta k_r$	0.685	0.056	0.259	1.000
$0.45/\Delta k_r$	0.580	0.082	0.338	1.000
$0.495/\Delta k_r$	0.471	0.118	0.411	1.000

In summary, the polar sampling effective FOV occurs within a radius of $0.5/\Delta k_r$, where Δk_r is the radial sample spacing in k-space. Since the ringlobes are radial in nature and occur at multiples of $1/\Delta k_r$, the replicates are circularly smeared versions of the original object. Therefore, the object extent must be at least limited to within a radius of $0.5/\Delta k_r$. Because the polar ringlobes are asymmetric and extend into the baseband, the polar radial sampling requirement is more involved than just considering the object's extent.

2.4 Discussion

In MR imaging, a flexible gradient system allows one to cover k-space in virtually any fashion. Depending on the trajectory and velocity of traversal, the acquired k-space samples may be distributed non-rectilinearly. Whenever one samples non-rectilinearly, one must weight each sample point according to the areal extent of the given acquired sample. In effect, the weighting function is designed to compensate for the sampling density.

To gain further insight into the 2D principal polar PSF, we followed Bracewell and Thompson's [20] formalism and decomposed it into its main lobe (whose behaviour is jinc-like), and a series of asymmetric ringlobes peaked near $j/\Delta k_r$ (whose amplitudes decay as j increases).

Since the first ringlobe occurs at a radius of $1/\Delta k_r$, where Δk_r is the radial sample spacing in k-space, the object's extent must be space-limited to within a radius of $0.5/\Delta k_r$. This is the sampling requirement similar to that of Cartesian sampling. However, when sampling on a finite polar grid, the ringlobes are asymmetric, oscillatory, non-periodic, and extend to the origin (*i.e.* they are not localized at multiples of $1/\Delta k_r$). This means that the 2D polar PSF ringlobes replicate a smeared version of the object throughout the baseband. This aliasing/leakage artifact leads to a small non-zero background signal within the baseband.

More importantly, the aliasing affects the overall intensity pattern of the object. In our simulations of a uniform disk phantom, polar aliasing resulted in the disk's intensity assuming a concave pattern. The deviation from a uniform intensity increases as the object occupies more of the FOV. Thus, to minimize aliasing and image corruption within the required FOV, oversampling in the k_r-direction may be necessary. The oversampling factor would depend on the object's extent and on the acceptable tolerance of aliasing.

The concepts of aliasing and leakage are well understood for Cartesian sampling. However, for polar sampling (and perhaps most if not all non-Cartesian sampling

acquisitions), this distinction is no longer clearly obvious. Even if we sample with δ-rings out to infinity, it is not apparent that its 2D PSF is itself a series of concentric δ-rings. Recall that in Cartesian sampling, the concept of aliasing is properly defined because the FT of an infinite series of δ-functions is itself a series of δ-functions. Leakage effects are easily explained and are due to truncation effects, *i.e.* due to the fact that we've sampled over a finite extent. For polar sampling, however, these two concepts are not as easily defined. Consequently, the 2D PSF of polar sampling encompasses a "mixing" of both aliasing and leakage effects, as defined for Cartesian acquisitions. Here, we've opted to call this simply aliasing.

But, the reader is cautioned that, herein, the term aliasing is used in the broadest sense of the word: any high frequency (or spatial) component going under an assumed low frequency (or spatial) component. In Cartesian sampling, leakage (and ringing) effects are remedied via the application of suitable filters (*e.g.* the Hamming window) prior to IFT. However, for polar sampling, these same filters did not correct the observed non-uniform intensity pattern of the reconstructed disk objects. Therefore, we attribute the effect as an aliasing phenomenon, where aliasing is now used in its most general and all-encompassing meaning.

In Cartesian sampling, the effective FOV is a *square* region of full-width $1/\Delta k_r$ for a sample spacing of Δk_r in both the k_x- and k_y-directions. In polar sampling, however, it is a *circular* region of diameter $1/\Delta k_r$. In effect, then, the polar FOV area is about 78.5% that of the Cartesian FOV for commensurate sample spacing and image pixel size. For comparable FOVs, the number of samples may have to be increased. On the other hand, certain polar sampling schemes (*e.g.* spiral acquisitions) allow more efficient coverage of k-space for a fixed gradient capability which may offset the increase in samples required. Furthermore, azimuthal sampling effects have not been addressed here: it may be that non-equidistant azimuthal sampling offer significant advantages in reducing aliasing effects.

Another important aspect of polar sampling, and any other k-space sampling

scheme for that matter, is the signal-to-noise-ratio (SNR). Pipe and Duerk [23] have analyzed the estimator variances for various sampling schemes, from which the SNR is given by $1/\sqrt{\text{variance}}$. Using [23, Eq.42], the polar sampling variance with respect to Cartesian sampling is given by $[4N+2]/[3N+3]$, where N is the number of readouts of duration T with M samples per readout; here, we assumed that T, M and N are the same for polar and Cartesian sampling. As N gets large, the polar variance approaches 4/3, from which the SNR tends to $\sqrt{3}/2=0.866$, where we have normalized the Cartesian SNR at 1.0. Thus, polar sampling has an inherently lower SNR than Cartesian sampling, all else being equal.

In clinical applications, however, polar sampling (and other non-rectilinear sampling schemes) offer some advantages in motion artifact suppression. Although SNR and aliasing are important considerations, the benefits of non-rectilinear sampling schemes (both radially and azimuthally) in terms of motion suppression may outweigh these disadvantages. Only further work in this area will clarify these tradeoffs.

2.5 References

[1] J.W. Cooley, J.W. Tukey. An algorithm for the machine computation of complex Fourier series. *Math. Comput.* **19**. 297–301 (1965).

[2] E.O. Brigham. "The Fast Fourier Transform". Prentice-Hall. Englewood Cliffs. N.J.. 1974.

[3] R.N. Bracewell. "The Fourier Transform and its Applications". McGraw Hill. New York. 1986.

[4] C.B. Ahn. J.H. Kim. Z.H. Cho. High-speed spiral-scan echo planar NMR imaging. *IEEE Trans. on Med. Imag.* **5(1)**. 2–7 (1986).

[5] E. Yudilevich. H. Stark. Spiral sampling: theory and an application to magnetic resonance imaging. *J. Opt. Soc. Amer. A* **5(4)**. 542–553 (1988).

[6] C.H. Meyer. B.S. Hu. D.G. Nishimura. A. Macovski. Fast spiral coronary artery imaging. *Magn. Reson. Med.* **28**. 202–213 (1992).

[7] P.C. Lauterbur. Image formation by induced local interactions: examples employing nuclear magnetic resonance. *Nature* **242**. 190–191 (1973).

[8] L.D. Hall. S. Sukumar. Rapid data-acquisition technique for NMR imaging by the projection-reconstruction method. *J. Magn. Reson.* **56**. 179–182 (1984).

[9] G.H. Glover. J.M. Pauly. K.M. Bradshaw. Boron-11 imaging with a three-dimensional reconstruction method. *J. Magn. Reson. Imag.* **2(1)**. 47–52 (1992).

[10] S. Matsui. H. Kohno. NMR imaging with a rotary field gradient. *J. Magn. Reson.* **70**. 157–162 (1986).

[11] R.H.T. Bates. T.M. Peters. Towards improvements in tomography. *N.Z. J. Sci.* **14**. 883–896 (1971).

[12] P.R. Smith. T.M. Peters. R.H.T. Bates. Image reconstruction from finite numbers of projections. *J. Phys. A: Math. Nucl. Gen.* **6**. 361–382 (1973).

[13] W.N. Brouw. Aperture synthesis. *in* "Methods in Computational Physics. volume 14" (B. Alder. S. Fernbach. and M. Rotenberg. Eds.). pp. 131–175. Academic Press. New York. 1975.

[14] F.R. Schwab. Optimal gridding visibility data in radio interferometry. *in* "Indirect Imaging". (J.A. Roberts. Ed.). pp. 333–346. Cambridge University Press. New York. 1983.

[15] J.D. O'Sullivan. A fast sinc function gridding algorithm for Fourier inversion in computer tomography. *IEEE Trans. on Med. Imag.* **4(4)**. 200–207 (1985).

[16] J.I. Jackson. C.H. Meyer. D.G. Nishimura. A. Macovski. Selection of a convolution function for Fourier inversion using gridding. *IEEE Trans. on Med. Imag.* **10(3)**. 473–478 (1991).

[17] H. Stark. Sampling theorems in polar coordinates. *J. Opt. Soc. Amer.* **69(11)**. 1519–1525 (1979).

[18] H. Stark. C.S. Sarna. Image reconstruction using polar sampling theorems. *Appl. Opt.* **18(13)**. 2086–2088 (1979).

[19] H. Stark. M. Wengrovitz. Comments and corrections on the use of polar sampling theorems in CT. *IEEE Trans. on Acoust. Speech Sign. Proc.* **31(5)**. 1329–1331 (1983).

[20] R.N. Bracewell. A.R. Thompson. The main beam and ringlobes of an east-west rotation-synthesis array. *Astrophys. J.* **182**. 77–94 (1973).

[21] P.A.M. Dirac. "The Principles of Quantum Mechanics. 4^{th} Edition". Clarendon Press. Oxford. 1958.

[22] I.S. Gradshteyn. I.M. Ryzhik. "Table of Integrals. Series. and Products". Academic Press. New York. 1980.

[23] J.G. Pipe. J.L. Duerk. Analytical resolution and noise characteristics of linearly reconstructed magnetic resonance data with arbitrary k-space sampling. *Magn. Reson. Med.* **34**. 170–178 (1995).

Chapter 3

Reconstruction Effects

3.1 Introduction

Magnetic resonance images are most commonly calculated from the inverse Fourier transform (IFT) of the acquired **k**-space data. Since the data are discrete as opposed to continuous, the sampling process may introduce image artifacts. Also, these artifacts may depend on the reconstruction algorithm used. For uniform **k**-space polar sampling, *i.e.* equally-spaced radial and azimuthal samples, the images may be reconstructed using either the gridding algorithm [1, 2, 3, 4] or the convolution backprojection algorithm [5, 6, 7].

Gridding is a general reconstruction algorithm which can be used for any non-Cartesian sampling scheme. Convolution backprojection, however, applies mostly to data sampled on a purely polar grid, although other polar-type acquisitions can be reconstructed with this algorithm (*e.g.* CT fan-beam, and CT cone-beam acquisitions).

These two algorithms offer different tradeoffs regarding image resolution, signal-to-noise ratio (SNR), and aliasing in the reconstructed image. Since these effects may (adversely) influence the appearance and subsequent analysis of the image content, the choice of reconstruction algorithm is important. The purpose of this chapter is to compare the resolution, SNR, and aliasing characteristics of these two reconstruction algorithms for polar **k**-space sampling.

For polar **k**-space sampling, the discretization occurs in both the radial and az-

imuthal directions. Consequently, the aliasing can occur in both the radial and azimuthal directions. Here, we focus primarily on radial sampling issues since one typically samples finely enough in the azimuthal direction to avoid azimuthal aliasing. We do, however, make some cursory statements about azimuthal sampling considerations and artifacts.

In the Theory section, we analyze the modulation transfer function (MTF), the SNR, and the aliasing effects of equally-spaced radial and azimuthal polar MR data reconstructed using both gridding and convolution backprojection. In the Tradeoffs section, we discuss the tradeoffs of gridding versus convolution backprojection. We also discuss practical SNR improvements with either reconstruction method. Experimental verification of the theory is presented in the Results section. In the Non-Equidistant k_r Sampling section, we discuss the potential benefits of a hybrid gridding and convolution backprojection reconstruction applicable to radially non-equidistant but azimuthally equidistant polar **k**-data.

3.2 Theory

3.2.1 Gridding

Gridding (GRD) is a general purpose Fourier reconstruction algorithm. It is flexible in that any non-Cartesian samples are interpolated onto a Cartesian (rectilinear) grid and then transformed using the rapid and efficient fast Fourier transform (FFT) [8], which operates on discrete data.

Algorithm Description

Let us assume that the MR magnetization in n-dimensional k-space is given by $M(\mathbf{k})$. In the acquisition process, we sample the magnetization (either rectilinearly or not) via the function $S(\mathbf{k})$, which consists of *unit area* δ-functions at the appropriate locations in k-space. The acquired sampled magnetization is given by

$$M_s(\mathbf{k}) \;=\; M(\mathbf{k})\, S(\mathbf{k}) \tag{3.1}$$

Since the k-space sampling density may be non-uniform for some general acquisition k-trajectory, each sample at location $\mathbf{k}$ is weighted by its areal extent, say $W(\mathbf{k})$. The sampled and weighted magnetization is then interpolated (*i.e.* regridded) onto a Cartesian k-space grid via convolution and resampling, namely

$$M_{swcs}(\mathbf{k}) \;\equiv\; \left\{ [M_s(\mathbf{k})\, W(\mathbf{k})] \star C(\mathbf{k}) \right\} \times \frac{1}{\Delta\mathbf{k}} \text{Ш}\left(\frac{\mathbf{k}}{\Delta\mathbf{k}}\right) \tag{3.2}$$

where $C(\mathbf{k})$ is the interpolating function, $\frac{1}{\Delta\mathbf{k}} \text{Ш}\left(\frac{\mathbf{k}}{\Delta\mathbf{k}}\right)$ is the n-dimensional Cartesian sampling function of spacing $\Delta\mathbf{k}$ in the $\mathbf{k}$ directions, $\star$ denotes convolution and $\times$ denotes multiplication.

The computationally efficient inverse FFT is then used to reconstruct the regridded MR image, say $I_{grd}(\mathbf{r})$. However, by the Fourier convolution theorem [9, p.108], convolution with $C(\mathbf{k})$ in Fourier space implies apodization by $c(\mathbf{r})$ in image space, where $c(\mathbf{r})$ is the IFT of $C(\mathbf{k})$. To undo this effect, one needs to divide the IFT of

$M_{swcs}(\mathbf{k})$ by $c(\mathbf{r})$, so that

$$I_{grd}(\mathbf{r}) = \frac{1}{c(\mathbf{r})} \mathcal{F}^{-1}\left\{M_{swcs}(\mathbf{k})\right\} \tag{3.3}$$

Modulation Transfer Function

It is customary to describe an imaging system by its frequency response, also known as its transfer function [10]. The transfer function provides a useful measure of the system's behaviour and allows for a direct comparison between systems.

If the input to a linear system is $f(\mathbf{r})$, linear systems theory predicts the output to be $f(\mathbf{r}) * p(\mathbf{r})$, where $p(\mathbf{r})$ is the point spread function (PSF) of the system, *i.e.* the response to an impulse function. In frequency space this becomes $F(\mathbf{k})\,P(\mathbf{k})$, where $F(\mathbf{k})$ and $P(\mathbf{k})$ are the Fourier transforms of $f(\mathbf{r})$ and $p(\mathbf{r})$, respectively. The transfer function $P(\mathbf{k})$ describes how each frequency is modulated according to $|P(\mathbf{k})|\,e^{i\phi_p(\mathbf{k})}$. More specifically, $|P(\mathbf{k})|$ and $\phi_p(\mathbf{k})$ are the modulation (MTF) and phase transfer functions, respectively. Note that if the PSF is a real and even function, then the transfer function is purely real, whereby the phase transfer function can only assume values of 0 or π. This is the case with GRD (and convolution backprojection) of polar k-space data, and so an MTF analysis suffices.

For a point object, $M(\mathbf{k})$ is unity over all of k-space. Consequently, $M_s(\mathbf{k})$ is unity at all discrete locations in Eq.(3.2), and $M_{swcs}(\mathbf{k})$ is also unity at each regridded Cartesian k location, even though the sampling density is non-uniform. In other words, after regridding (interpolation and resampling) the energy per unit area is constant; this is a consequence of the $W(\mathbf{k})$ weighting directly compensating for the variable sampling density. In the particular case of purely polar sampling, the ramp weighting leads to the GRD algorithm's MTF being unity throughout the acquisition region, *i.e.* within the radial frequency range $[0, k_r^{max}]$, where $k_r^{max} = \frac{1}{2} N_r \Delta k_r$.

The theoretical MTF expectations for GRD reconstruction of polar k-data were verified via numerical simulations. Analytical k-space values of noise-free image domain *sinusoidal* bar phantoms were calculated. All synthetic phantoms were derived

from assumed unit amplitude (x-directional) sinusoids given by $1 + \sin\left(\frac{2\pi x N_c}{\mathrm{FOV}}\right)$, where x is within the range $\pm\mathrm{FOV}/2$, and N_c is the number of sinusoid cycles per FOV (field of view). To avoid leakage artifacts, N_c was chosen to be an *integral* number of cycles. The reconstructed bar phantom amplitude for $N_c = 1$ was then normalized to unity, and all other reconstructed N_c phantoms were scaled accordingly. Thus, the relative amplitudes of the reconstructed sinusoidal bar phantoms yielded the MTF values directly. To avoid any beat frequency effects, N_c was chosen to be a factor of N_r, the number of discrete image points per FOV. For example, with $N_r = 192$, the available N_c values were $\{1,2,3,4,6,8,12,16,24,48\}$. The measured synthetic sinusoid amplitudes (MTF values) were 1.00 ± 0.01.

Signal-to-Noise Ratio

In any real physical system, the true signal is accompanied by noise which corrupts the image. In MRI, it is the measured **k**-data which include a noise term, say $\eta(\mathbf{k})$. We assume that $\eta(\mathbf{k})$, the input noise function, is a zero-mean complex uncorrelated Gaussian additive stochastic quantity with standard deviation σ. Note that such noise is strictly true only in the case of an ideal low pass (rectangular) analog-to-digital acquisition filter. Under this assumption, the duration time of acquisition (T_{acq}) scales the expectation value according to

$$E\left[\eta(\mathbf{k}_1)\,\eta^*(\mathbf{k}_2)\right] = \frac{\sigma^2}{T_{acq}}\,\delta_{\mathbf{k}_1,\mathbf{k}_2} \tag{3.4}$$

where $\delta_{i,j}$ is the Kronecker delta, and the $*$ superscript denotes the complex conjugate. Under these conditions, and the underlying assumption that the samples are acquired with constant dwell time, Pipe [11] has shown that the variance (per unit **k**-space coverage) of the reconstructed noise is given by

$$\mathrm{var} = \frac{\sigma^2}{T_{acq}\,\mathrm{Area}_k^2}\int_{\mathbf{k}} |W(\mathbf{k})|^2\, d\mathbf{k} \tag{3.5}$$

where $W(\mathbf{k})$ is the GRD weighting function, and Area_k is the entire area of **k**-space covered during data acquisition. For 2D purely polar sampling, the product of the

sampling and weighting functions, *i.e.* $S(\mathbf{k})W(\mathbf{k})$, is given by

$$\sum_{n=0}^{N_a-1} \sum_{m=-N_r/2}^{N_r/2-1} \delta(k_x - m\Delta k_r \cos n\Delta k_\theta,\ k_y - m\Delta k_r \sin n\Delta k_\theta)\ |m|\,(\Delta k_r)^2 \Delta k_\theta \quad (3.6)$$

As expected, the weighting for the $[N_r \times N_a]$ polar samples depends on the radial location $|m|\,\Delta k_r$, which is the ramp filter. Note that we have N_a azimuthal samples within 0–π to be consistent with the convolution backprojection convention, namely $\Delta k_\theta = \frac{\pi}{N_a}$.

Although the ramp filter may not be the "optimal" weighting function (in terms of noise reduction and smoothing), it is the most intuitive one and can be directly compared to convolution backprojection using the Ram-Lak (ramp) filter [12]. An apodized ramp filter of the form $\mathcal{A}(k_r)|m\,\Delta k_r|$ may prove more beneficial in practice, although this would alter the GRD MTF. Here, though, we deal strictly with the unapodized ramp filter, namely $\mathcal{A}(k_r) = 1$, from which the GRD variance per unit k-space coverage is given by

$$\mathrm{var}_{grd} = \frac{\sigma^2 \sum_n \sum_m [\mathcal{A}(k_r)|m|\,(\Delta k_r)^2 \Delta k_\theta]^2}{T_{acq}\left[\pi(N_r \Delta k_r/2)^2\right]^2} \simeq \frac{4\sigma^2}{3\,T_{acq}\,N_r N_a} \quad (3.7)$$

Since the normalized SNR is given by the reciprocal of the square-root of the variance, we obtain

$$\mathrm{SNR}_{grd} \simeq \frac{\sqrt{3\,T_{acq}\,N_r N_a}}{2\sigma} \quad (3.8)$$

Note that this effectively represents the SNR *per unit voxel volume*. According to Edelstein [13] and Macovski [14], the SNR scales as the voxel volume Δv, given by $\Delta v = \Delta x\,\Delta y\,\Delta z$ with Δz the slice thickness. Thus,

$$\mathrm{SNR}_{grd} \simeq \frac{\Delta v\sqrt{3\,T_{acq}\,N_r N_a}}{2\sigma} \quad (3.9)$$

Experimental verification of the $\sqrt{T_{acq}}$ and Δv dependences are given in the Results section.

Aliasing

Since the magnetization is sampled via $S(\mathbf{k})$, the **k**-data are discrete as opposed to continuous, and the reconstructed image is the true image convolved with the point spread function, which is the IFT of $S(\mathbf{k})W(\mathbf{k})$. The process of discretization, then, can potentially lead to aliasing artifacts.

For finite extent polar sampling, the principal polar PSF can be determined by considering $\frac{1}{2}N_r$ concentric *rings* spaced by Δk_r, as previously shown in the Sampling Effects chapter of this treatise. Using the formalism of Bracewell and Thompson [15], Lauzon and Rutt [16] have shown that the polar PSF is given by the spin integration of $v(r)$, where $v(r)$ is the 1D IFT of the discrete (as opposed to continuous) ramp filter, which is the weighting function of Eq.(3.6). Thus,

$$\begin{aligned} v(r) &= \mathcal{F}^{-1}\left\{W(k_r)\right\} = \mathcal{F}^{-1}\left\{\sum_{m=-N_r/2}^{N_r/2} |m\Delta k_r|\ \delta(k_r - m\Delta k_r)\right\} \\ &= \frac{(N_r\Delta k_r)^2}{4}\left[2\,\mathrm{sinc}(r N_r\Delta k_r) - \mathrm{sinc}^2\left(\frac{1}{2}r N_r\Delta k_r\right)\right] \star \Delta k_r \coprod\!\!\coprod (r\Delta k_r) \\ &= \frac{(N_r\Delta k_r)^2}{4}\sum_{j=-\infty}^{\infty}\left\{2\,\mathrm{sinc}\left(\left[r-\frac{j}{\Delta k_r}\right] N_r\Delta k_r\right) - \right. \\ &\qquad \left. \mathrm{sinc}^2\left(\frac{1}{2}\left[r-\frac{j}{\Delta k_r}\right] N_r\Delta k_r\right)\right\} \end{aligned} \tag{3.10}$$

where $\mathcal{F}^{-1}$ denotes the IFT operator, and $\mathrm{sinc}(\xi) \equiv \frac{\sin(\pi\xi)}{\pi\xi}$. The spin integration of $v(r)$, denoted $\mathcal{Q}\{v(r)\}$, is identical to backprojecting $v(r)$ continuously (as opposed to discretely) at all angles from 0 to π. In doing so, we obtain the principal polar PSF, namely

$$\mathrm{PSF}_{grd} = s_0(r) + \sum_{j=1}^{\infty} s_j(r) \qquad \begin{cases} s_0(r) = \mathcal{Q}\{v_0(r)\} \\ s_j(r) = \mathcal{Q}\{v_{+j}(r) + v_{-j}(r)\} \end{cases} \tag{3.11}$$

where $s_0(r)$ and $s_j(r)$ are the main lobe and ringlobes, respectively, $\mathcal{Q}$ is the spin integration operator, and $v_j(r)$ is one term of Eq.(3.10) at that particular j value.

Upon evaluation, $s_0(r)$ behaves as $\frac{J_1(\pi r N_r\Delta k_r)}{\pi r N_r\Delta k_r}$ (the *jinc* function [9, p.249]) which is the circular analog of the *sinc* function. It describes the blurring effect of

having sampled over a *finite* extent. The ringlobes $s_j(r)$ are oscillatory and asymmetrical in the radial direction, with their peak amplitude occurring near $\frac{j}{\Delta k_r}$. The ringlobe peak amplitudes decay with the ringlobe order as $\frac{1}{\sqrt{j}}$. The reader is referred to the Sampling Effects chapter of this treatise for a more in-depth analysis of the characteristics of the polar PSF main lobe and ringlobes.

The resultant image, then, is a summation of the true object convolved with (1) the main lobe $s_0(r)$ which replicates the object at $r=0$ and blurs it due to finite sampling, and (2) with the ringlobes $s_j(r)$ which smear the object azimuthally and radially at multiple radii $\frac{j}{\Delta k_r}$. Furthermore, if the k-space values are not sufficiently sampled in the azimuthal direction, then streak artifacts (azimuthal aliasing) will also result. To avoid this type of aliasing, one requires $N_a \geq \frac{1}{2}\pi N_r$.

Although GRD is an optimized interpolation and reconstruction technique (with the appropriate choice of convolution function), it does not correct for the original sampling effects [4]. In other words, the 2D polar PSF in Eq.(3.11) affects the aliasing at a level that is not remedied using GRD. In practice, the regridded k-data are subsampled (say by the factor 'ovr') onto a finer Cartesian k-grid. Upon IFT, the resultant image FOV is larger by the same factor 'ovr'. The true object is then cropped from the central $\left(\frac{1}{\text{ovr}}\right)^{th}$ region. This subsampling process minimizes any aliasing from the re-interpolation and subsequent IFT, but it does NOT correct for the inherent aliasing effects incurred during acquisition.

Consequently, the overall signal amplitude pattern of the object may be compromised, as shown in Figure 3.1: as the object becomes larger relative to the FOV, the aliasing leads to a greater deviation of the signal amplitude profile pattern. The GRD images were regridded using the Kaiser-Bessel window function (an approximation to the Prolate Spheroidal Wave Function of zero order) given by $I_0\left(\beta\sqrt{1-\left(\frac{2k}{L}\right)}\right)$, with parameters $L=4$, $\beta=12$, and a subsampling factor of ovr=2. These parameters apply to both the k_x and k_y directions, and for all GRD reconstructions within this study. These parameters were chosen in such a manner to minimize uniformity deviations

(in the least-squares sense) of an expected uniform synthetic disk phantom occupying 50% of the FOV. We fixed the oversampling parameter to ovr=2, and varied L and J within 3–6 and 6–20, respectively. Within this range of parameters, the measured uniformity deviations were similar, which suggests that the gridding reconstruction is not overly sensitive to the choice of the L and J parameters.

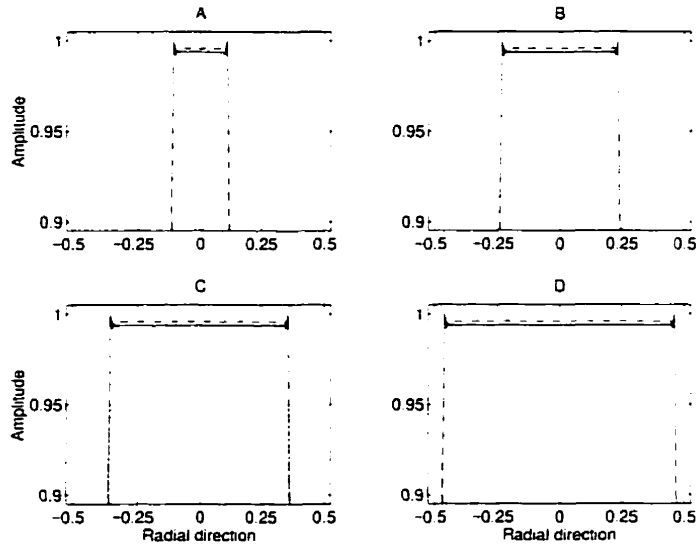

Figure 3.1: Synthetic, uniform disk profiles using GRD and CBP

Synthetic, noise-free, uniform disk profiles of reference Cartesian k*-data reconstructed with the FFT (solid), and of polar* k*-data reconstructed using GRD (dotted) or CBP (dashed). The GRD reconstruction kernel parameters can be found in the text. The radial axes are in units of the FOV. The profiles are for disk diameters of (a) 25% of the FOV, (b) 50% of the FOV, (c) 75% of the FOV, and (d) 95% of the FOV. Note the increasing non-uniform profile signal amplitude for GRD as the object size increases, an aliasing effect arising from the ringlobes $s_j(r)$.*

The sampling effects of purely polar sampling can be minimized if one sinc interpolates in the radial k_r direction prior to regridding. This is most easily accomplished by taking the 1D IFT of the radial k_r–lines, zero-padding to twice their length, and Fourier transforming back to k-space. Gridding can then be used by applying the discrete ramp weighting (whose spacing is now $\frac{1}{2}\Delta k_r$). In this case, the polar PSF is given by $s_0(r)+\sum_{j=1}^{\infty} s_{2j}(r)$. Since the first ringlobe $s_1(r)$ and all odd-order ringlobes have been eliminated, the reconstructed image has reduced aliasing.

For example, an object occupying 95% of the FOV may deviate from its true signal amplitude pattern by as much as 20% if GRD is performed on the original k-data, as shown in Figure 3.1(d). However, by sinc interpolating in the k_r direction by a factor of 2 *prior* to gridding, the signal amplitude deviations are within 1% owing to the reduced aliasing. Similarly, by sinc interpolating in the k_r direction by a factor of 4 *prior* to gridding, the deviation is within 0.1% for the same object since the polar PSF now consists of the main lobe and every 4^{th} ringlobe, *i.e.* $s_0(r)+\sum_{j=1}^{\infty} s_{4j}(r)$. For general non-Cartesian sampling schemes, though, sinc interpolation in the k_r direction may not be practical nor possible.

3.2.2 Convolution Backprojection

The convolution backprojection (CBP) algorithm has been used extensively in computed tomography (CT). Although CT acquires data in the image domain (*i.e.* real projections through the object), one can show using the central slice theorem [17] that this is equivalent to polar sampling in k-space. Furthermore, CBP may be applied to (noisy) complex projections since one can reconstruct the real and imaginary components independently. Therefore, CBP has potential applications to MR reconstruction.

Algorithm Description

The reconstructed MR image is given by the inverse Fourier transform of the sampled magnetization, $M_s(\mathbf{k})$. If one expresses the Fourier variables in polar notation, namely ($k_x = k_r \cos k_\theta$, $k_y = k_r \sin k_\theta$), the polar sampled magnetization can be written as

$$\begin{aligned} M_s(k_r, k_\theta) &= \sum_{n=0}^{N_a-1} \sum_{m=-N_r/2}^{N_r/2-1} M(k_r, k_\theta)\, \delta(k_r - m\Delta k_r,\ k_\theta - n\Delta k_\theta) \\ &\equiv \sum_n \sum_m M_n(m\,\Delta k_r)\, \delta(k_r - m\Delta k_r,\ k_\theta - n\Delta k_\theta) \end{aligned} \tag{3.12}$$

where $M_n(m\Delta k_r)$ is the magnetization sampled in the k_r direction at angle $n\Delta k_\theta$. With the use of Eq.(3.29) from Appendix A, the reconstructed CBP image is

$$I_{cbp}(x, y) = \sum_{n=0}^{N_a-1} B\left\{\mathcal{F}^{-1}\left[M_n(m\,\Delta k_r)\right] \star C_{cbp}(r)\right\} \tag{3.13}$$

where B is the backprojection operator, $C_{cbp}(r)$ is the discrete convolution function sampled at spacing $\Delta r = \dfrac{1}{N_r \Delta k_r}$, and the term being backprojected is the discrete convolved MR "projection" at angle $n\Delta k_\theta$. The image is summed over all N_a convolved projections being backprojected at the desired Cartesian (x, y) locations.

The convolution function is effectively given by the sampled IFT of the finite *continuous* (as opposed to discrete) ramp filter $|k_r|$. To reduce high frequency leakage effects, this filter is often apodized by $\mathcal{A}(k_r)$ so that in general C_{cbp} is given by the

following:

$$C_{cbp}(r) = \mathcal{F}^{-1}\left\{\mathcal{A}(k_r)|k_r|\prod\left(\frac{k_r}{N_r\Delta k_r}\right)\right\} \times \frac{1}{\Delta r}\coprod\left(\frac{r}{\Delta r}\right) \tag{3.14}$$

where $\prod(\xi)=1$ for $|\xi|\leq\frac{1}{2}$ and zero otherwise.

For a direct comparison of the CBP and GRD algorithms, we limit ourselves to the ramp filter (known as the Ram-Lak filter in the CT community) whereby $\mathcal{A}(k_r)=1$, in analogy to the GRD case. A brief overview of the tradeoffs of apodized ramp filters is discussed in the Tradeoffs section. The CBP reconstruction algorithm may be applied to any type of purely polar **k**-data, be it Hermitian, anti-Hermitian, or non-Hermitian (see Appendix A).

Modulation Transfer Function

The convolution backprojection MTF is dependent on three factors: (1) the convolution function $C_{cbp}(r)$ which weights the projections (in the image domain), (2) the interpolation function used in the backprojection stage, and (3) the resampling onto the image grid.

The interpolation arises because each desired image (x, y) location corresponds to a given projected location onto the 1D convolved MR projection vector at angle $n\Delta k_\theta$. These projected locations may or may not coincide with an actual MR projection sample located at $\frac{p}{N_r\Delta k_r}$, with $p=\left\{-\frac{N_r}{2},\ldots,\frac{N_r}{2}-1\right\}$. Thus, some interpolation is required so that the appropriate MR projection value is backprojected to each desired image pixel location.

Various filter (apodized ramp) functions and their convolution counterparts appear in Jain [18, Ch.10], although we will only analyze the case for the Ram-Lak (unapodized ramp) filter [12]. Of course, the analysis below follows readily for any filter function. In the case of the Ram-Lak filter, $C_{cbp}(r)$ of Eq.(3.14) is easily calculated and the coefficients are given in Appendix B.

After discrete convolution of the projections with $C_{cbp}(r)$, one must backproject these onto the image grid: this requires both interpolation and resampling. One of

the more computationally efficient and commonly used interpolation techniques is linear interpolation, which is assumed here. It can be expressed as a convolution (in the image domain) with a triangle function of width $2\Delta r = \frac{2}{N_r \Delta k_r}$. In **k**-space, this corresponds to a modulation of $\text{sinc}^2\left(\frac{k_r}{N_r \Delta k_r}\right)$.

The convolved interpolated projection is then backprojected and resampled onto the desired image locations. This resampling leads to some form of wraparound in the 2D **k**-space, the details of which can be found in Appendix B.

The CBP algorithm's MTF can be calculated for large N_a ($N_a \geq 16 N_r$) with $M_n(m\,\Delta k_r) = 1$ for all m. In this case the MR projections, $\mathcal{F}^{-1}\left\{M_n\right\}$, are given by a single impulse function at $r = 0$. Reconstruction of these data yields the algorithm's PSF since we expect to reconstruct a point at the image centre. Finally, the Fourier transform magnitude of the PSF gives the MTF.

The Ram-Lak MTF contour is given in Figure 3.2(a). For comparison, that of the Shepp-Logan filter (an apodized ramp) is also shown in Figure 3.2(c). Note that the MTFs are *not* circularly symmetric, nor are they confined to a circle of diameter $N_r \Delta k_r$, even though the acquired data are within that circle. These effects arise because of the interpolation and resampling during backprojection, as discussed in Appendix B. However, at low spatial frequencies these MTFs can be approximated by the circularly symmetric functions $\text{sinc}^2\left(\frac{k_r}{N_r \Delta k_r}\right)$ and $\text{sinc}^3\left(\frac{k_r}{N_r \Delta k_r}\right)$, respectively. These approximations are also depicted in Figures 3.2(b) and (d), respectively.

The MTF values were verified with simulations. The synthetic phantom **k**-values were calculated in the same manner as that for GRD (see section 3.2.1), and the images were reconstructed using the CBP algorithm. The theoretical MTF values *on axis* for $N_r = 192$, and N_c assuming values of {1,2,3,4,6,8,12,16,24,48} are {1.000,0.999,0.998,0.998,0.996,0.994,0.988,0.979,0.955,0.848}, respectively. The measured synthetic sinusoid amplitudes (the MTF values) were within ±2% of these theoretical values.

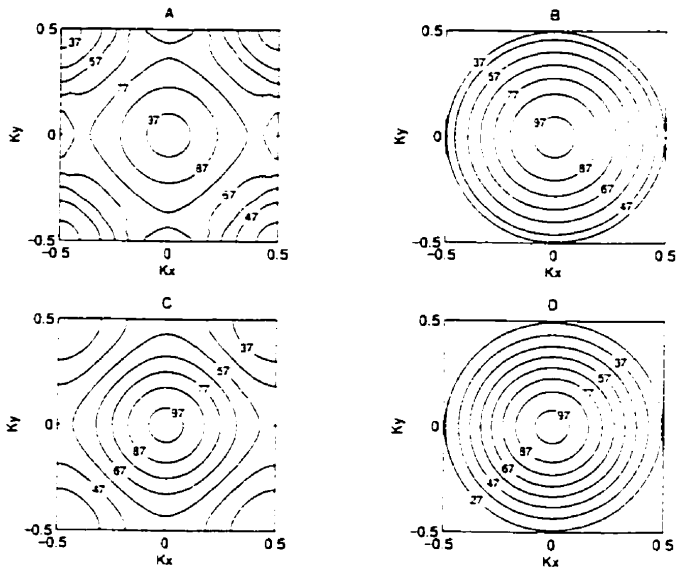

Figure 3.2: Convolution backprojection MTFs

Contour percentages of CBP MTFs. The axes are in units of $N_r \Delta k_r$. (a) True MTF using the Ram-Lak filter. (b) Truncated $sinc^2\left(\frac{k_r}{N_r \Delta k_r}\right)$. (c) True MTF using the Shepp-Logan filter. (d) Truncated $sinc^3\left(\frac{k_r}{N_r \Delta k_r}\right)$. Note that the true MTFs are four-fold symmetric, while the truncated $sinc^2$ and $sinc^3$ approximations are circularly symmetric.

Signal-to-Noise Ratio

As in GRD, we assume that the k-space noise term is a zero-mean uncorrelated complex additive Gaussian stochastic variable with standard deviation σ. Pipe's variance analysis [11] for GRD reconstruction, as given in Eq.(3.5), is equally valid for the CBP reconstruction. Thus, the variance per unit k-space coverage is still

$$\text{var} = \frac{\sigma^2}{T_{acq}\,\text{Area}_k^2} \int_{\mathbf{k}} |W(\mathbf{k})|^2 \, d\mathbf{k} \tag{3.15}$$

where $W(\mathbf{k})$ is the *effective* weighting function in k-space, namely the CBP filter function $\mathcal{A}(k_r)|k_r|$ times the appropriate MTF.

In the previous section, we showed that the convolution function, backprojection, and resampling operations lead to a non-uniform MTF in k-space. Consequently, the effective weighting function must incorporate these effects. This is done by multi-

plying the (perhaps apodized) ramp function with the calculated CBP MTF. Consequently, the CBP variance per unit k-space coverage is given by

$$\frac{\sigma^2 \sum_{n=0}^{N_a-1} \sum_{m=-N_r/2}^{N_r/2-1} [\mathcal{A}(m\,\Delta k_r)|m\,\Delta k_r|\ \mathrm{MTF}(m\Delta k_r, n\Delta k_\theta)\ \Delta k_r \Delta k_\theta]^2}{T_{acq}\left[\pi(N_r \Delta k_r/2)^2\right]^2} \tag{3.16}$$

More particularly, var_{cbp} using the Ram-Lak (rala) filter requires $\mathcal{A}(m\,\Delta k_r) = 1$ and the Ram-Lak MTF (shown in Figure 3.2), so that

$$\begin{aligned} \mathrm{var}_{rala} &= \frac{\sigma^2 \sum_{n=0}^{N_a-1} \sum_{m=-N_r/2}^{N_r/2-1} [|m\,\Delta k_r|\ \mathrm{MTF}_{rala}(m\Delta k_r, n\Delta k_\theta)\ \Delta k_r \Delta k_\theta]^2}{T_{acq}\left[\pi(N_r \Delta k_r/2)^2\right]^2} \\ &\simeq 0.711 \frac{\sigma^2}{T_{acq} N_r N_a} \end{aligned} \tag{3.17}$$

Since the CBP MTF is difficult to ascertain analytically, we resorted to a numerical evaluation of the variance per unit k-space coverage. Therefore, the 0.711 factor comes about from a numerical integration of the square of the finite, circular, ramp filter multiplied by the Ram-Lak MTF divided by the circular k-space area squared.

Using Eqs.(3.9),(3.17), and $\mathrm{SNR} \equiv \frac{\Delta v}{\sqrt{\mathrm{var}}}$, the CBP_{rala} SNR relative to GRD of polar data using the ramp filter is easily compared, and is given in Table 3.1. The Shepp-Logan results are also included for further comparison. The CBP algorithm implemented with the Ram-Lak filter yields an increased SNR relative to GRD of polar k-data using the ramp filter. However, with GRD the MTF is flat while with CBP the MTF falls off at higher frequencies, resulting in a loss of resolution. This point will be expounded upon in the Tradeoffs section.

Aliasing

The aliasing using the CBP algorithm of Eq.(3.13) is markedly different than that of GRD. Because the radial k_r–lines are discretized rectilinearly with spacing Δk_r, the Nyquist criterion applies in the radial direction: if the object is spatially-limited to within a diameter of $\frac{1}{\Delta k_r}$, then the IFT of each radial k_r–line is a non-aliased

Table 3.1: Theoretical variance and SNR values for GRD and CBP

	Polar Sampling GRD Recon	Polar Sampling CBP_{rala} Recon	Polar Sampling CBP_{shlo} Recon
var	$\frac{4}{3}\ \frac{\sigma^2}{T_{acq}.N_r.N_a}$	$0.71\ \frac{\sigma^2}{T_{acq}.N_r.N_a}$	$0.45\ \frac{\sigma^2}{T_{acq}.N_r.N_a}$
$\frac{\text{var}}{\text{var}_{grd}}$	1	0.53	0.34
SNR	$\frac{\sqrt{3}}{2}\ \frac{\Delta v\sqrt{T_{acq}.N_r.N_a}}{\sigma}$	$1.19\ \frac{\Delta v\sqrt{T_{acq}.N_r.N_a}}{\sigma}$	$1.50\ \frac{\Delta v\sqrt{T_{acq}.N_r.N_a}}{\sigma}$
$\frac{\text{SNR}}{\text{SNR}_{grd}}$	1	1.37	1.725

Theoretically expected absolute and relative variance (var) and SNR values for $[N_r \times N_a]$ polar samples reconstructed using either GRD with the ramp filter, CBP with the Ram-Lak (rala) filter, or CBP with the Shepp-Logan (shlo) filter. Under these conditions, the effective resolution will be maximum for GRD (since its MTF is uniform) while that of CBP is reduced (since the MTFs roll off at higher frequencies, as depicted in Figures 3.2(a) and 3.2(c) for the rala and shlo filters, respectively).

projection through the object. Thus, unlike GRD, in CBP the original sampling effects in the k_r direction are treated in 1D as opposed to 2D.

The azimuthal sampling criterion, though, remains the same between the two algorithms: if the k-space values are azimuthally undersampled, the reconstructed image will contain streak artifacts. If, however, $N_a \geq \frac{1}{2}\pi.N_r$, then the image will not suffer from this streaking artifact.

The effective PSF of CBP is similar to that of GRD, except that the PSF is composed of the main lobe *only* and *no* ringlobes. If there are an infinite number of projections, then the CBP PSF is calculated from the spin integration of $C_{cbp}(r)$ found in Eq.(3.14). However, one must note that $C_{cbp}(r)$ is the IFT of the *continuous* (perhaps apodized) ramp filter followed by discretization in the image domain: by comparison, the GRD weighting function is discretized directly in k-space, from which the GRD PSF is the spin integration of the IFT of the discretized $W(\mathbf{k})$. This

difference is what leads to the ringlobes in GRD, but not in CBP. For example, $C_{cbp}(r)$ using the Ram-Lak filter is, from Appendix B,

$$C_{cbp}(r) \propto \left[2\,\mathrm{sinc}(r N_r \Delta k_r) - \mathrm{sinc}^2\left(r\frac{N_r}{2}\Delta k_r\right)\right] \times \frac{1}{\Delta r}\amalg\left(\frac{r}{\Delta r}\right) \qquad (3.18)$$

with $\Delta r = \dfrac{1}{N_r \Delta k_r}$ as before. Neglecting the sampling process, *i.e.* the $\amalg(r/\Delta r)$ term, C_{cbp} above is identical to $c(r)$ of Eq.(3.10) for $j=0$. Upon spin integration, the CBP PSF is given by $\mathcal{Q}\left\{c_0(r)\right\} = s_0(r)$. Thus, as stated previously, the PSF consists of the main lobe only and no ringlobes. In effect, the ringlobes in GRD emanate from the sampling (in k-space) of the weighting function *prior* to the IFT and subsequent spin integration. Conversely, CBP eliminates the ringlobes by sampling (in the image domain) the IFT of the weighting function *after* the IFT.

In reality, the discretization of $C_{cbp}(r)$ means that the true CBP PSF is different than $s_0(r)$, the GRD main lobe. While $s_0(r)$ is calculated from the spin integration of $c_0(r)$, in CBP one spin integrates $C_{cbp}(r)$ which is a sampled and subsequently interpolated version of $c_0(r)$. The functions c_0 and C_{cbp} are depicted on the left sides of Figures 3.5(a) and 3.5(e), respectively, which are found on page 91.

The CBP sampling criterion is simply stated: provided that (1) the k_r spacing Δk_r is such that the object is contained within a circle of diameter $\dfrac{1}{\Delta k_r}$, and (2) the number of projections N_a within the azimuthal range 0–π is of the order $\frac{1}{2}\pi N_r$ or greater, then the aliasing resulting from the CBP reconstruction will be negligible.

3.3 Tradeoffs

Although GRD is a general reconstruction algorithm and CBP applies mostly to polar sampling, their respective tradeoffs concerning resolution, SNR, and aliasing can be directly compared for purely polar k-space acquisitions.

The effective resolution of each algorithm is dependent on its modulation transfer function. The MTF of GRD for polar k-data using the ramp filter is unity for radial frequencies $|k_r| \leq \frac{1}{2} N_r \Delta k_r$. Conversely, the MTF of CBP using the Ram-Lak filter is not unity, nor is it circularly symmetric. Rather, it is an even four-fold symmetric function which can be approximated by $\mathrm{sinc}^2\left(\frac{k_r}{N_r \Delta k_r}\right)$ at low spatial frequencies, as explained in the CBP-MTF section.

For GRD reconstruction using the ramp weighting, the MTF is flat. Conversely, for CBP reconstruction using the Ram-Lak filter, the MTF decreases at higher spatial frequencies. Thus, the effective image resolution of CBP (rala) images is degraded with respect to that of GRD. However, this decrease in resolution is compensated by an increase in SNR, as shown in Table 3.1.

The weighting functions need not be limited to the ramp (Ram-Lak) functions. Many choices of apodized ramp functions are possible, both for GRD and CBP. The ramp filter guarantees the maximum resolution (for a given algorithm) in the reconstructed image. However, with the ramp filter the variance is also maximized which leads to a minimal SNR. For apodized ramp functions, the MTF rolls off at higher k_r values. This leads to blurring in the image but with an increase in SNR. Thus, resolution and SNR must be considered in unison to properly compare the GRD and CBP algorithms.

In both GRD and CBP, the variance is given by the effective k-space weighting squared, namely the (possibly apodized) ramp weighting times the MTF of the reconstruction algorithm, *i.e.*

$$\sum_{n=0}^{N_a-1} \sum_{m=-N_r/2}^{N_r/2-1} [\mathcal{A}(m\,\Delta k_r)|m\,\Delta k_r|\ \mathrm{MTF}(m\Delta k_r, n\Delta k_\theta)\,\Delta k_r \Delta k_\theta]^2 \qquad (3.19)$$

For both GRD and CBP, $\mathcal{A}(m\,\Delta k_r)$ is unity when using the ramp and/or Ram-Lak filters. However, their respective MTFs are different, which leads to a different variance and SNR. However, the change in SNR is directly compensated for by a change in resolution owing to their different MTFs, as discussed earlier.

One can, in principle, restore maximum resolution by deconvolving the PSF from the reconstructed CBP image, but doing so decreases the SNR to a level similar to that of GRD images. Also, it is possible to use an apodized ramp weighting in GRD so that the image SNR is comparable to the CBP_{ramp} SNR. In other words, the GRD MTF would no longer be uniform but would roll off at higher frequencies. In this case, the GRD and CBP image resolution and SNR will be comparable.

In effect, if one reconstructs the **k**-data to obtain a comparable SNR between the GRD and CBP images, then the effective image resolution or blurring will also be comparable. The reverse is also true. Thus, the GRD and CBP algorithms behave similarly when one considers resolution and SNR together: GRD with the ramp filter maximizes resolution with minimal SNR, whereas CBP sacrifices resolution with a gain in SNR. Still, one can judiciously alter the weighting parameters to get comparable results between the two algorithms. However, the aliasing properties will not be significantly altered since altering the weighting does not eliminate the ringlobes in GRD although it may suppress them slightly.

Although SNR and resolution must be considered together, one can simultaneously maximize both provided the azimuthal spacing varies as a function of k_r such that the GRD weighting $W(\mathbf{k})$ is constant. Gridding of these data yields maximum resolution (because of the unit MTF) and maximum SNR [19, 20], since the variance is minimized to $\dfrac{\sigma^2}{T_{acq}\,N_p}$, where N_p is the total number of sampled points. Since we require that $N_a \simeq \frac{1}{2}\pi N_r$ only at $k_r^{max} = \frac{1}{2}N_r\Delta k_r$, then $N_p < N_r N_a$. Thus, the GRD reconstruction time will be shorter than for the purely polar case of $[N_r \times N_a]$ sample points. Note, however, that the aliasing characteristics will be identical in both cases because PSF_{grd} of Eq.(3.11) is still applicable since there is no azimuthal aliasing.

The aliasing incurred using CBP with the Ram-Lak filter and linear interpolation, and GRD with the ramp filter are different. For an infinite number of projections ($N_a \rightarrow \infty$), the point spread function is given by the spin integration of the appropriate function, namely Eq.(3.10) for GRD and Eq.(3.18) for CBP_{ramp}. In actuality, N_a is finite and so the respective PSFs are given by a discrete and finite spin *summation* instead of spin integration. This leads to potential azimuthal (streaking) artifacts in the baseband unless $N_a \geq \frac{1}{2}\pi N_r$.

For GRD reconstruction, the ramp filter is discretized *prior* to the IFT, while for CBP it is discretized *after* the IFT. Because the ringlobes emanate from the discretization of the filter prior to the IFT, the CBP PSF is composed of the main lobe only. Thus, provided the object being reconstructed is contained within a circular FOV of diameter $\frac{1}{\Delta k_r}$ and $N_a \geq \frac{1}{2}\pi N_r$, the aliasing resulting from the CBP reconstruction will be negligible.

In comparison, the ringlobes present in the GRD PSF are due to the fact that the GRD reconstruction retains the original 2D sampling effects. One way to minimize the effects of the ringlobes is to sinc-interpolate in the radial direction before GRD reconstruction, as suggested in section 3.2.1.

It is interesting to note that if one applies the ramp (Ram-Lak) filter directly to the polar k-data prior to the 1D IFT (*i.e.* in a multiplicative fashion in analogy to what occurs in GRD), takes the IFT in the k_r direction and backprojects, then the reconstructed image aliasing is similar to that of the GRD image. This is because the IFT of the discrete ramp produces replicates which upon backprojection (the discrete analog of spin integration) leads to ringlobes. Thus, the discrete convolution in image space is preferable to the discrete multiplication in k-space.

3.4 Results

The theoretical SNR expectations were verified experimentally on a 0.5T GE Signa scanner (General Electric Medical Systems, Milwaukee, WI), whose maximum gradient amplitude and slew rate are 1.0 Gauss/cm and 1.67 Gauss/cm/ms, respectively. The phantom consisted of 9 NMR glass tubes (1.0 cm diameter, 15 cm length) closely packed within a 4x4 cm^2 region. Each tube was filled with various concentrations of agarose doped with nickel chloride ($NiCl_2$) to generate phantoms with T_1 and T_2 values ranging from 250ms-1250ms and 25ms-400ms, respectively, as shown in Table 3.2.

Table 3.2: Agarose/$NiCl_2$ phantom T_1 and T_2 values

Tube #	$NiCl_2$	Agarose	T_2	T_1
1	5.0 mM	4.0 %	24.9 ms	249.8 ms
2	5.0 mM	1.0 %	79.4 ms	268.2 ms
3	5.0 mM	0.2 %	178.7 ms	270.1 ms
4	2.0 mM	4.0 %	27.3 ms	508.4 ms
5	2.0 mM	1.0 %	95.5 ms	573.5 ms
6	2.0 mM	0.2 %	284.0 ms	567.1 ms
7	0.5 mM	4.0 %	27.9 ms	1066.0 ms
8	0.5 mM	1.0 %	107.3 ms	1230.0 ms
9	0.5 mM	0.2 %	407.7 ms	1240.0 ms

Measured T_1 and T_2 relaxation times for the nickel/agarose ($NiCl_2$) phantoms of varying concentrations.

A Concentric Circle Spin Echo pulse sequence was written (EPIC 5.6 pulse programming language) such that half the circle was acquired at each excitation. The readout was in the azimuthal direction, and the radial steps were increased for subsequent excitations to acquire the entirety of k-space, *i.e.* both the top and bottom half. The k-space values were acquired using the GE head coil and a loader shell to properly load the coil.

The MR parameters were as follows: an echo time (TE) of 40ms, a repetition time (TR) of 2000ms, a 5mm slice thickness, 1 excitation (NEX) per image, a matrix

size of [384×160] (namely 384 azimuthal points within 0–π with 160 radial points per projection), with a scan time of 5:24 per image. The **k**-space values were measured for FOVs of 11cm, 22cm, and 33cm using filter bandwidths (BW) of ±32kHz, ±16kHz, and ±8kHz, which correspond to acquisition times (T_{acq}) of 6144μs, 12288μs, and 24576μs, respectively. All images were reconstructed onto a 256x256 image grid for both GRD and CBP.

Two images were acquired for each FOV/BW combination, say img_1 and img_2. The resultant signal and noise images were calculated from $\frac{1}{2}\left[\text{img}_1+\text{img}_2\right]$ and $\frac{1}{\sqrt{2}}\left[\text{img}_1-\text{img}_2\right]$, respectively. The pair of images were then scaled such that the signal image was normalized to have a maximum amplitude of one. We measured the average signal and noise within various regions of interest (ROI) of the phantoms, and determined the SNR by taking their ratio. Thirty six ROIs were chosen within the NMR tubes, and 36 ROIs were chosen in the surrounding air medium (*i.e.* noise regions).

All noise images (GRD and CBP) were observed to be fairly uniform over the entire FOV. Furthermore, the signal images were observed to possess comparable signal intensities (to within ±5%) at the various FOVs and BWs.

From Eq.(3.9) and Table 3.1, the SNRs of both GRD and CBP are expected to scale as the square-root of the acquisition time. And, since $T_{acq} \propto 1/\text{BW}$, the SNRs at ±16kHz and ±8kHz relative to that at ±32kHz are expected to increase by $\sqrt{2} \approx 1.41$ and $\sqrt{4} = 2$, respectively. The experimental results of Table 3.3 support the theoretical expectations.

We also verified the noise dependence with voxel volume. Since the reconstructed images consist of N_r square pixels of width Δr, the FOV along the x and y directions is given by $\text{FOV} = N_r \Delta r$. Consequently, the voxel volume is $\Delta v = \text{FOV}^2 \Delta z / N_r^2$. All images were acquired for Δz and N_r held constant, so that Δv scales as FOV^2.

The mean noise value was measured in 36 air regions at different FOVs for various BWs for both GRD and CBP reconstruction. Since the SNR is expected to scale as

Table 3.3: Experimental SNR measurements relative to a ±32kHz filter

	±32kHz (6144μs)	±16kHz (12288μs)	±8kHz (24576μs)
GRD (11cm)	1.000	1.38 ± 0.07	1.95 ± 0.12
CBP_{rala} (11cm)	1.000	1.39 ± 0.06	2.00 ± 0.13
CBP_{shlo} (11cm)	1.000	1.39 ± 0.08	2.01 ± 0.13
GRD (22cm)	1.000	1.33 ± 0.08	1.97 ± 0.16
CBP_{rala} (22cm)	1.000	1.33 ± 0.12	1.93 ± 0.22
CBP_{shlo} (22cm)	1.000	1.30 ± 0.11	1.89 ± 0.20
GRD (33cm)	1.000	1.49 ± 0.19	1.93 ± 0.36
CBP_{rala} (33cm)	1.000	1.39 ± 0.19	1.85 ± 0.34
CBP_{shlo} (33cm)	1.000	1.41 ± 0.23	1.85 ± 0.35

Experimental SNR measurements relative to a ±32kHz bandwidth filter (with the corresponding acquisition times in brackets). The measurements represent the mean plus one standard deviation of measured relative SNRs in 36 different ROIs within the various $NiCl_2$ phantoms. The theoretical expectations at ±16kHz and ±8kHz are 1.41 and 2.0, respectively.

FOV^{-2} and the maximum signal within all images was normalized to unity, then the variation of noise only is expected to scale as $1/FOV^2$. Thus, relative to an 11cm FOV, the expected noise at 22cm and 33cm FOVs is expected to be $1/2^2 = 0.25$ and $1/3^2 \approx 0.11$, respectively. The experimental results of Table 3.4 support the expectations, although there seems to be a bias to slightly overestimate the noise.

Finally, we verified the theoretically expected SNR increases of CBP images relative to GRD images, as given in Table 3.1. We expected an SNR increase of approximately 1.37 using the Ram-Lak filter, and an increase of about 1.725 using the Shepp-Logan filter. The results of Table 3.5 agree with theoretical predictions.

Although the GRD and CBP Signal-to-Noise Ratio theory sections were developed assuming ideal conditions, the results of Tables 3.3–3.5 provide experimental validation of the simplified theoretical analysis.

Table 3.4: Experimental noise measurements relative to an 11cm FOV

	11cm FOV	22cm FOV	33cm FOV
GRD (±32kHz)	1.000	0.28 ± 0.01	0.13 ± 0.01
CBP_{rala} (±32kHz)	1.000	0.27 ± 0.01	0.12 ± 0.01
CBP_{shlo} (±32kHz)	1.000	0.27 ± 0.01	0.12 ± 0.01
GRD (±16kHz)	1.000	0.28 ± 0.01	0.13 ± 0.01
CBP_{rala} (±16kHz)	1.000	0.27 ± 0.01	0.12 ± 0.01
CBP_{shlo} (±16kHz)	1.000	0.27 ± 0.01	0.12 ± 0.01
GRD (±8kHz)	1.000	0.27 ± 0.01	0.12 ± 0.01
CBP_{rala} (±8kHz)	1.000	0.27 ± 0.01	0.11 ± 0.01
CBP_{shlo} (±8kHz)	1.000	0.26 ± 0.01	0.12 ± 0.01

Experimental noise measurements relative to an 11cm FOV. The measurements represent the mean plus one standard deviation of measured noise regions in 36 different ROIs within the air regions surrounding the $NiCl_2$ phantoms. The theoretical expectations at 22cm and 33cm FOVs are 0.25 and 0.11, respectively.

Table 3.5: Experimental SNR measurements of CBP relative to GRD

	GRD	CBP_{rala}	CBP_{shlo}
11cm FOV, ±32kHz	1.000	1.38 ± 0.06	1.68 ± 0.10
22cm FOV, ±32kHz	1.000	1.37 ± 0.05	1.72 ± 0.09
33cm FOV, ±32kHz	1.000	1.35 ± 0.06	1.65 ± 0.09
11cm FOV, ±16kHz	1.000	1.39 ± 0.05	1.70 ± 0.07
11cm FOV, ±8kHz	1.000	1.41 ± 0.04	1.72 ± 0.06

Experimental SNR measurements of CBP_{rala} and CBP_{shlo} reconstruction relative to GRD reconstruction. The measurements represent the mean plus one standard deviation of measured relative SNRs in 36 different ROIs within the various $NiCl_2$ phantoms. The theoretical expectations for CBP_{rala} and CBP_{shlo} are 1.37 and 1.725, respectively.

3.5 Non-Equidistant k_r Sampling

The SNR, resolution, and aliasing characteristics are important design (and reconstruction algorithm) considerations for any MR acquisition. However, the scan time and the resulting flow/motion artifacts in the image are just as important. Since the gross features of the imaged object are contained near the centre of k-space while its edge information is located at the high spatial frequencies, it may be desirable to sample non-uniformly in the radial and/or azimuthal directions to reduce scan time and suppress motion artifacts. Here, we restrict ourselves to non-equidistant radial polar sampling with equally-spaced azimuthal samples.

To reconstruct such radially non-equidistant polar k-data, GRD can still be used because of its flexibility and generality, provided that the 2D weighting function $W(\mathbf{k})$ is known. CBP, however, expects the projection data (*i.e.* the 1D IFT of the k_r-lines) to be equally-spaced. Consequently, one can perform a 1D GRD of the k_r-lines (which gives rectilinear MR projections) followed by CBP: this we call the hybrid GRD/CBP reconstruction.

To perform the GRD/CBP reconstruction, one first needs to determine the 1D weighting function $W(k_r)$ required in the 1D GRD of the non-equidistant k_r samples. This is easily calculated. For example, assume 3 consecutive k_r samples are located at $k_{r,p-1}$, $k_{r,p}$, and $k_{r,p+1}$. The weighting of the p^{th} sample, a measure of its areal extent, is given by

$$W(k_{r,p}) = \frac{1}{2}|k_{r,p} - k_{r,p-1}| + \frac{1}{2}|k_{r,p+1} - k_{r,p}| \tag{3.20}$$

Although GRD/CBP reconstruction is generally more time-consuming than 2D GRD, it does offer some benefits: $W(k_r)$ is easily calculated (as shown above), and the aliasing is reduced.

The aliasing reduction of GRD/CBP compared to 2D GRD is obvious when one compares their PSFs which are given by the spin integration of the effective weighting functions. For general non-uniform radial polar sampling, the (k_x, k_y) coordinates are

transformed to $(K(k_r), k_\theta)$, where $K(k_r)$ represents some general function. For 2D GRD, the weighting is

$$W(\mathbf{k}) = \left| \begin{array}{cc} \frac{\partial k_x}{\partial k_r} & \frac{\partial k_x}{\partial dk_\theta} \\ \frac{\partial k_y}{\partial dk_r} & \frac{\partial k_y}{\partial dk_\theta} \end{array} \right|_{k_r = m\Delta k_r} \Rightarrow \left| K(m\Delta k_r) \frac{dK(m\Delta k_r)}{dk_r} \right| \tag{3.21}$$

so that the PSF, using the Fourier convolution theorem, is given by

$$\begin{aligned} \mathrm{PSF}_{grd} &= \mathcal{Q}\left\{ \mathcal{F}^{-1}\left[\left| K(m\Delta k_r) \frac{dK(m\Delta k_r)}{dk_r} \right| \right] \right\} \\ &= \mathcal{Q}\left\{ \mathcal{F}^{-1}\left[\left| \frac{dK(m\Delta k_r)}{dk_r} \right| \right] \star \mathcal{F}^{-1}\left[|K(m\Delta k_r)| \right] \right\} \end{aligned} \tag{3.22}$$

where $\mathcal{Q}$ and $\mathcal{F}^{-1}$ are the spin integration and IFT operators, respectively, and $\star$ is the convolution operator. In analogy to Eq.(3.11), spin integrating the IFT of the discrete weighting will produce ringlobes in the PSF.

In comparison, for the GRD/CBP reconstruction, the 1D gridding portion requires a weighting of $\left| \frac{dK(m\Delta k_r)}{dk_r} \right|$. The ramp-like weighting is applied as a convolution in image space in the CBP portion of the algorithm via $C_{cbp}(r)$. The PSF is thus

$$\mathrm{PSF}_{grd/cbp} = \mathcal{Q}\left\{ \mathcal{F}^{-1}\left[\left| \frac{dK(m\Delta k_r)}{dk_r} \right| \right] \star C_{cbp}(r) \right\} \tag{3.23}$$

where $C_{cbp}(r)$ is given in Eq.(3.14). Note that before convolution, only the baseband is retained. Within this baseband, the aliasing effects of having undersampled at large k_r persist, which is reflected in the $\mathcal{F}^{-1}\left\{ \left| \frac{dK(m\Delta k_r)}{dk_r} \right| \right\}$ term.

Now, comparison of Eqs.(3.22) and (3.23) shows that the only difference in the PSFs is the function convolved with $\mathcal{F}^{-1}\left\{ |dK(m\Delta k_r)/dk_r| \right\}$ prior to spin integration. In GRD/CBP, it is $C_{cbp}(r)$ which is calculated from the IFT of the *continuous* ramp function, which is Eq.(3.18). Conversely, in 2D GRD, it is the IFT of the (non-uniformly) *sampled* ramp function. Thus, in analogy to the purely polar case, the ringlobes emanating from the IFT of the discrete **k**-space ramp weighting have been eliminated, although the original sampling effects (*i.e.* those due to undersampling of the high spatial frequencies) are retained within the baseband.

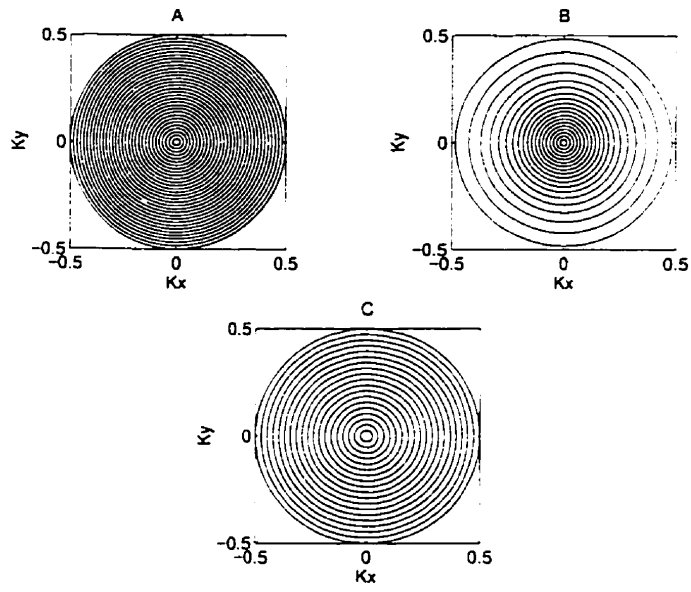

Figure 3.3: Polar k-space sampling trajectories

K-*space sampling patterns for (a) purely polar samples with radial spacing* Δk_r. *(b) radially non-equidistant polar samples whose radial positions are given in Eq.(3.24), and (c) purely polar samples with radial spacing* $1.52\Delta k_r$. *Note that all trajectories cover the same effective area in* **k**-*space. The axes are in units of* $N_r\Delta k_r$.

A simulation of radially non-equidistant polar **k**-data was carried out. The data were reconstructed using both 2D GRD and the GRD/CBP algorithms (Figure 3.4). The reference image in Figure 3.4(a) depicts the synthetic noise-free phantom **k**-data reconstructed from $[128 \times 128]$ Cartesian samples of spacing Δk_r in both the k_x and k_y directions. Figures 3.4(b) and 3.4(c) show the 2D GRD and GRD/CBP reconstructions, respectively, of the same synthetic phantom sampled with radially non-equidistant polar sampling. The **k**-data consisted of 200 azimuthally equidistant samples within $(0, \pi)$ by M radial samples located at $K(k_r)$ given by

$$\pm \sum_{m=0}^{M/2} \left(\frac{k_r}{\Delta k_r} + c_5 \left[\frac{k_r}{N_r \Delta k_r} \right]^5 + c_{10} \left[\frac{k_r}{N_r \Delta k_r} \right]^{10} \right) \delta(k_r - m\Delta k_r) \qquad (3.24)$$

where c_5 and c_{10} are constants, and $M < N_r$. By setting $c_5 = 5000.$ and $c_{10} = 80000.$ we get $M = 84$ so that the total k_r extent is $128\Delta k_r$. This represents a 34% reduction of k_r samples. For comparison, Figure 3.4(d) depicts the case of 84 radially equidistant polar samples covering the same k_r extent of $128\Delta k_r$ but with spacing $1.52\Delta k_r$.

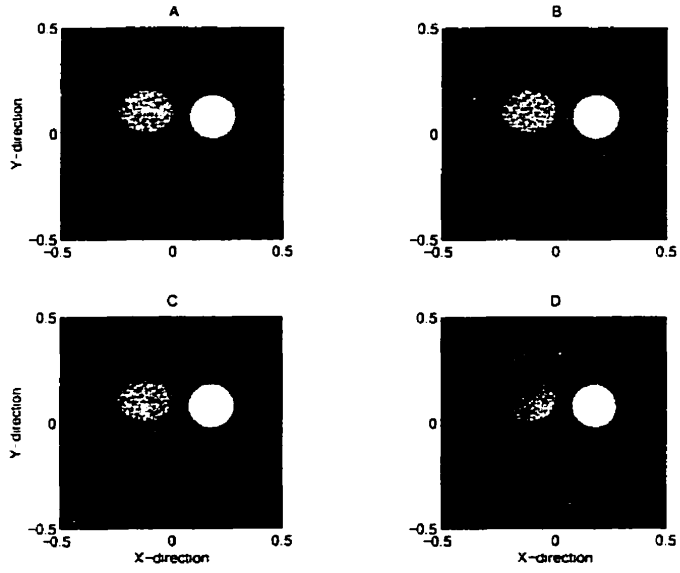

Figure 3.4: Synthetic, noise-free, phantom images

Synthetic, noise-free, phantom images. (a) Reference $[128\times128]$ *Cartesian image reconstructed with the FFT. (b) Radially non-equidistant* $[84\times200]$ *polar* **k***-data reconstructed with the 2D GRD algorithm. The radial spacing is about* Δk_r *at low frequencies but increases to over* $3\Delta k_r$ *at high frequencies. (c) The same* **k***-data as in Figure 3.4(b), but reconstructed with the hybrid GRD/CBP algorithm. (d) Radially equidistant* $[84\times200]$ *polar* **k***-data of radial spacing* $1.52\Delta k_r$ *reconstructed with the 2D GRD algorithm. The details of the* **k***-data sample locations can be found in the text. All images were reconstructed onto a* $[128\times128]$ *image grid. Note the severe aliasing in Figure 3.4(d) as compared to Figure 3.4(b) or Figure 3.4(c), even though the matrix size and* **k***-space extent are the same.*

Note that because the radial extent of **k**-space is constant (see Figure 3.3), all reconstructed images have the same pixel size. The aliasing effects, however, are different, especially when comparing the equidistant versus non-equidistant cases. Furthermore, the SNR and *effective* resolution differ, although these two effects must be considered jointly (as discussed in the Tradeoffs section).

In Figure 3.4(c), the circular oscillations present inside and outside the object are strictly due to undersampling at large k_r. They emanate mostly from the object boundary (outer ellipse) since the aliasing effect is more pronounced for large objects within the FOV. In Figure 3.4(b), the oscillations are slightly larger, especially in the region outside the object. This is the ringlobe effect arising from the

$\mathcal{F}^{-1}\left[|K(m\Delta k_r)|\right]$ term in Eq.(3.22). Moreover, the signal amplitude effect seen in Figure 3.1 persists in Figure 3.4(b) but is eliminated in Figure 3.4(c) since this too is a ringlobe effect. It emanates from the **k**-space discretization of the ramp-like filter *prior* to IFT and subsequent spin integration.

Figure 3.4(d) clearly demonstrates that if the **k**-space coverage and number of samples is the same as in the radially non-equidistant case, the aliasing is severe, although the underlying gross characteristics of the object are still recognizable.

Neither the GRD nor GRD/CBP reconstructions correct for aliasing present due to undersampling of the data. Thus, some aliasing is inevitable under those sampling circumstances. However, not all aliasing is catastrophic. In fact, it may be possible to sample in such a way that the aliasing within the image is tolerable and does not affect the overall SNR and/or CNR (contrast-to-noise ratio) characteristics of the image too severely. These concepts may be applicable when the object undergoes motion, whereby an increase in spatial sampling artifacts (*i.e.* aliasing) is traded off for a decrease in temporal artifacts (*i.e.* a reduction in motion artifacts).

3.6 Discussion

The image reconstruction effects of equidistant radial/azimuthal polar k-data were investigated for both the gridding and the convolution backprojection algorithms. These effects included the SNR, resolution, and aliasing present in the image.

While GRD is primarily a Fourier domain algorithm and CBP is an image domain technique, both of these algorithms perform identically in terms of SNR and resolution, provided that these two effects are considered together. In their most basic implementations, *i.e.* the weighting based on ramp filters, GRD maximizes resolution at the expense of SNR, while CBP sacrifices resolution to increase the SNR.

The variance analysis presented herein yields the SNR value, an effectively global figure of merit. However, a more in-depth analysis of the noise power spectrum is warranted to ascertain and determine the complete characteristics of noise propagation within each algorithm.

Gridding offers the advantage of direct manipulation of the k-space data. This allows one to tailor the resolution versus the SNR. Moreover, GRD allows for the possibility of non-equidistant azimuthal polar sampling whereby one can maximize resolution and SNR simultaneously.

In this chapter, we contrasted GRD using the ramp filter with CBP using the Ram-Lak (ramp) filter, the most direct comparison between the two algorithms. However, many choices of reconstruction weighting and/or convolution functions are possible for both GRD and CBP. In fact, the polar k-data can be reconstructed using CBP and GRD such that the images have comparable SNR and resolution. In this case, either the GRD weighting function or the CBP convolution function or both must be altered to yield comparable variances and MTFs. Apodized ramp filters also have the added benefit of suppressing Gibb's ringing artifacts, but doing so leads to increased blurring and a loss of image resolution.

One important difference between GRD and CBP is their different PSFs which lead to different aliasing behaviour. The polar PSF using GRD includes the main

lobe and the ringlobes. The main lobe describes the blurring effect of finite sampling, and the ringlobes are a measure of the expected aliasing. Conversely, the PSF using CBP eliminates the ringlobes altogether. Thus, provided the radial sampling satisfies the Nyquist criterion, the aliasing using CBP will be minimal. In both algorithms, though, insufficient azimuthal sampling leads to streaking artifacts in the image (azimuthal aliasing). Neither GRD nor CBP correct for this artifact.

Interestingly enough, simulations show that if the **k**-data are radially continuous as opposed to discrete (*i.e.* spiral versus concentric circles), the PSF ringlobes are reduced, which leads to reduced aliasing. However, the spiral PSF is dependent on the number of interleaves acquired, and consequently so is the aliasing. In short, one must fully characterize the PSF of the particular sampling scheme to ascertain the aliasing effects. Therefore, the conclusions drawn here for purely polar sampling do not necessarily apply to spiral sampling.

To reconstruct radially non-equidistant but azimuthally equidistant **k**-data, we suggested a hybrid GRD/CBP reconstruction algorithm. This technique reduces aliasing in comparison to 2D GRD, although the reconstruction times tend to be longer by about 30% or so. Though an in-depth analysis of the radial sampling effects of radially non-equidistant polar **k**-data is beyond the scope of this treatise, the hybrid GRD/CBP algorithm may allow one to investigate the tolerable aliasing limits and ensuing tradeoffs of radially non-equidistant polar **k**-space sampling.

3.7 Appendices

3.7.1 App. A – CBP Integral

In polar coordinates, we write $k_x = k_r \cos k_\theta$ and $k_y = k_r \sin k_\theta$, from which the 2D IFT of $M(k_r, k_\theta)$ is

$$\begin{aligned} I(x,y) &= \int_{k_\theta=0}^{2\pi} \int_{k_r=0}^{\infty} M(k_r, k_\theta)\, \epsilon^{2\pi i k_r [x\cos k_\theta + y \sin k_\theta]}\, k_r dk_r dk_\theta \\ &= \int_0^{\pi} \int_0^{\infty} M(k_r, k_\theta)\, \epsilon^{2\pi i k_r X}\, k_r dk_r dk_\theta \; + \\ &\qquad \int_{\pi}^{2\pi} \int_0^{\infty} M(k_r, k_\theta)\, \epsilon^{2\pi i k_r X}\, k_r dk_r dk_\theta \end{aligned} \tag{3.25}$$

where $X \equiv [x \cos k_\theta + y \sin k_\theta]$. In the second integral, we can first substitute $k_\beta = k_\theta - \pi$, then note that $M(k_r, k_\beta + \pi) = M(-k_r, k_\beta)$, and then substitute $k_s = -k_r$ to obtain

$$\begin{aligned} \int_{k_\theta=\pi}^{2\pi} \int_{k_r=0}^{\infty} M(k_r, k_\theta)\, \epsilon^{2\pi i k_r X}\, k_r dk_r dk_\theta \;\; &= \\ \int_0^{\pi} \int_{-\infty}^{0} M(k_s, k_\beta)\, \epsilon^{2\pi i k_s X}\, |k_s|\, dk_s dk_\beta & \end{aligned} \tag{3.26}$$

so that

$$I(x,y) = \int_0^{\pi} \int_{-\infty}^{\infty} M(k_r, k_\theta)\, \epsilon^{2\pi i k_r X}\, |k_r|\, dk_r dk_\theta \tag{3.27}$$

Now, for a particular $k_\theta = k'_\theta$, the $X(x,y)$ variable represents the projection of (x,y)-space at the same angle k'_θ in the image domain. Conversely, we can write this 2D $X(x,y)$ representation as a 1D representation of r in conjunction with backprojection:

$$\begin{aligned} \int_{-\infty}^{\infty} M(k_r, k'_\theta)\, \epsilon^{2\pi i k_r X(x,y)}\, |k_r|\, dk_r \;\; &\rightarrow \;\; B\left\{ \int_{-\infty}^{\infty} M(k_r, k'_\theta)\, \epsilon^{2\pi i k_r r}\, |k_r|\, dk_r \right\} \\ = \;\; B\left\{ \mathcal{F}^{-1}\left[M_{k'_\theta}(k_r)\, |k_r| \right] \right\} \;\; &= \;\; B\left\{ \mathcal{F}^{-1}\left[M_{k'_\theta}(k_r) \right] \star \mathcal{F}^{-1}\left[|k_r| \right] \right\} \end{aligned} \tag{3.28}$$

where B denotes backprojection, and $M_{k'_\theta}(k_r) \equiv M(k_r, k'_\theta)$ represents the radial k-line at angle k'_θ. Note that Eq.(3.28) applies to continuous functions, whereby the ramp weighting can be applied as a multiplication in k-space or as a convolution in image space (by virtue of the Fourier convolution theorem [9, p.108]). When applied to discrete functions, however, the convolution expression is preferred since it does

not suffer from cyclical aliasing [21. Ch.7]. Finally, then

$$I(x,y) \;=\; \int_0^{\pi} B\left\{\mathcal{F}^{-1}\left[M_{k_\theta}(k_r)\right] \star \mathcal{F}^{-1}\left[|k_r|\right]\right\} dk_\theta \tag{3.29}$$

The interpretation of Eq.(3.29) follows readily. The IFT of each radial k_r-line at angle k_θ is convolved with the IFT of the ramp filter which compensates for the variable sampling density. This convolved projection at angle k_θ is then backprojected for each desired image (x,y) location. The reconstructed image $I(x,y)$ is the summation of all the convolved projections at angles k_θ within $(0,\pi)$. Note that we imposed no conditions on $M(k_r,k_\theta)$ so that this reconstruction formalism is valid for Hermitian, anti-Hermitian, or non-Hermitian polar k-data.

3.7.2 App. B – CBP MTF

One might expect the convolution backprojection MTF (using linear interpolation) to be given by $\mathcal{A}(k_r)\,\mathrm{sinc}^2\left(\frac{k_r}{N_r\Delta k_r}\right)$ out to a maximum radius of $\frac{1}{2}N_r\Delta k_r$, where $\mathcal{A}(k_r)$ is the apodization function applied to the finite ramp filter. However, the discretization, interpolation, and resampling of the convolved data onto a Cartesian grid leads to a more complicated MTF (see Figure 3.2).

The MTF is given by the Fourier transform of the PSF, where we assume the object to be a point object so that each projection is given by a single impulse at $r=0$, namely $\delta(r)$. The convolved projection is thus the IFT of the filter function. Here, we assume that the filter function is the Ram-Lak filter and that linear interpolation is used in the backprojection stage. The analysis depicted in Figure 3.5 can be applied for other filters and more sophisticated interpolation schemes.

Figure 3.5(a) depicts the ramp filter $F(k_r)$ in the Fourier domain (on the right). Its IFT is

$$f(r) = \int_{-N_r\Delta k_r/2}^{+N_r\Delta k_r/2} |k_r|\,\epsilon^{2\pi i k_r r}\,dk_r \tag{3.30}$$

$$= \frac{(N_r\Delta k_r)^2}{4}\left[2\,\mathrm{sinc}\,(rN_r\Delta k_r) - \mathrm{sinc}^2\left(\frac{rN_r\Delta k_r}{2}\right)\right] \tag{3.31}$$

which is depicted on the left of Figure 3.5(a) (the image domain). For computation purposes, the convolution function is discretized at the Nyquist rate, namely $\Delta r = \frac{1}{N_r\Delta k_r}$. This discretization is expressed by multiplying $f(r)$ with the sampling function $\coprod\left(\frac{r}{\Delta r}\right)$ of Figure 3.5(b) to obtain $f_s(r)$, as shown in Figure 3.5(c). In Fourier space, this corresponds to convolving $F(k_r)$ with $\coprod\left(\frac{k_r}{N_r\Delta k_r}\right)$ to give $\hat{F}(k_r)$, a replicated version of $F(k_r)$, as shown in Figure 3.5(c). The coefficients at locations $p\,\Delta r$ (where p is an integer) of $f_s(r)$ are

$$\text{Ram-Lak filter: } \left\{ \begin{array}{cc} 1/4 & p=0 \\ -1/(p\pi)^2 & p \text{ is ODD} \\ 0 & p \text{ is EVEN} \end{array} \right\} \tag{3.32}$$

The discrete $f_s(r)$ function is then (here assumed linearly) interpolated. Now,

linear interpolation can be expressed as a convolution with a triangle function of width $2\Delta r$, say $\Lambda\left(\frac{r}{\Delta r}\right)$, as depicted in Figure 3.5(d). This gives $f_s(r) * \Lambda\left(\frac{r}{\Delta r}\right)$, which is shown in Figure 3.5(e). Note that this is effectively $C_{cbp}(r)$ of Eq.(3.14). In Fourier space, this corresponds to $\hat{F}(k_r)$ being multiplied (apodized) by $\mathrm{sinc}^2\left(\frac{k_r}{N_r \Delta k_r}\right)$ which is shown in Figures 3.5(e) and 3.5(f), the latter showing an expanded view.

With the interpolated $f_s(r)$ representing one projection at angle k_θ, we then backproject it onto the image grid at the appropriate (x, y) locations. This procedure is depicted in Figure 3.5(g). The 2D FT of this backprojected data results in $\hat{F}(k_r)\,\mathrm{sinc}^2\left(\frac{k_r}{N_r \Delta k_r}\right)$ at the same angle k_θ in (k_x, k_y)-space. However, because of discretization in the x and y directions, we get wraparound (or folding) of the 1D function $\hat{F}(k_r)\,\mathrm{sinc}^2\left(\frac{k_r}{N_r \Delta k_r}\right)$ in the 2D **k**-space, as shown in Figure 3.5(g).

If $k_\theta = 0$, then $\hat{F}(k_r)\,\mathrm{sinc}^2\left(\frac{k_r}{N_r \Delta k_r}\right)$ is folded onto itself and is resampled with spacing Δk_r, which is the original sample spacing, and the foldover points occur at odd multiples of $\pm\frac{1}{2} N_r \Delta k_r$. In this case, we recover the ramp filter exactly, as shown in Figure 3.5(h). Similarly, if $k_\theta = 45°$, then $\hat{F}(k_r)\,\mathrm{sinc}^2\left(\frac{k_r}{N_r \Delta k_r}\right)$ also folds onto itself. However, unlike the $k_\theta = 0$ case, the foldover points occur at odd multiples of $\pm\frac{1}{\sqrt{2}} N_r \Delta k_r$. The effective weighting at 45^0 is not a ramp, but rather an apodized ramp-like function that is non-zero at $k_r = 0$ and extends out to $|k_r| = \frac{1}{\sqrt{2}} N_r \Delta k_r$. This too, is depicted in Figure 3.5(h). For cases where k_θ is not a multiple of 45^0, $\hat{F}(k_r)\,\mathrm{sinc}^2\left(\frac{k_r}{N_r \Delta k_r}\right)$ is distributed over much of the 2D **k**-space, as shown in Figure 3.5(i).

When backprojecting numerous projections within the azimuthal range 0–π, one gets the PSF, whose 2D FT is the MTF (see Figure 3.2). The MTF's non-circular symmetry and the fact that it is not restricted to within a diameter of $N_r \Delta k_r$ is due to the above-mentioned wraparound effect.

Figure 3.5: Comprehensive development of the CBP MTF

Convolution backprojection MTF details in both the image domain and the Fourier domain. (a) The ramp filter $F(k_r)$ and its corresponding IFT $f(r)$ in the image domain. (b) The 1D image domain sampling function of spacing Δr and its FT, a series of impulses with spacing $1/\Delta r = N_r \Delta k_r$. (c) The result of sampling gives $f_s(r)$, whose FT is $\hat{F}(k_r)$, a replicated version of the ramp filter. (d) The triangle function of width $2\Delta r$, and its FT which is proportional to $sinc^2(k_r/[N_r \Delta k_r])$. (e) Linear interpolation of $f_s(r)$, i.e. convolution with the triangle function, and its FT given by $\hat{F}(k_r)$ apodized by the $sinc^2$ function. (f) An expanded view of $\hat{F}(k_r)\, sinc^2(k_r/[N_r \Delta k_r])$ out to $\pm 4 N_r \Delta k_r$. (g) The backprojection of $f_s(r) * \Lambda(r/\Delta r)$ at angle k_θ onto the image grid, and its Fourier counterpart $\hat{F}(k_r)\, sinc^2(k_r/[N_r \Delta k_r])$ which is centred at $(0,0)$, oriented at angle k_θ, and wrapped around due to 2D image domain sampling. (h) At $k_\theta = [0^\circ, 45^\circ]$, $\hat{F}(k_r)\, sinc^2(k_r/[N_r \Delta k_r])$ wraps onto itself giving 1D profiles at $k_\theta = 0^\circ, 45^\circ$, respectively, in 2D Fourier space. (i) The wraparound effect in the Fourier domain for k_θ not a multiple of 45°, shown here for $k_\theta = 22.5^\circ$.

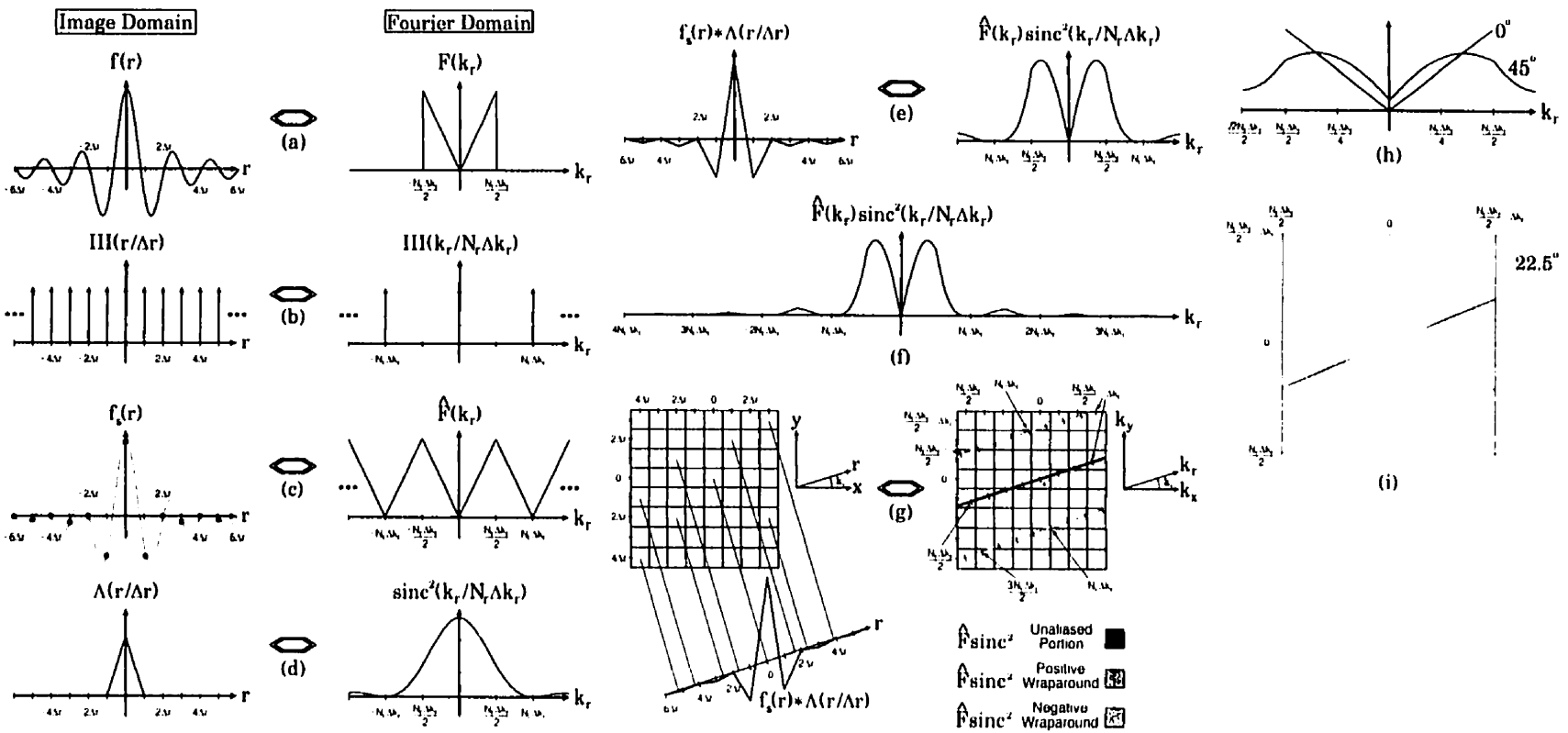
Image Domain
Fourier Domain
f(r)
F(k_r)
(a)
III(r/Δr)
III(k_r/N_rΔk_r)
(b)
f_s(r)
F̂(k_r)
(c)
Λ(r/Δr)
sinc²(k_r/N_rΔk_r)
(d)
f_s(r)*Λ(r/Δr)
F̂(k_r)sinc²(k_r/N_rΔk_r)
(e)
(f)
(g)
F̂sinc² Unaliased Portion
F̂sinc² Positive Wraparound
F̂sinc² Negative Wraparound
0°
45°
(h)
22.5°
(i)

3.8 References

[1] W.N. Brouw. Aperture synthesis. *in* "Methods in Computational Physics. volume 14" (B. Alder. S. Fernbach. and M. Rotenberg. Eds.). pp. 131-175. Academic Press. New York. 1975.

[2] F.R. Schwab. Optimal gridding visibility data in radio interferometry. *in* "Indirect Imaging". (J.A. Roberts. Ed.). pp. 333-346. Cambridge University Press. New York. 1983.

[3] J.D. O'Sullivan. A fast sinc function gridding algorithm for Fourier inversion in computer tomography. *IEEE Trans. on Med. Imag.* **4(4)**. 200-207 (1985).

[4] J.I. Jackson. C.H. Meyer. D.G. Nishimura. A. Macovski. Selection of a convolution function for Fourier inversion using gridding. *IEEE Trans. on Med. Imag.* **10(3)**. 473-478 (1991).

[5] R.N. Bracewell. A.C. Riddle. Inversion of fan-beam scans in radio astronomy. *Astrophys. J.* **150**. 427-434 (1967).

[6] P.R. Smith. T.M. Peters. R.H.T. Bates. Image reconstruction from finite numbers of projections. *J. Phys. A: Math. Nucl. Gen.* **6**. 361-382 (1973).

[7] S.W. Rowland. Computer implementation of image reconstruction formulas. *in* "Image Reconstruction from Projections: Implementation and Applications" (G.T. Herman. Ed.). chapter 2. pp. 9-79. Topics in Applied Physics. volume 32. Springer Verlag. New York. 1979.

[8] J.W. Cooley. J.W. Tukey. An algorithm for the machine computation of complex Fourier series. *Math. Comput.* **19**. 297-301 (1965).

[9] R.N. Bracewell. "The Fourier Transform and its Applications". McGraw Hill. New York. 1986.

[10] C.E. Metz, K. Doi. Transfer function analysis of radiographic imaging sytems. *Phys. Med. Biol.* **24(6)**, 1079–1106 (1979).

[11] J.G. Pipe, J.L. Duerk. Analytical resolution and noise characteristics of linearly reconstructed magnetic resonance data with arbitrary *k*-space sampling. *Magn. Reson. Med.* **34**, 170–178 (1995).

[12] G.N. Ramachandran, A.V. Lakshminarayanan. Three-dimensional reconstruction from radiographs and electron micrographs: II. Application of convolutions instead of Fourier transforms. *Proc. Natl. Acad. Sci. USA* **68**, 2236–2240 (1971).

[13] W.A. Edelstein, G.H. Glover, C.J. Hardy, R.W. Redington. The intrinsic signal-to-noise ratio in NMR imaging. *Magn. Reson. Med.* **3**, 604–618 (1986).

[14] A. Macovski, Noise in MRI. *Magn. Reson. Med.* **36**, 494–497 (1996).

[15] R.N. Bracewell, A.R. Thompson, The main beam and ringlobes of an east-west rotation-synthesis array. *Astrophys. J.* **182**, 77–94 (1973).

[16] M.L. Lauzon, B.K. Rutt, Effects of polar sampling in k-space. *Magn. Reson. Med.* **36(6)**, 940–949 (1996).

[17] R.N. Bracewell, Strip integration in radio astronomy. *Aust. J. Phys.* **9**, 198–217 (1956).

[18] A.K. Jain, "Fundamentals of Digital Image Processing", Prentice-Hall Inc., Englewood Cliffs, New Jersey, 1989.

[19] A. Macovski, C. Meyer, A novel fast-scanning system. In *Proc of SMRM Fifth Ann Meet (WIP)*, pp. 156–157, Montreal, Canada, 1986.

[20] C.H. Meyer, B.S. Hu, D.G. Nishimura, A. Macovski, Fast spiral coronary artery imaging. *Magn. Reson. Med.* **28**, 202–213 (1992).

[21] E.O. Brigham. "The Fast Fourier Transform". Prentice-Hall. Englewood Cliffs. N.J.. 1974.

Chapter 4

T_2 Modulation Effects

4.1 Introduction

One major advantage of magnetic resonance imaging (MRI) is the flexibility of tissue characterization by various contrast mechanisms. The majority of clinical MRI acquisitions are based on T_1-weighting, proton density weighting, and T_2-weighting, and to a lesser extent on diffusion weighting and other novel contrast mechanisms.

T_1-weighted images have the added benefit of being acquired with short acquisition times. This translates into more efficient patient throughput, cost effectiveness, and less discomfort to the patient. The trade-off, though, is usually a signal-to-noise ratio (SNR) penalty.

However, it is the high contrast-to-noise ratio (CNR) T_2-weighted imaging techniques that prove to be clinically useful to the radiologist for generic components of pathology. But, proper T_2-weighted MR images such as from a conventional spin echo (SE) experiment require long acquisition times so that they are not influenced by any T_1-weighting.

In 1986, Hennig [1] proposed a fast T_2-weighted acquisition technique which goes under the names of RARE (*R*apid *A*cquisition with *R*elaxed *E*nhancement), FSE (*F*ast *S*pin *E*cho), or TSE (*T*urbo *S*pin *E*cho). In this treatise, these terms are used interchangeably. The acquisition time is shorter than conventional SE since multiple spin echoes in the echo train are assigned to different regions of k-space. Accordingly,

the time reduction with respect to conventional SE is the length of the echo train.

The first principles of FSE have been fully analyzed for Cartesian acquisitions [2], to some degree for projection reconstruction MRI (PR-MRI) [3], and not at all for concentric circles MRI (CC-MRI). Here, we analyze the T_2 modulation effects for both PR-MRI and CC-MRI polar acquisitions.

In the Theory section, we develop the T_2-weighting formalism which modulates the **k**-space data directly and leads to possible artifacts in the reconstructed image. In the Results section, we present some experimental verifications of the theory. The ramifications of T_2-weighting for polar **k**-space data are discussed.

4.2 Theory

The effect of T_2 modulation can be readily understood by considering the signal equation (developed in the Introduction chapter) and using basic Fourier theory. Recall that the acquired magnetization, ignoring field inhomogeneities, is given by

$$M(\mathbf{k},t) = \int_{-\infty}^{+\infty} m_{xy}^{o}(\mathbf{r})\,\epsilon^{-t/T_2(\mathbf{r})}\,\epsilon^{-2\pi i\mathbf{k}\cdot\mathbf{r}}\,d\mathbf{r} \tag{4.1}$$

where $m_{xy}^{o}(\mathbf{r})$ is the transverse magnetization spin-density and $\epsilon^{-t/T_2(\mathbf{r})}$ represents the T_2-weighting function which is both temporally and spatially dependent. This expression assumes mono-exponential T_2 decay at each position $\mathbf{r}$.

However, if we assume that the object is composed of N_s different T_2 species, then the j^{th} species of the T_2-weighted magnetization spin-density can be written as $m_{xy,j}^{o}(\mathbf{r})\,\epsilon^{-t/T_{2,j}}$, where $T_{2,j}$ is the T_2 spin-spin relaxation time constant of the j^{th} T_2 species. Note that the spatial and temporal dependences are now separately associated with the $m_{xy,j}^{o}$ and $\epsilon^{-t/T_{2,j}}$ terms, respectively.

Since the Fourier transform obeys the superposition principle (*i.e.* the addition theorem of Table 1.1), then the *net* magnetization is formed from the summation of all N_s different T_2 species, namely $\sum_{j=1}^{N_s} m_{xy,j}^{o}(\mathbf{r})\,\epsilon^{-t/T_{2,j}}$. Substituting this into Eq.(4.1), we can write the signal equation as

$$M(\mathbf{k},t) = \int_{-\infty}^{+\infty} \sum_{j=1}^{N_s} m_{xy,j}^{o}(\mathbf{r})\,\epsilon^{-t/T_{2,j}}\,\epsilon^{-2\pi i\mathbf{k}\cdot\mathbf{r}}\,d\mathbf{r} \tag{4.2}$$

By interchanging the order of the summation and integral symbols (which is permissible since the Fourier transform is a linear operator) and noting that $\epsilon^{-t/T_{2,j}}$ is independent of $\mathbf{r}$, we have

$$\begin{aligned} M(\mathbf{k},t) &= \sum_{j=1}^{N_s} \epsilon^{-t/T_{2,j}} \int_{-\infty}^{+\infty} m_{xy,j}^{o}(\mathbf{r})\,\epsilon^{-2\pi i\mathbf{k}\cdot\mathbf{r}}\,d\mathbf{r} \\ &= \sum_{j=1}^{N_s} \epsilon^{-t/T_{2,j}}\, M_o^j(\mathbf{k}) = \sum_{j=1}^{N_s} \epsilon^{-t/T_{2,j}}\, \mathcal{F}\left\{ I_o^j(\mathbf{r}) \right\} \end{aligned} \tag{4.3}$$

where $I_o^j(\mathbf{r})$ is the spin-density weighted image of the j^{th} T_2 species, and $\mathcal{F}$ denotes the Fourier transform operator.

Note how the total acquired k-space data are given by the sum of the k-space representation of the j^{th} T_2 species $M_o^j(\mathbf{k})$ exponentially weighted according to its T_2 value. This formalism allows one to characterize the effective T_2-weighting of the reconstructed images for both conventional and RARE-mode spin echo acquisitions.

In conventional spin echo (see Figure 4.1), the n^{th} echo in the echo train forms the n^{th} image at time TE=nESP, where ESP and TE are the echo spacing and echo time, respectively. The k-space magnetization and MR image are given by

$$M_{se}(\mathbf{k}) = \sum_{j=1}^{N_s} \epsilon^{-\mathrm{TE}/T_{2,j}} \mathcal{F}\left\{ I_o^j(\mathbf{r}) \right\} \tag{4.4}$$

$$I_{se}(\mathbf{r}) = \mathcal{F}^{-1}\left\{ M_{se}(\mathbf{k}) \right\} = \sum_{j=1}^{N_s} \epsilon^{-\mathrm{TE}/T_{2,j}} I_o^j(\mathbf{r}) \tag{4.5}$$

Thus, the reconstructed image is made up of the sum of the N_s individual T_2 species images, each one scaled according to its T_2 value.

Since the k-space data are acquired at one effective echo time, the T_2-weighting function is independent of the spatial frequency coordinate ($\mathbf{k}$). Consequently, the T_2 contrast for a conventional SE acquisition is only dependent on the echo time (TE) and on the T_2 values of the N_s different T_2 species. Short T_2 species will be reduced in intensity relative to longer T_2 species, and so a T_2-weighted contrast is achieved.

By comparison, in RARE-mode acquisitions, multiple echoes within the echo train are used within the same k-space, as shown in Figure 4.2. In so doing, different regions of k-space are encoded at different echo times, *i.e.* $\mathbf{k}(t)$. One can invert this such that the temporal coordinate is dependent on the spatial frequency location, namely $t \rightarrow t(\mathbf{k})$. By writing it this way, the temporal dependence in Eq.(4.3) can be written as a spatial frequency dependence. Consequently, the acquired RARE-mode k-space data and MR image are given by

$$M_{rare}(\mathbf{k}) = \sum_{j=1}^{N_s} \epsilon^{-t(\mathbf{k})/T_{2,j}} \mathcal{F}\left\{ I_o^j(\mathbf{r}) \right\} \tag{4.6}$$

$$I_{rare}(\mathbf{r}) = \mathcal{F}^{-1}\left\{ M_{rare}(\mathbf{k}) \right\} = \sum_{j=1}^{N_s} \mathcal{F}^{-1}\left\{ \epsilon^{-t(\mathbf{k})/T_{2,j}} \right\} \star I_o^j(\mathbf{r}) \tag{4.7}$$

where the $\star$ symbol denotes convolution, and we have used the Fourier convolution theorem [4, p.108]. Although not explicitly stated previously, the inverse Fourier transform operation required to go from $M(\mathbf{k})$ to $I(\mathbf{r})$ is performed over the spatial frequency $\mathbf{k}$-coordinate only, which is why we parameterize time as a function of spatial frequency.

Unlike the conventional SE acquisition, T_2 modulation in RARE-mode acquisitions leads to a more complicated effect than mere scaling. Rather, the j^{th} T_2 species is blurred (*i.e.* smeared) and perhaps replicated via the convolution process. An understanding of the functional form of $\epsilon^{-t(\mathbf{k})/T_{2,j}}$ is therefore warranted.

If the j^{th} T_2 species is represented as a point object or impulse, *i.e.* $I_j(\mathbf{r}) = \delta(\mathbf{r})$, then $\mathcal{F}^{-1}\left\{\epsilon^{-t(\mathbf{k})/T_{2,j}}\right\}$ is said to be the T_2 impulse response function (IRF). Note that there are different T_2 IRFs for each T_2 species.

In analogy to the conventional SE acquisition, in RARE-mode acquisitions each T_2 species is affected according to its respective T_2 impulse response function. For conventional SE, the T_2 IRF is merely a scalar which modifies the intensity of the respective T_2 species, whereas for RARE-mode acquisitions, the T_2 IRF is a spatially varying function which scales, smears, and blurs the respective T_2 species.

Moreover, since the T_2-weighting function in RARE-mode acquisitions is dependent on the spatial frequency, the $\mathbf{k}$-space trajectory plays an integral part in the functional form of the T_2-weighting function: the image contrast and $\mathbf{k}$-space trajectory are no longer separable for these types of acquisition. Thus, the T_2-weighting and T_2 IRF functions of PR-MRI and CC-MRI are analyzed separately.

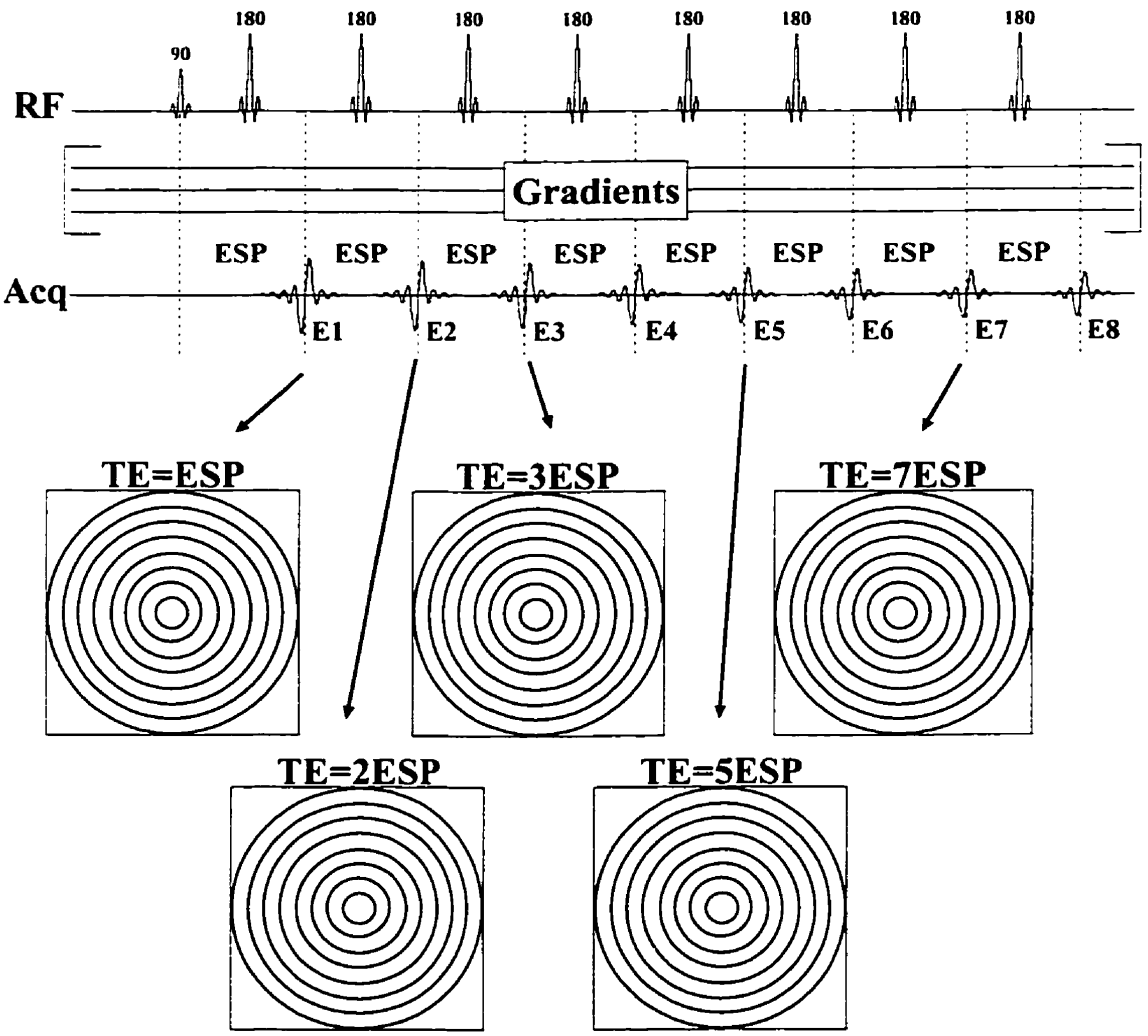

Figure 4.1: Conventional spin echo k-space representation
Each of the n echoes within the echo train (labelled E1-E8) is encoded within one k-*space matrix. The data (shown here as CC-MRI) are collected at one effective echo time given by TE=nESP.*

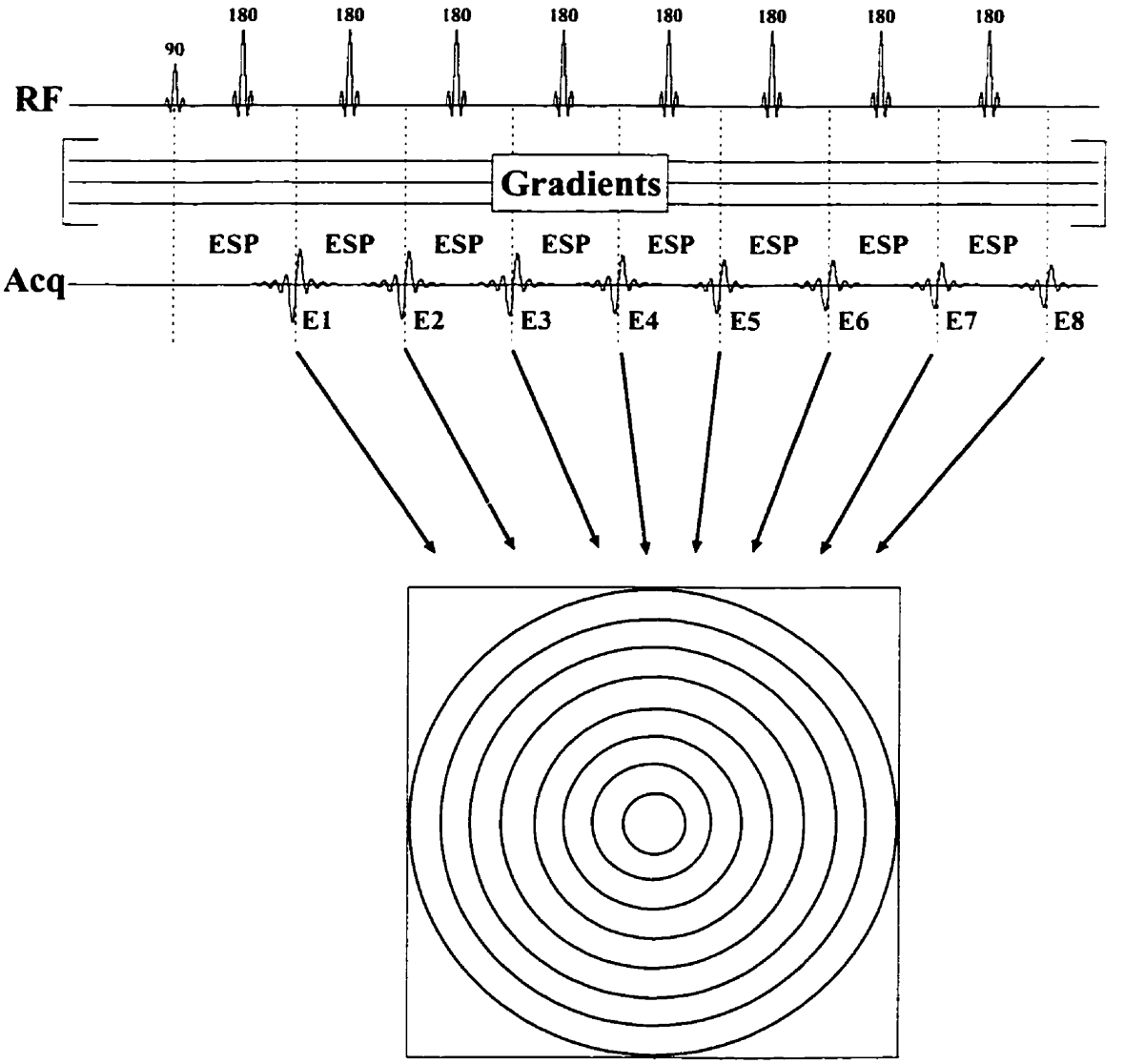

Figure 4.2: RARE-mode spin echo k-space representation
All of the n echoes (labelled E1–E8) are encoded within the same **k**-*space matrix. The data (shown here as CC-MRI) are amplitude modulated by the* T_2-*weighting function* $\exp\left(\frac{-t(\mathbf{k})}{T_2}\right)$.

4.2.1 Projection Reconstruction

For projection reconstruction MRI, the readout direction (on the order of a few milliseconds) is in the radial direction. Thus, for RARE-mode PR-MRI, the T_2-weighting occurs along the azimuthal direction and cannot be circularly symmetric or isotropic. This has the potential of introducing artifacts into the reconstructed MR image.

In 1994, Rasche [3] surmised that RARE-mode PR-MRI, which he termed Radial TSE, could provide a familiar contrast behaviour at a reduced scan time. Rasche analyzed the T_2 impulse response function and effective TE for RARE-mode PR-MRI. Here, we present some of our own findings which differ from Rasche's. In fact, we show that Rasche's analysis may be in error. Moreover, the formalism and analysis of T_2 contrast method presented herein is general and can be applied to any k-space trajectory.

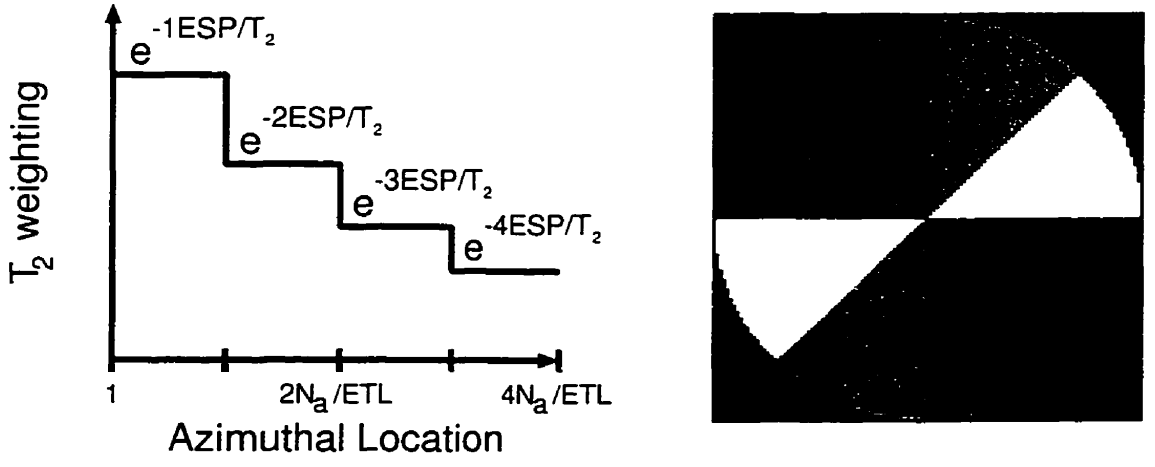

Figure 4.3: PR-MRI T_2-weighted banding approach
The T_2-weighting in the azimuthal direction is made up of bands of echoes at the same echo time nESP. The 1D representation along the azimuthal direction is shown on the left, while its 2D representation is shown on the right.

Many types of modulation functions are permissible. The first approach follows readily from the Cartesian RARE-mode acquisition, here called the *banding* approach, as shown in Figure 4.3. The azimuthal T_2-weighting is displayed assuming N_a projections within 0–π and an echo train length (ETL) of 4 echoes. In this approach, the

first echo of each excitation is encoded such that the projection lies within $\left(0, \frac{\pi}{\text{ETL}}\right)$. the second echo projection lies within $\left(\frac{\pi}{\text{ETL}}, \frac{2\pi}{\text{ETL}}\right)$, and so on.

The normalized T_2 impulse response function with an echo spacing ESP=15ms, an echo train length ETL=4 echoes, N_a=192 projections, N_r=128 points per projection, and a T_2 value of 25ms is shown in Figure 4.4. Here, we display the magnitude of the T_2 IRF in decibels (dBs), *i.e.* $10\log_{10}(|\text{IRF}|)$.

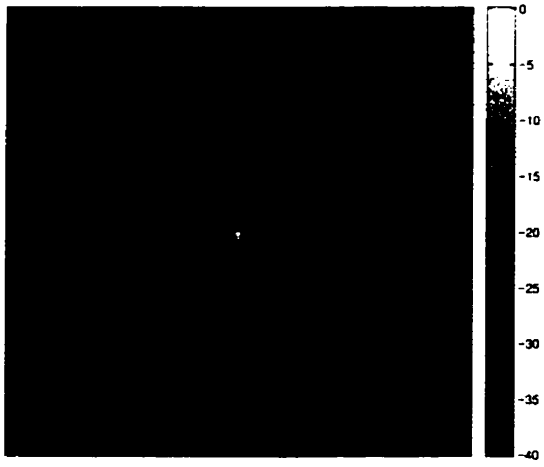

Figure 4.4: PR-MRI T_2 impulse response function for the banding approach
The normalized T_2 impulse response function is displayed in dBs for an ETL of 4 echoes. N_a=192 projections. N_r=128 points per projection. an ESP of 15ms. and a T_2 value of 25ms. The corresponding linear gray scale colourbar is also shown.

Note the asymmetry of the impulse response function due to the junctions occurring between successive bands. Simulations show that such a T_2-weighting scheme leads to severe smearing in the reconstructed image. This is demonstrated in Figure 4.5 for the reconstruction (using convolution backprojection) of a synthetic noisy disk phantom with an SNR$\simeq$100.

The second approach, termed the *sequential* approach, depicts the echoes being sequentially ordered along the azimuthal direction, as shown in Figure 4.6. Once again we have assumed an ETL of 4 echoes. For display purposes, we chose N_a=24 projections (within 0–π) and N_r=128 points per projection. In practice, however, one would have N_a on the order of $\frac{\pi}{2}N_r$ to avoid azimuthal streaking artifacts, as

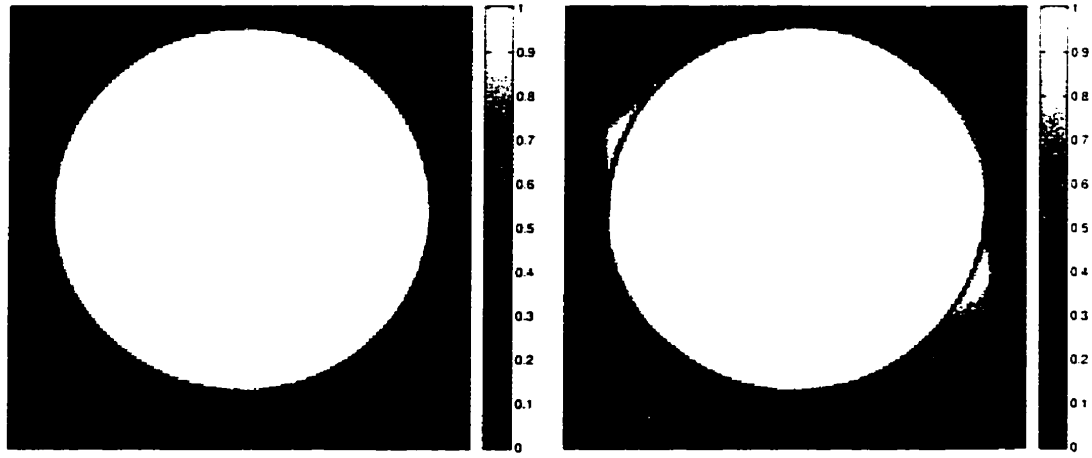

Figure 4.5: PR-MRI image reconstruction effect for the banding approach
The effect of the PR-MRI banding approach is shown for a synthetic disk phantom (left) being severely smeared (right) when subjected to the banding approach with ESP=15ms, ETL=4 echoes, N_a=192 projections, N_r=128 points per projection, and T_2=25ms. The corresponding linear gray scale colourbars are also shown: the two images are at the same windowing level.

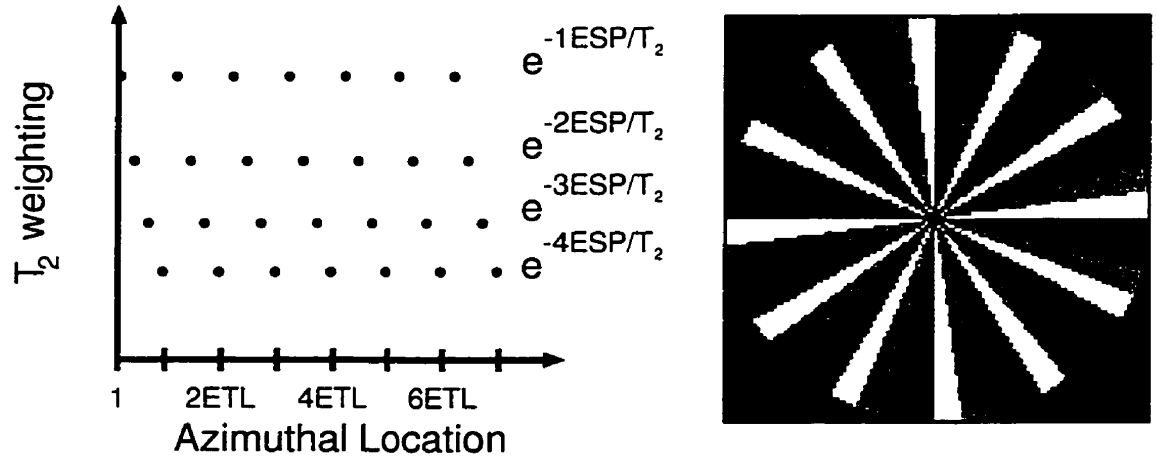

Figure 4.6: PR-MRI T_2-weighted sequential approach
The T_2-weighting in the azimuthal direction is sequential with echo time. The 1D representation along the azimuthal direction is shown on the left, while its 2D representation is shown on the right.

explained in the Reconstruction Effects chapter. Its 2D representation is also shown for comparison with that of Figure 4.3.

Although the junctions still exist at every multiple of ETL along the azimuthal direction, the T_2-weighting function exhibits a more symmetrical appearance since the junctions are distributed throughout. This also leads to a more symmetrical T_2 impulse response function. The normalized magnitude T_2 IRF (in dBs) is shown in Figure 4.7 assuming an ESP of 15ms, an ETL of 4 echoes, N_a=192 projections within 0–π, N_r=128 points per projection, and a T_2 value of 25ms.

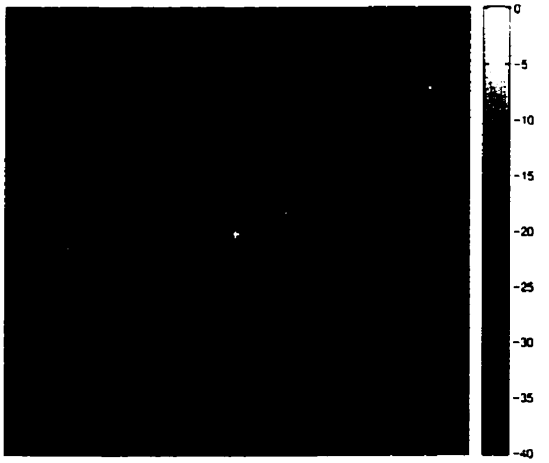

Figure 4.7: PR-MRI T_2 impulse response function for the sequential approach
The normalized T_2 impulse response function is displayed in dBs for an ETL of 4 echoes. N_a=192 projections. N_r=128 points per projection, an ESP of 15ms, and a T_2 value of 25ms. The corresponding linear gray scale colourbar is also shown.

In comparison to Figure 4.4, the sequential T_2 IRF of Figure 4.7 appears more uniform and pseudo-isotropic, is four-fold symmetric, and there is more distributed energy away from the centre. The reconstruction of a noiseless synthetic disk phantom (depicted in Figure 4.8) shows little smearing artifacts, but slight streaking (*i.e.* star-like) artifacts outside the object emanating from the edges of the disk phantom. This effect arises due to the star-like appearance of the T_2 IRF (as shown in Figure 4.7).

The third and final approach depicts the *interleaved* approach. The ordering is similar to the sequential approach except that one tries to *maximize* the number of

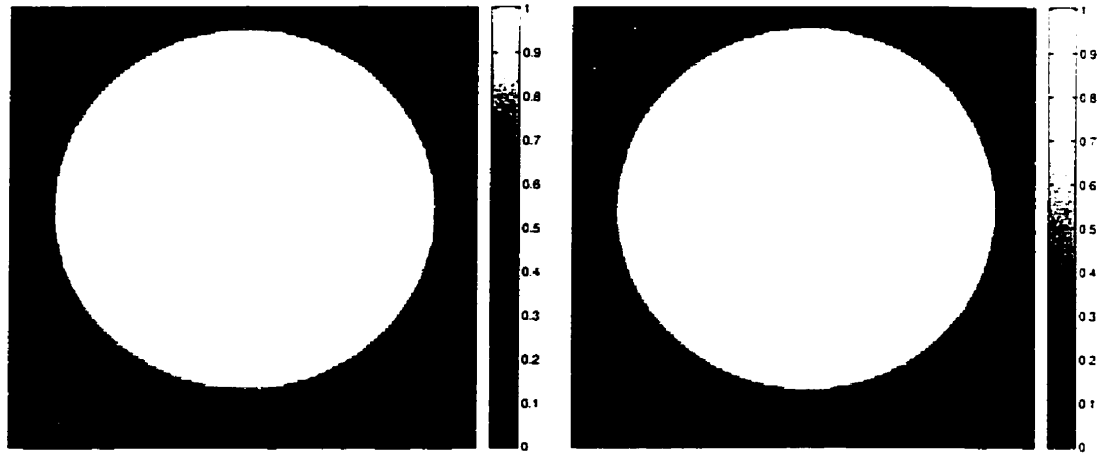

Figure 4.8: PR-MRI image reconstruction effect for the sequential approach
The effect of the PR-MRI sequential approach is shown for a reconstructed synthetic noiseless disk phantom. The parameters are ESP=15ms, ETL=16 echoes, N_t=192 projections, N_r=128 points per projection, and T_2=25ms. The image on the right is the same as that on the left but at a higher brightness level to accentuate the star-like artifacts (note the different gray scale colourbars).

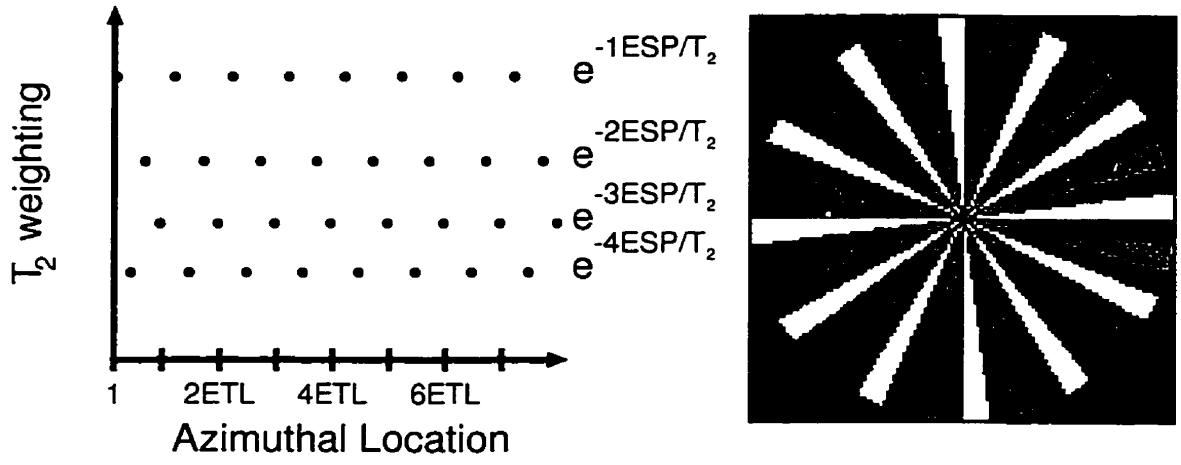

Figure 4.9: PR-MRI T_2-weighted interleaved approach
The T_2-weighting in the azimuthal direction is interleaved with echo time, as explained in the text. The 1D representation along the azimuthal direction is shown on the left, while its 2D representation is shown on the right.

junctions in the T_2-weighting function. Therefore, the first half of the echo train is encoded sequentially at the odd azimuthal locations, while the second half of the echo train is encoded in a reverse sequential fashion at the even azimuthal locations. An example helps to elucidate the approach.

If the echo train length is 8 and the echoes are labelled E1–E8, then the azimuthal ordering is {E1,E8,E2,E7,E3,E6,E4,E5}. Figure 4.9 depicts the case of ETL=4 echoes and N_a=24 projections (for display purposes only). The 2D representation can be directly compared to that of Figure 4.6 since the ESP and T_2 values are the same in these two cases. Note that in the interleaved approach, one introduces more intense junctions than the banding or sequential approaches in an attempt to minimize the coherence of T_2-weighting in the azimuthal direction.

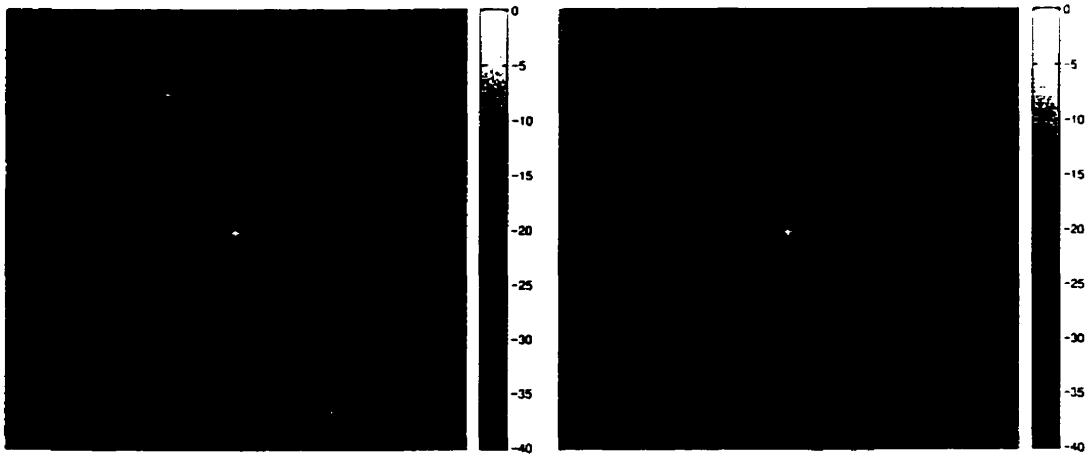

Figure 4.10: PR-MRI T_2 impulse response function for the interleaved approach
The normalized T_2 impulse response functions are displayed in dBs for an ETL of 4 echoes, N_a=192 projections, N_r=128 points per projection, an ESP of 15ms, and T_2 values of 25ms (left) and 80ms (right). The corresponding linear gray scale colourbars are also shown; the two images are at the same windowing level.

The normalized magnitude T_2 impulse response function (in dBs) is shown in Figure 4.10 assuming an ESP of 15ms, an ETL of 4 echoes, N_a=192 projections, N_r=128 points per projection, and T_2 values of 25ms and 80ms. Comparison of the T_2=25ms sequential and interleaved IRF images of Figures 4.7 and 4.10, respectively,

shows that the interleaved approach appears slightly more diffuse than the sequential T_2 IRF, and there is less energy in the spokes. This leads to reduced star-like and smearing artifacts in the reconstructed MR image.

In Figure 4.10, one can clearly observe that for longer T_2 species, the IRF has reduced intensity in the spokes. This leads to reduced blurring effects for long T_2 species relative to short T_2 species.

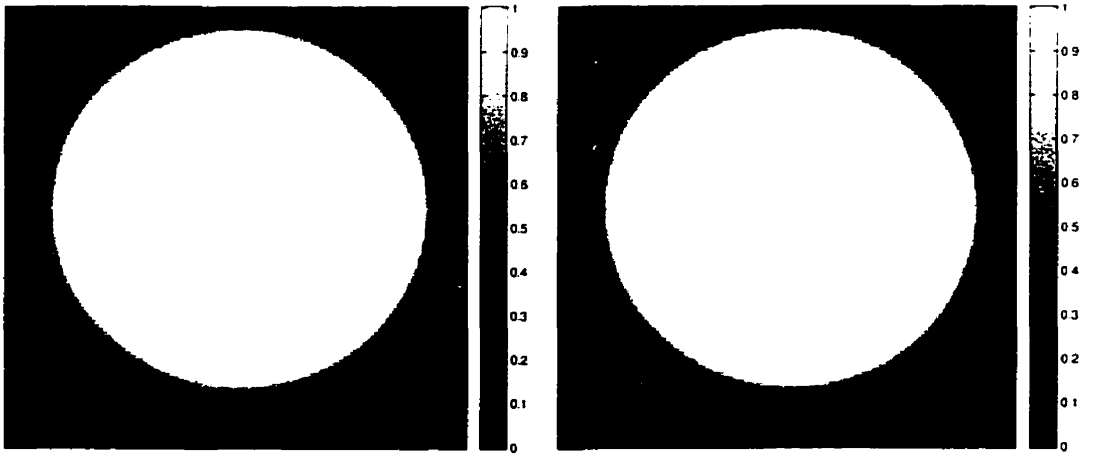

Figure 4.11: PR-MRI image reconstruction effect for the interleaved approach
The effect of the PR-MRI interleaved approach is shown for a reconstructed synthetic disk phantom with SNR≃45. The parameters are ESP=15ms, ETL=16 echoes, N_a=192 projections, N_r=128 points per projection, and T_2=25ms. The image on the left is the reconstructed disk subjected to the sequential approach, while the image on the right is for the interleaved approach. Note the reduced signal outside the object for the interleaved approach. The corresponding linear gray scale colourbars are also shown; the two images are at the same bright windowing level to accentuate the star-like artifacts.

The reconstruction of a synthetic disk phantom of SNR≃45 subjected to the interleaved approach is shown on the right of Figure 4.11. For comparison, the same disk phantom subjected to the sequential approach is shown on the left. The T_2-weighting parameters include ESP=15ms, ETL=16 echoes, N_a=192 projections, N_r=128 points per projection, and a T_2 value of 25ms. The interleaved approach image has slightly less signal (about 5%) outside the object (*i.e.* reduced star-like artifact), and the SNR is slightly greater (~46 *vs.* ~44) in comparison to the sequential approach.

For PR-MRI the azimuthal junction artifact is difficult to avoid. However, one could adopt a two-sided approach to eliminate the junctions altogether. For example, the one-sided sequential approach for ETL=4 echoes is

{E1.E2.E3.E4.E1.E2.E3.E4.E1.E2.E3.E4.E1...}

which has junctions between the E4 and E1 echoes. In the two-sided sequential approach, the azimuthal weighting would be (for ETL=4 echoes)

{E1.E2.E3.E4.E4.E3.E2.E1.E1.E2.E3.E4.E4...}

which no longer has a junction between the E4 and E1 echoes.

But, the two-sided approach emphasizes the star-like pattern of T_2-weighting which leads to an enhanced star-like appearance in the T_2 IRF. This has the deleterious effect of enhancing streaking artifacts in the reconstructed image. The two-sided interleaved approach, which was suggested by Rasche [3], also suffers from increased star-like artifacts. The PR-MRI one-sided interleaved approach proposed here, though, appears to be a good compromise in minimizing smearing and star-like artifacts in the image.

The effective echo time of PR-MRI RARE-mode acquisitions (TE_{pr}) is somewhat more difficult to ascertain. Since it is the centre of **k**-space that dictates the overall contrast of the object, the effective TE is the time at which one samples the central **k**-space data. But, in PR-MRI *all* the projections within the echo train traverse the centre of **k**-space.

Nevertheless, an effective echo time can be derived if we assume that the object being imaged is circularly symmetric and centred within the field of view (FOV). In this case, all the projections are identical, except for an amplitude variation owing to T_2 modulation.

To provide stronger T_2-weighting, say, one may wish to acquire the first echo at time ESP_0 which may be different than the echo spacing ESP of subsequent echoes. This may be achieved either by delaying the acquisition time of the echo train, or by

not acquiring the first m echoes in the echo train. Furthermore, if $ESP_0 > ESP$, the lipid signal is reduced due to J-coupling effects (*i.e.* scalar coupling). Consequently, the signal intensity fraction of RARE-mode PR-MRI relative to a conventional spin echo PR-MRI acquisition collected at time $TE = ESP_0$ is given by

$$\mathcal{S}_{pr} = \frac{\sum_{n=0}^{ETL-1} \frac{N_a}{ETL} \epsilon^{-(ESP_0 + n ESP)/T_2}}{\sum_{n=1}^{N_a} \epsilon^{-ESP_0/T_2}} = \frac{1}{ETL} \sum_{n=0}^{ETL-1} \epsilon^{-n ESP/T_2} \qquad (4.8)$$

Note that $\mathcal{S}_{pr}$ is independent of ESP_0 since the fraction is *relative* to that echo time. Recognizing Eq.(4.8) as a finite geometric series, it can be rewritten as

$$\mathcal{S}_{pr} = \frac{1}{ETL} \frac{1 - \exp\left(-\frac{ESP \times ETL}{T_2}\right)}{1 - \exp\left(-\frac{ESP}{T_2}\right)} \qquad (4.9)$$

The signal intensity fractions are plotted in Figure 4.12 at various ETL values assuming ESP=15ms for T_2 values within the range 1–500ms.

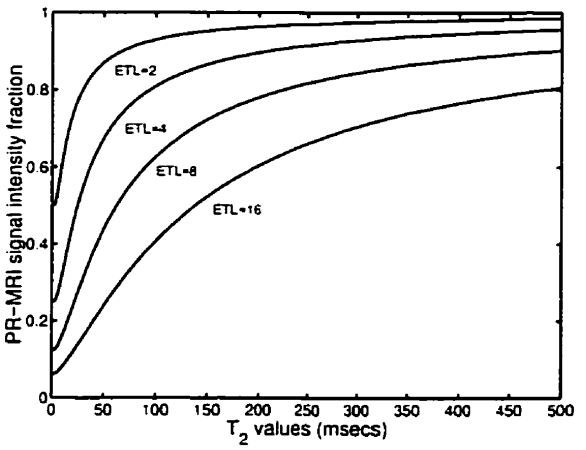

Figure 4.12: PR-MRI signal intensity fraction curves
The PR-MRI signal intensity fraction curves are plotted assuming an echo spacing ESP=15ms.

It may be instructive to consider a few limiting cases. First, if ETL=1 echo, then the fraction containing the exponentials in $\mathcal{S}_{pr}$ reduces to one so that $\mathcal{S}_{pr}$ is unity. This is as expected since there is effectively no T_2 modulation: this represents the conventional SE acquisition.

Second, in the limit of $T_2 \rightarrow \infty$, the Taylor series expansion of the fraction of exponentials term tends to ETL such that $\mathcal{S}_{pr}$ is unity. This is also as expected since an infinite T_2 would not suffer any T_2 signal intensity decay.

Third, in the limit of $T_2 \rightarrow 0$, the exponential terms in T_2 are much smaller than one. Thus, $\mathcal{S}_{pr}$ tends to $\frac{1}{\mathrm{ETL}}$ for $T_2 \rightarrow 0$, as observed in Figure 4.12.

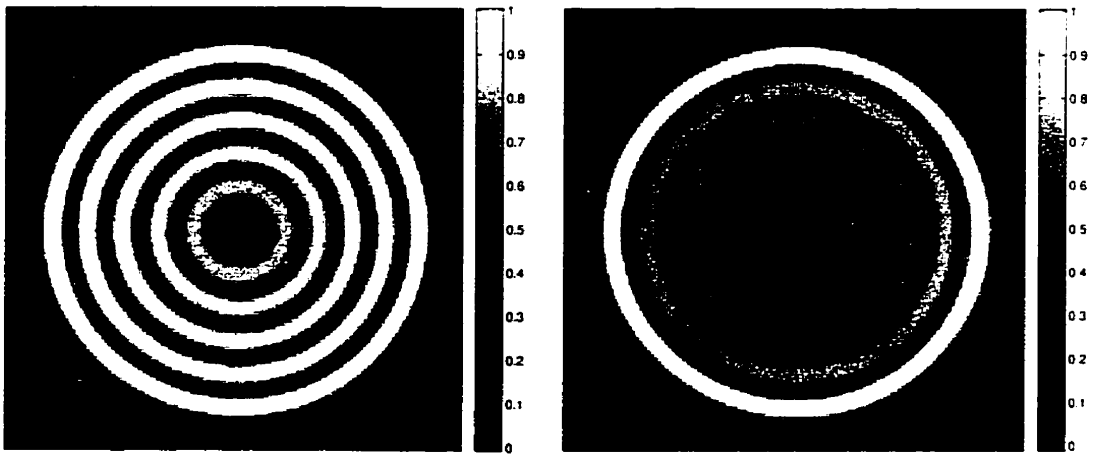

Figure 4.13: PR-MRI signal intensity fraction synthetic phantom images
The synthetic phantom consists of 6 rings with T_2 values of 25ms, 80ms, 110ms, 180ms, 280ms, from the centre outwards with the largest ring having an infinite T_2. The image on the left is the conventional SE PR-MRI image (TE=15ms), whereas the image on the right is the RARE-mode PR-MRI image with ETL=8 echoes, N_a=384 projections, N_r=128 points per projection, and ESP=15ms. These images are at the same windowing level.

Numerical verification of Eq.(4.9) was carried out in the following manner. We generated a synthetic phantom consisting of a series of concentric rings of various T_2 values, as shown on the left of Figure 4.13. The k-space data (128 radial points per projection by 384 projections within 0–π) were synthesized for each ring, and the appropriate one-sided interleaved T_2-weighting was determined for each different T_2 species. Two composite images were formed, namely the conventional SE PR-MRI image and the RARE-mode image. These are depicted in Figure 4.13 on the left and right, respectively.

The composite k-space data sets were reconstructed using the convolution back-

projection algorithm. The outer ring was chosen to have an infinite T_2 (so that its $\mathcal{S}_{pr}$ is unity for all ESP/ETL combinations), and all images were normalized to unity with respect to this outer ring.

The PR-MRI signal intensity fraction was then calculated from the ratio of the RARE image to that of the conventional SE image for the respective T_2 rings. The signal intensity fractions were found to correspond to theoretical expectations of Eq.(4.9) within $\pm 1\%$ for various ESP (15ms, 20ms, 30ms, 40ms) and ETL (1, 2, 4, 8, 16, 32) combinations for T_2 values within 1–500ms.

The PR-MRI effective echo time TE_{pr} is given by the expected T_2-weighting at time ESP_0 multiplied by $\mathcal{S}_{pr}$, namely $\epsilon^{-\mathrm{TE}_{pr}/T_2} = \mathcal{S}_{pr}\epsilon^{-\mathrm{ESP}_0/T_2}$, from which

$$\begin{aligned} \mathrm{TE}_{pr} &= \mathrm{ESP}_0 - T_2 \log \mathcal{S}_{pr} \\ &= \mathrm{ESP}_0 - T_2 \log \left\{ \frac{1}{\mathrm{ETL}} \frac{1 - \exp\left(-\frac{\mathrm{ESPxETL}}{T_2}\right)}{1 - \exp\left(-\frac{\mathrm{ESP}}{T_2}\right)} \right\} \end{aligned} \tag{4.10}$$

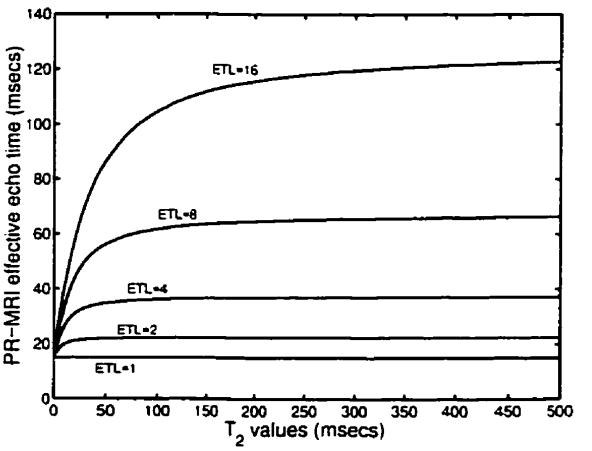

Figure 4.14: PR-MRI effective TE curves

The PR-MRI effective echo time curves are plotted assuming an echo spacing ESP=15ms, and ESP_0=ESP=15ms. Note that the ETL=1 echo curve (which represents the conventional SE acquisition) has $\mathrm{TE}_{pr}=\mathrm{ESP}_0$ for all T_2 values.

The TE_{pr} is plotted in Figure 4.14 for the various signal intensity fraction curves of Figure 4.12 (ESP=15ms) and setting ESP_0=ESP=15ms. Note the rapid increase in effective echo time for short T_2 species and the somewhat 'flat' region at larger

T_2 values. In reality, this region is tending to the asymptotic TE_{pr} limit for a given ESP_0, ESP, and ETL combination, as shown below.

Again, it is instructive to consider a few limiting cases. First, for ETL=1 echo, we previously found that $\mathcal{S}_{pr}$ tends to unity, so that $\log \mathcal{S}_{pr}$ tends to zero and $TE_{pr}=ESP_0$ for all T_2 values since TE_{pr} is independent of T_2 in this case. This is as expected since the ETL=1 echo case represents the conventional SE acquisition.

Second, in the limit of $T_2 \rightarrow 0$, $\mathcal{S}_{pr}$ tends to $\frac{1}{ETL}$, but the $T_2 \log \mathcal{S}_{pr}$ term tends to zero (since T_2 tends to zero) so that $TE_{pr}=ESP_0$. Consequently, all curves in Figure 4.13 start at $TE_{pr}=ESP_0$ and increase as a function of T_2.

Third, in the limit of $T_2 \gg$ ESPxETL, one can show that the Taylor series expansion of the logarithmic term reduces to $-\frac{ESP(ETL-1)}{2T_2}$. Thus, the $-T_2 \log \mathcal{S}_{pr}$ term tends to $\frac{1}{2}$ESP(ETL-1) and

$$TE_{pr} = ESP_0 + \frac{1}{2}ESP(ETL-1) \qquad \text{for } T_2 \gg ESPxETL \tag{4.11}$$

If ESP_0=ESP, then the TE_{pr} asymptote is given by $\frac{1}{2}$ESP(ETL+1).

Using the nomenclature established in this section and assuming ESP_0=ESP, Rasche [3] determined TE_{pr} to be given by

$$TE_{pr}^{Rasche} = -T_2 \log\left\{\frac{T_2}{ESPxETL}\left[1-\exp\left(-\frac{ESPxETL}{T_2}\right)\right]\right\} \tag{4.12}$$

For the above, one can show that for $T_2 \gg$ ESPxETL the Taylor series expansion of the logarithmic term reduces to $-\frac{ESPxETL}{2T_2}$, so that TE_{pr} tends to $\frac{1}{2}$ESPxETL. This is close but not exactly equal to what was derived above (for ESP_0=ESP).

Note, however, that for ETL=1 echo, Rasche predicts an effective echo time of ESP/2 for large T_2 values even though all the projections were acquired at an echo time of ESP. Moreover, the effective echo time is less than ESP ($=ESP_0$) for short T_2 values. In fact, for $T_2 \rightarrow 0$, one can show (using l'Hospital's rule) that TE_{pr} tends to zero, again less than the acquisition time of the first echo. Consequently, it is felt that Rasche's analysis may be in error.

In all fairness to Rasche, one can show that the effective TE of Eq.(4.10) from our analysis reduces to Rasche's effective TE of Eq.(4.12) if one assumes that (1) $ESP_0=0$, and (2) $T_2 \gg ESP$ so that the $1-\epsilon^{-ESP/T_2}$ term can be written as ESP/T_2. Still, these assumptions are overly restrictive and do not represent the general case.

Experimental verification (found in the Results section) of the theoretical expectations of the PR-MRI signal intensity fraction, and by implication that of the effective echo time TE_{pr}, substantiates our above analysis for PR-MRI.

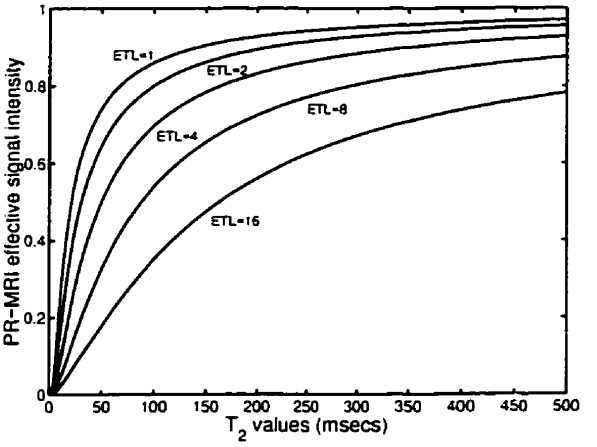

Figure 4.15: PR-MRI effective signal intensity curves
The PR-MRI effective signal intensity curves are plotted assuming an echo spacing ESP=15ms, and ESP_0=ESP=15ms.

Finally, by knowing the effective echo time TE_{pr}, one can calculate the effective signal intensity from ϵ^{-TE_{pr}/T_2}. This is plotted in Figure 4.15 for the various effective echo time curves of Figure 4.14 with ESP_0=ESP=15ms. Note the small signal intensity for short T_2 species, as expected. The ETL=1 echo curve is the conventional SE case and represents the T_2 contrast curve ϵ^{-ESP_0/T_2}.

4.2.2 Concentric Circles

In contrast to projection reconstruction MRI, the readout direction for concentric circles acquisitions (CC-MRI) occurs in the azimuthal direction. Therefore, for RARE-mode CC-MRI, the T_2-weighting occurs in the radial direction. Unlike PR-MRI, the T_2 modulation is circularly symmetric, which leads to a circularly symmetric T_2 impulse response function.

Previous work by Block [5] introduced RARE spiral acquisitions wherein it was mentioned that the T_2-weighting should be smoothly varying, and one should attempt to minimize the T_2-weighting variations. However, little justification was given. Here, we show that for CC-MRI the T_2-weighting should not only be smoothly varying, but also monotonically decaying to avoid introducing any further artifacts.

The first T_2-weighting approach follows readily from the PR-MRI banding approach except that for CC-MRI the bands occur in the radial direction. If the maximal radial location is given as k_r^{max}, then in the CC-MRI banding approach the first echo is encoded to lie within $|k_r| \leq \frac{k_r^{max}}{\text{ETL}}$, the second echo lies within $\frac{k_r^{max}}{\text{ETL}} \leq |k_r| \leq \frac{2k_r^{max}}{\text{ETL}}$, and so on. This is depicted in Figure 4.16 for ETL=4 echoes.

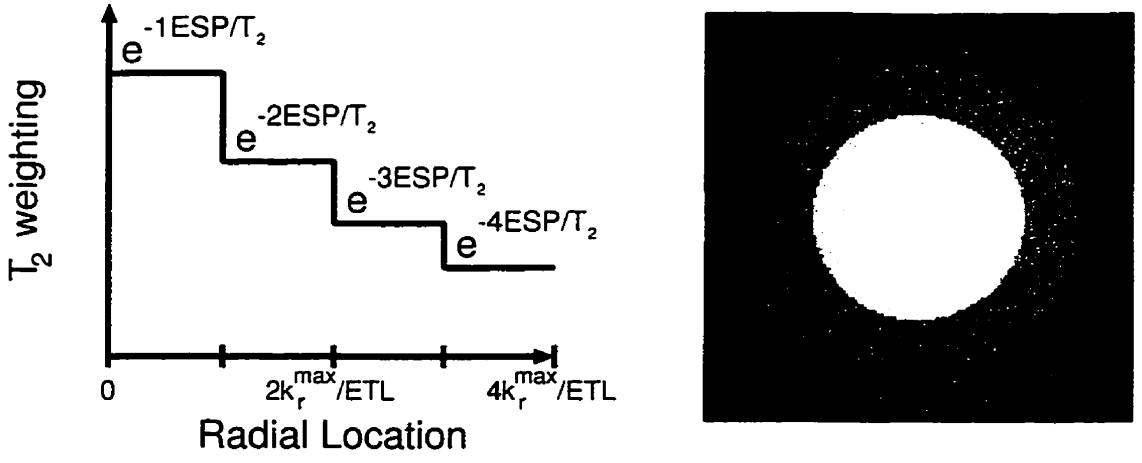

Figure 4.16: CC-MRI T_2-weighted banding approach
The T_2-weighting in the radial direction is made up of bands of echoes at the same echo time nESP. The 1D representation along the azimuthal direction is shown on the left, while its 2D representation is shown on the right.

Because of circular symmetry, one can use the Fourier-Bessel (*i.e.* Hankel) transform to calculate the T_2 impulse response function. Moreover, in analogy to PR-MRI RARE-mode acquisitions, one may wish to provide stronger T_2-weighting. Consequently, we assume that the first acquired echo occurs at time ESP_0 and that all subsequent echoes have an echo spacing ESP. The 1D weighting of Figure 4.16 can then be written as

$$\sum_{n=0}^{\mathrm{ETL}-1} \epsilon^{-(\mathrm{ESP}_0+n\mathrm{ESP})/T_2} \left\{ \Pi\left(\frac{\mathrm{ETL}\,k_r}{2[n+1]k_r^{max}}\right) - \Pi\left(\frac{\mathrm{ETL}\,k_r}{2nk_r^{max}}\right) \right\} \qquad (4.13)$$

where $k_r \geq 0$, we have used the definition of the "rect" function $\Pi(\xi)$ to be unity for $\xi \leq 1/2$ and zero otherwise, and for $n=0$ we assume that the second rect function is identically zero (since it is undefined in that case).

From Bracewell [4, p.249], the Hankel transform of the rect function is proportional to the jinc function, which is the circular analog of the sinc function. Therefore, the T_2 IRF for the CC-MRI banding approach is proportional to

$$\sum_{n=0}^{\mathrm{ETL}-1} \epsilon^{-n\mathrm{ESP}/T_2} \left\{ (n+1)^2 \,\mathrm{jinc}\left(2\pi r(n+1)\frac{k_r^{max}}{\mathrm{ETL}}\right) - n^2\,\mathrm{jinc}\left(2\pi rn\frac{k_r^{max}}{\mathrm{ETL}}\right) \right\} \qquad (4.14)$$

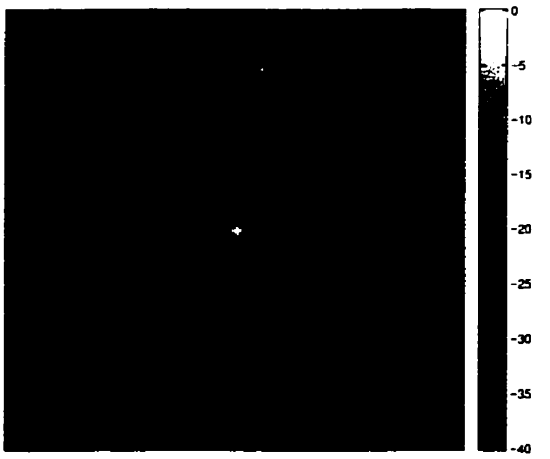

Figure 4.17: CC-MRI T_2 impulse response function for the banding approach
The normalized T_2 impulse response function is displayed in dBs for an ETL of 4 echoes. N_r=128 points per projection, N_a=192 projections, an ESP of 15ms, and a T_2 value of 25ms. The corresponding linear gray scale colourbar is also shown.

The normalized T_2 impulse response function with an echo spacing ESP=15ms, an echo train length ETL=4 echoes, N_r=128 points per projection, N_a=192 projections, and a T_2 value of 25ms is shown in Figure 4.17. We display the magnitude of the T_2 IRF in decibels (dBs), as before.

Simulations show that such a T_2-weighting scheme leads to ring-like artifacts in the reconstructed image. This is demonstrated in Figure 4.18 for the reconstruction (using convolution backprojection) of a synthetic noisy disk phantom with SNR$\simeq$100 and assuming T_2-weighting parameters of ETL=4 echoes, N_r=128 points per projection, N_a=192 projections, ESP$_0$=ESP=15ms, and a T_2 of 25ms. These ring-like artifacts are due to the junctions between the radial bands at multiples of $\frac{k_r^{max}}{\mathrm{ETL}}$ in the T_2-weighting function (see Figure 4.16).

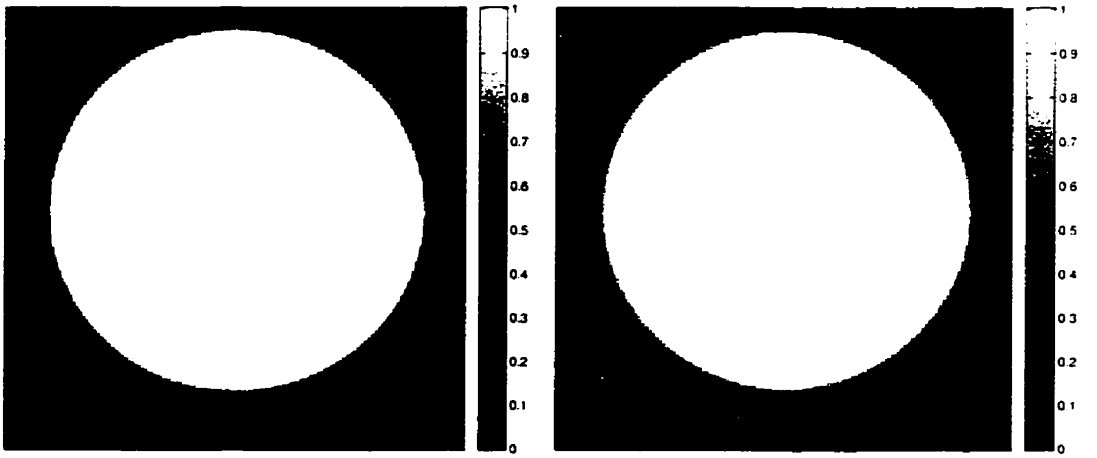

Figure 4.18: CC-MRI image reconstruction effect for the banding approach
The effect of the CC-MRI banding approach is shown for a synthetic disk phantom (left) having ringing artifacts (right) when subjected to the banding approach with ESP=15ms, ETL=4 echoes, N_r=128 points per projection, N_a=192 projections, and T_2=25ms. The corresponding linear gray scale colourbars are also shown: the two images are at the same windowing level.

Since the junctions occurring between successive bands lead to ring-like artifacts in the reconstructed image, a better approach is to produce a smoothly varying, but still monotonically decaying T_2-weighting, as shown in Figure 4.19.

The T_2-weighting function is given by $e^{-t(k_r)/T_2}$ since it occurs in the radial direc-

tion for CC-MRI. This must be rewritten as $e^{-a_o|k_r|}$, where a_o is the parameterization of the *temporal* T_2 constant as a *spatial frequency* constant. We assume that the first echo occurs at time ESP_o, that subsequent echoes have an echo spacing ESP, and that the echo train length is ETL so that the k_r decay constant is given by $\frac{ESPxETL}{T_2} = a_o k_r^{max}$. Consequently, the smoothly decaying T_2-weighting function is

$$\begin{aligned} e^{-t(k_r)/T_2} &= e^{-ESP_0/T_2} e^{-a_o|k_r|} \\ &= \exp\left(-\frac{ESP_0}{T_2}\right) \exp\left(-\frac{ESPxETL}{T_2}\frac{|k_r|}{k_r^{max}}\right) \end{aligned} \tag{4.15}$$

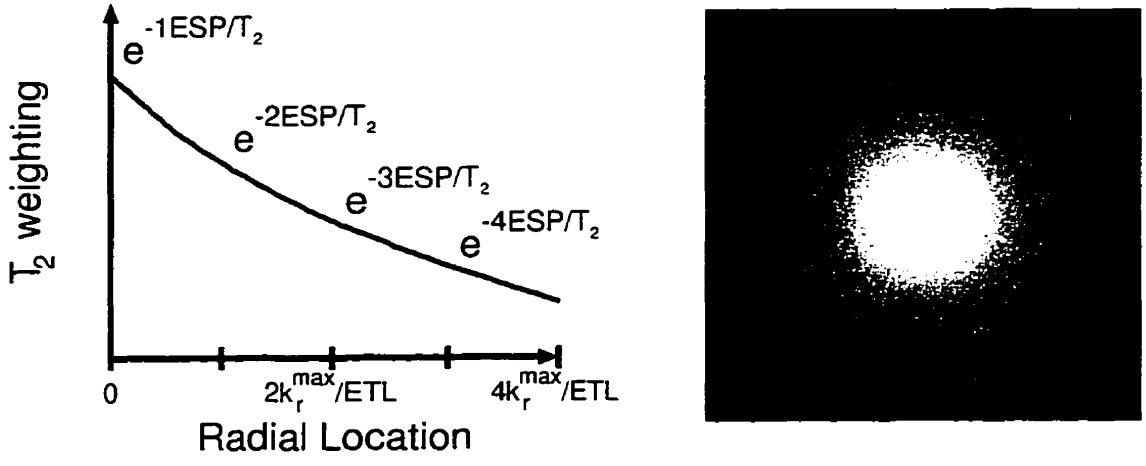

Figure 4.19: CC-MRI T_2-weighted smoothly decaying approach
The T_2-weighting in the radial direction is made pseudo-continuous to eliminate the junction artifacts seen in the banding approach. The 1D representation along the radial direction is shown on the left, while its 2D representation is on the right.

The T_2 impulse response function of the smoothly varying approach is calculated from the Hankel transform of $e^{-t(k_r)/T_2}$ of Eq.(4.15). To get a better intuition, we assume that the weighting is of infinite extent so that the T_2 IRF is given by

$$2\pi \int_0^\infty e^{-ESP_0/T_2}\, e^{-a_o k_r}\, J_o(2\pi r k_r)\, k_r\, dk_r \tag{4.16}$$

which can be rewritten as

$$2\pi\, e^{-ESP_0/T_2} \int_0^\infty \{k_r J_o(2\pi r k_r)\}\, e^{-a_o k_r}\, dk_r \tag{4.17}$$

Now, Eq.(4.17) can be recognized as the Laplace transform of $k_r J_0(2\pi r k_r)$ at the specific "Laplace domain frequency" of a_0, since the Laplace transform of a function $f(\xi)$, say, is given by $\int_0^\infty f(\xi)e^{-s\xi}\,d\xi$. Using [6, p.712 (6.623)] with the appropriate variables, the CC-MRI smooth approach T_2 IRF is of the form

$$\frac{2\pi a_0 \exp(-\mathrm{ESP}_0/T_2)}{(a_0^2+4\pi^2 r^2)^{3/2}} \qquad \text{with } a_0 = \frac{\mathrm{ESPxETL}}{T_2 k_r^{max}} \tag{4.18}$$

The normalized magnitude T_2 IRF (in decibels) is shown in Figure 4.20 assuming an echo spacing ESP=15ms, an echo train length ETL=4 echoes, N_r=128 points per projection, N_a=192 projections, and a T_2 value of 25ms. Note that unlike the above analysis, the actual T_2-weighting function is finite (instead of infinite), and the weighting function is pseudo-continuous (instead of truly continuous) since one measures a finite number of k_r points.

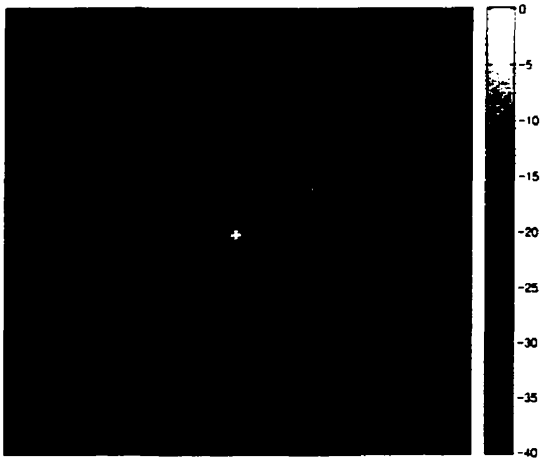

Figure 4.20: CC-MRI T_2 impulse response function for the smooth approach
The normalized T_2 impulse response function is displayed in dBs for an ETL of 4 echoes. N_r=128 points per projection, N_a=192 projections, an ESP of 15ms, and a T_2 value of 25ms. The corresponding linear gray scale colourbar is also shown.

In comparison to the T_2 IRF of Figure 4.17, the smooth approach T_2 IRF is mostly concentrated at the centre and has negligible sidelobes. The noisy synthetic disk phantom of SNR≃100 (shown on the left of Figure 4.21) subjected to this T_2 IRF is free from ring-like artifacts, but experiences some radially isotropic blurring (as shown on the right of Figure 4.21).

Thus, in contrast to PR-MRI, in CC-MRI one must eliminate the junctions (between bands) to prevent any further image artifacts. However, the T_2 IRF does lead to isotropic blurring, which is T_2-dependent: short T_2 species will be blurred more heavily than long T_2 species. This occurs because the T_2-weighting functions of short and long T_2 species are narrow and broad, respectively. This, in turn, means that their T_2 IRFs are broad and narrow, respectively.

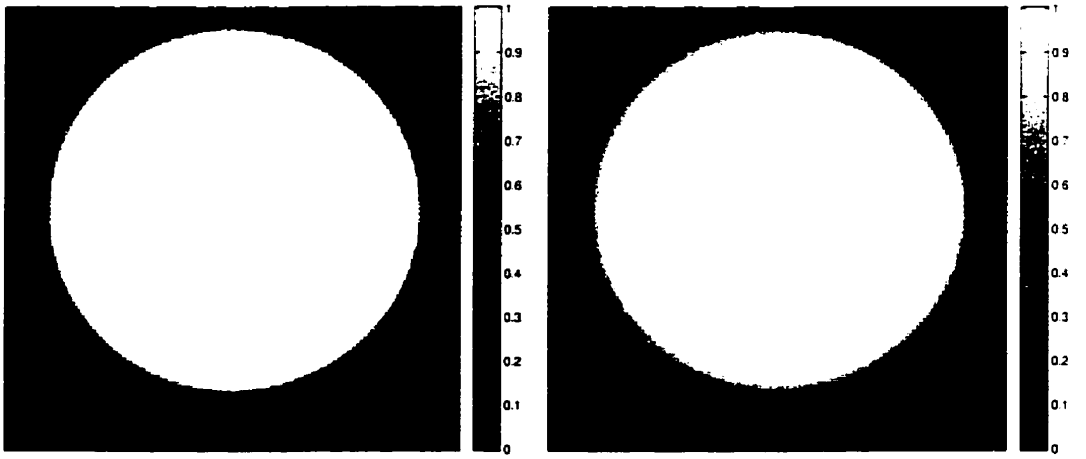

Figure 4.21: CC-MRI image reconstruction effect for the smooth approach
The effect of the CC-MRI smooth approach is shown for a synthetic disk phantom (left) being slightly blurred (right) but not suffering from any ring-like artifacts when subjected to the smooth approach with ESP=15ms, ETL=4 echoes, N_r=128 points per projection, N_a=192 projections, and T_2=25ms. The corresponding linear gray scale colourbars are also shown; the two images are at the same windowing level.

To demonstrate the necessity of the monotonicity requirement, Figures 4.22 and 4.23 show the T_2-weighting and reconstructed phantom image, respectively, of a non-monotonically decaying smoothly varying T_2 modulation for ETL=4 echoes, N_r=128 points per projections, N_a=192 projections, ESP=15ms, and T_2=25ms.

Although the weighting is smooth, the reconstructed image suffers from some edge enhancement whereby the edges of the disk appear brighter than the centre of the disk. This effect becomes more pronounced as the T_2-weighting peak is made further from the centre of k-space. Therefore, if one wishes to acquire the centre of k-space at some time different than the echo spacing ESP and avoid edge enhancement, it is

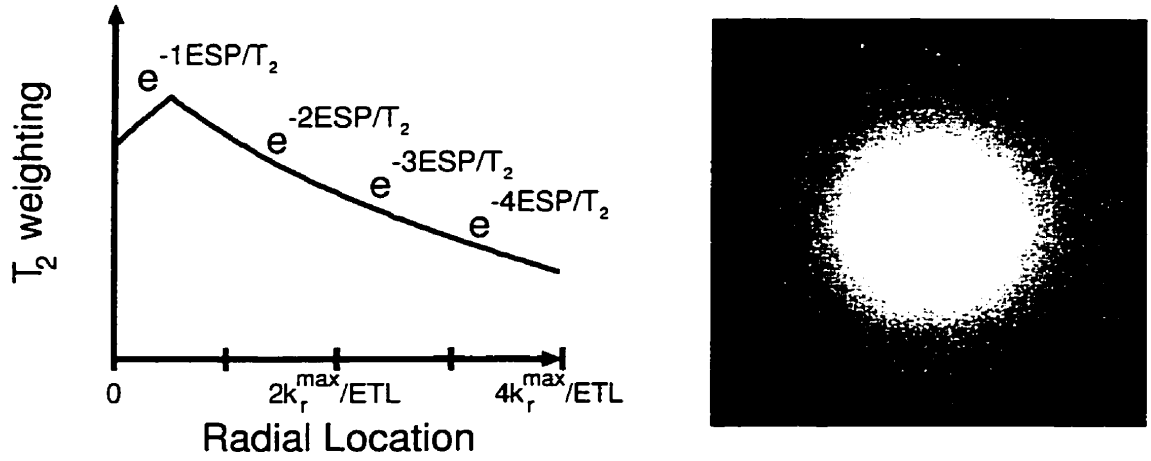

Figure 4.22: CC-MRI T_2-weighted non-monotonic approach
The T_2-weighting in the radial direction is pseudo-continuous to eliminate the junctions, but the weighting function is peaked away *from the centre of* k*-space.*

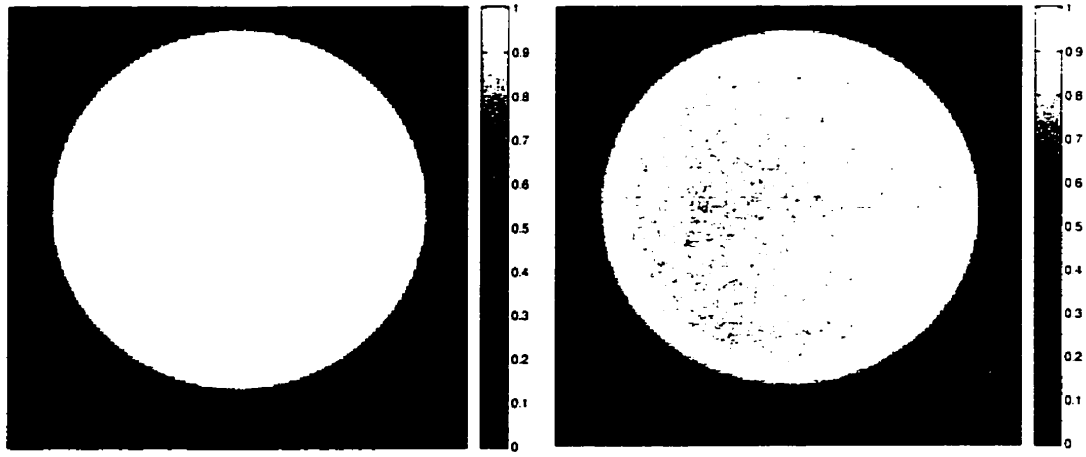

Figure 4.23: CC-MRI image reconstruction effect for the non-monotonic approach
The effect of the CC-MRI non-monotonic approach is shown for a synthetic disk phantom (left) being edge enhanced (right) when subjected to the non-monotonic approach with ESP=15ms, ETL=4 echoes, N_r=128 points per projection, N_a=192 projections, and T_2=25ms. The corresponding linear gray scale colourbars are also shown; the two images are at the same windowing level.

best to either (1) delay the acquisition time of the echo train to ESP_0, or (2) to *not* acquire the first m echoes in the train so that the $(m+1)^{th}$ echo occurs at time ESP_0. In so doing, the CC-MRI T_2-weighting will be monotonically decaying.

In analogy to PR-MRI, it is the time of acquisition of the *centre* of k-space that determines the overall contrast. In CC-MRI, this is represented by the acquisition of the first echo at time ESP_0. However, short T_2 species are apodized more heavily than long T_2 species, which may well affect the effective echo time (TE_{cc}) since the signal intensity fraction of the RARE-mode acquisition is different than that of the conventional SE acquisition.

For the PR-MRI analysis, this consideration was taken care of by assuming a circularly symmetric object whose radial k_r-lines were identical. Subsequent application of the T_2-weighting modified the amplitude of each k_r-line by a scalar. In CC-MRI, however, the T_2-weighting occurs *along* the k_r direction. Consequently, the signal intensity fraction is more difficult to calculate.

Let us consider a uniform, circularly symmetric disk of finite radius c, centred within the FOV. Because of circular symmetry, one can calculate the k_r signal profile using the Hankel transform: from Bracewell [4, p.249], one obtains $2\pi c^2 \frac{J_1(2\pi k_r c)}{2\pi k_r c}$, where J_1 is the first-order Bessel function of the first kind.

The CC-MRI signal intensity fraction $\mathcal{S}_{cc}$ from a RARE-mode acquisition *relative* to a conventional SE acquisition is given by the ratio of their respective integrated k-space signals, namely

$$\begin{aligned}
\mathcal{S}_{cc} &= \frac{\epsilon^{-ESP_0/T_2} \int_0^{2\pi} \int_0^{\infty} 2\pi c^2 \frac{J_1(2\pi k_r c)}{2\pi k_r c} e^{-a_o k_r} k_r \, dk_r dk_\theta}{\epsilon^{-ESP_0/T_2} \int_0^{2\pi} \int_0^{\infty} 2\pi c^2 \frac{J_1(2\pi k_r c)}{2\pi k_r c} k_r \, dk_r dk_\theta} \\
&= \frac{\int_0^{\infty} J_1(2\pi k_r c) e^{-a_o k_r} \, dk_r}{\int_0^{\infty} J_1(2\pi k_r c) \, dk_r}
\end{aligned} \tag{4.19}$$

where we have performed the integral over the k_θ variable (which yields 2π), and have eliminated common terms. Both of these definite integrals can be found from

Gradshteyn [6. p.665 (6.511)] and [6. p.707 (6.611)]. from which

$$\mathcal{S}_{cc} = \frac{\sqrt{a_o^2 + (2\pi c)^2} - a_o}{\sqrt{a_o^2 + (2\pi c)^2}} = 1 - \frac{1}{\sqrt{1 + \left(\frac{2\pi c}{a_o}\right)^2}}$$

$$= 1 - \left[1 + \left(\frac{2\pi c T_2 k_r^{max}}{\text{ESPxETL}}\right)^2\right]^{-1/2} = 1 - \left[1 + \left(\frac{\pi N_r d_p T_2}{2\text{ESPxETL}}\right)^2\right]^{-1/2} \quad (4.20)$$

where we have used $a_o = \frac{\text{ESPxETL}}{T_2 k_r^{max}}$. Moreover, we assume that $k_r^{max} = N_r/2$ so that the FOV in image space is unity. Consequently, the disk diameter $d_p = 2c$ is expressed as a percentage of the FOV.

Just like in the PR-MRI analysis, the CC-MRI signal intensity fraction is independent of ESP_0 since it is *relative* to that echo time. But, an important difference is that $\mathcal{S}_{cc}$ depends not only on ESP, ETL, and T_2, but also on the diameter d_p of the disk and on the number N_r of radial points. Typical CC-MRI $\mathcal{S}_{cc}$ curves are plotted in Figure 4.24 for various N_r, ETL, and d_p values assuming ESP=15ms for T_2 values within the range 1–500ms.

The dependences on T_2, the echo spacing ESP, the echo train length ETL, and the disk size d_p are expected. The N_r dependence may seem somewhat surprising. But, a little thought and the use of Figure 4.25 help to elucidate this dependence. Recall that the FOV is normalized to unity, and that d_p is the disk diameter relative to the FOV. Thus, for fixed FOV and d_p, the non T_2-weighted k-space signal is the same for all N_r values except that one samples out *farther* in k-space for larger N_r values. This is shown schematically as the dotted portion of the signal in Figure 4.25. For a given ESP/ETL combination, then, the T_2-decay occurs over a smaller extent for N_r being small: therefore, more signal is apodized for small N_r compared to large N_r, all else being equal.

It may be instructive to consider a few limiting cases. First, if a_o=0, then the square-root term tends to infinity, and $\mathcal{S}_{cc}$ is unity. This is as expected since the a_o=0 condition is met if (1) there is no T_2-weighting (the conventional SE acquisition), or (2) $T_2 \rightarrow \infty$ which also means that the object is not influenced by any T_2-weighting.

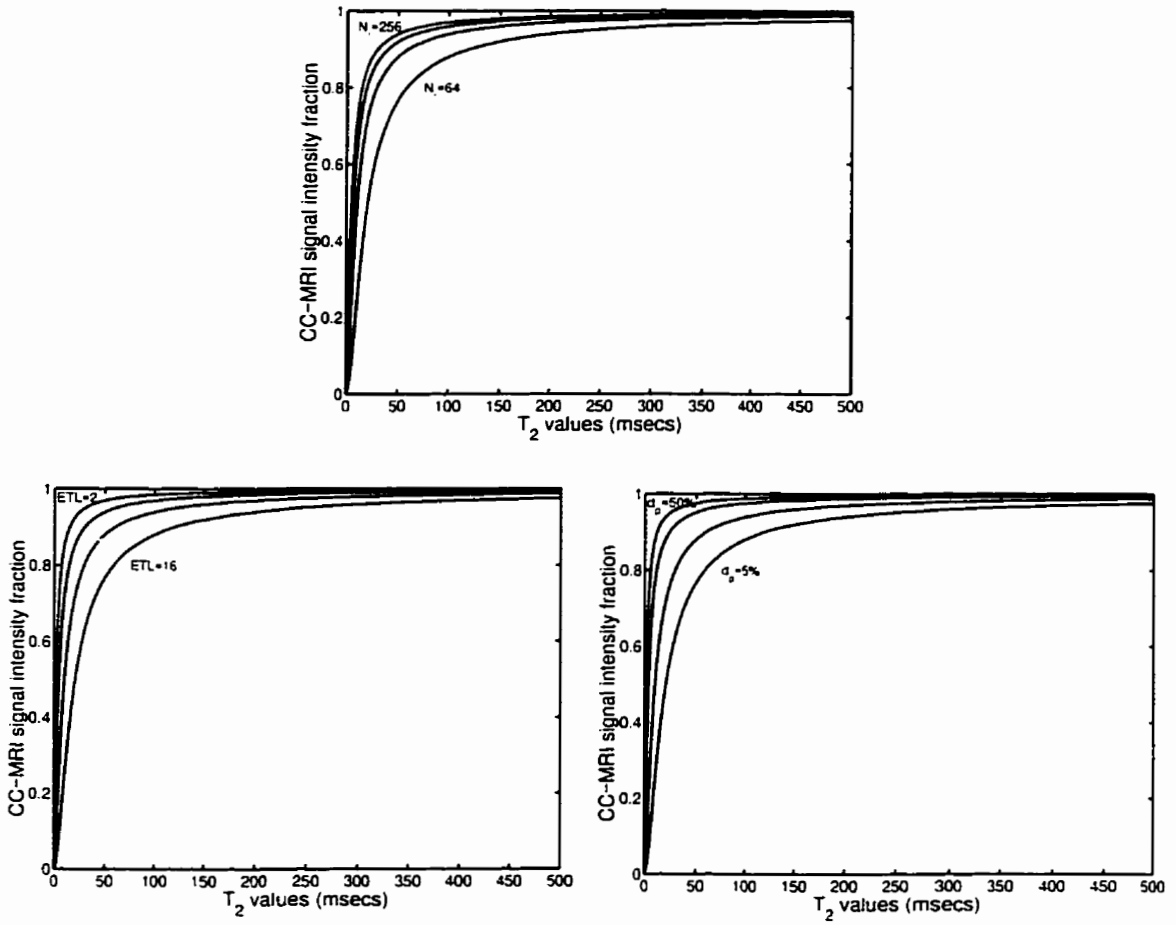

Figure 4.24: CC-MRI signal intensity fraction curves

The CC-MRI signal intensity fraction curves are plotted assuming an echo spacing ESP=15ms. At the top, the S_{cc} curves are for d_p=10% and ETL=8 echoes at various N_r values (64,128,192,256). The bottom left S_{cc} curves are for d_p=10% and N_r=128 radial points at various ETL values (2,4,8,16). Finally, the bottom right S_{cc} curves are for N_r=128 radial points and ETL=8 echoes for various d_p values (5%,10%,25%,50%).

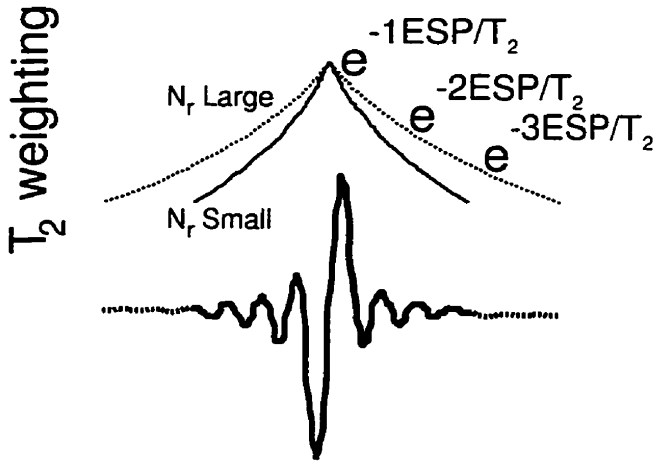

Figure 4.25: CC-MRI signal intensity fraction N_r dependence
The MR k-space signal is shown schematically for a disk of diameter d_p within the FOV. Since the FOVs are the same for small/large N_r values, one must sample the MR signal out farther for large N_r (depicted by the dotted portion of the MR signal). For small N_r values, the T_2-weighting function (solid) is of shorter extent than for large N_r values (dotted), so that a larger fraction of signal is apodized for small N_r.

Second, in the limit of zero diameter disk, *i.e.* $d_p \rightarrow 0$, then the term within the round brackets brackets is zero so that $\mathcal{S}_{cc}$ tends to zero. This is also as expected since there is effectively no object to be imaged.

Third, in the limit of $T_2 \rightarrow 0$, the term within the round brackets is zero and $\mathcal{S}_{cc}$ again tends to zero. This makes intuitive sense since the CC-MRI signal intensity fraction is defined over at least one echo spacing, and a short T_2 with respect to ESPxETL represents a significant signal loss: in this case, a complete signal loss.

Fourth, in the limit of $N_r \rightarrow \infty$, the square-root term tends to infinity and $\mathcal{S}_{cc}$ is unity. This is as expected since this corresponds to $a_o \rightarrow 0$; recall that $a_o = \frac{\text{ESPxETL}}{T_2 k_r^{max}}$, and $k_r^{max} \rightarrow \infty$ as $N_r \rightarrow \infty$.

Numerical verification of Eq.(4.20) was carried out in the following manner. We generated a synthetic phantom consisting of a disk of diameter d_p with respect to the FOV and a large concentric ring, as shown on the left of Figure 4.26. The k-space data (N_r radial points per projection by $\frac{\pi}{2} N_r$ projections within 0–π) were synthesized for the disk and ring, and the appropriate smooth, monotonically decaying CC-MRI T_2-

weighting was determined for the disk. The outer ring was chosen to have an infinite T_2 (so that its S_{cc} is unity for all ESP/ETL/N_r/d_p combinations).

Two composite images were formed, namely the conventional SE CC-MRI image and the RARE-mode image which are depicted on the left and right of Figure 4.26, respectively. The composite k-space data sets were reconstructed using the convolution backprojection algorithm. Since the outer ring had an infinite T_2, its S_{cc} was unity. Thus, all images were normalized to unity with respect to the outer ring.

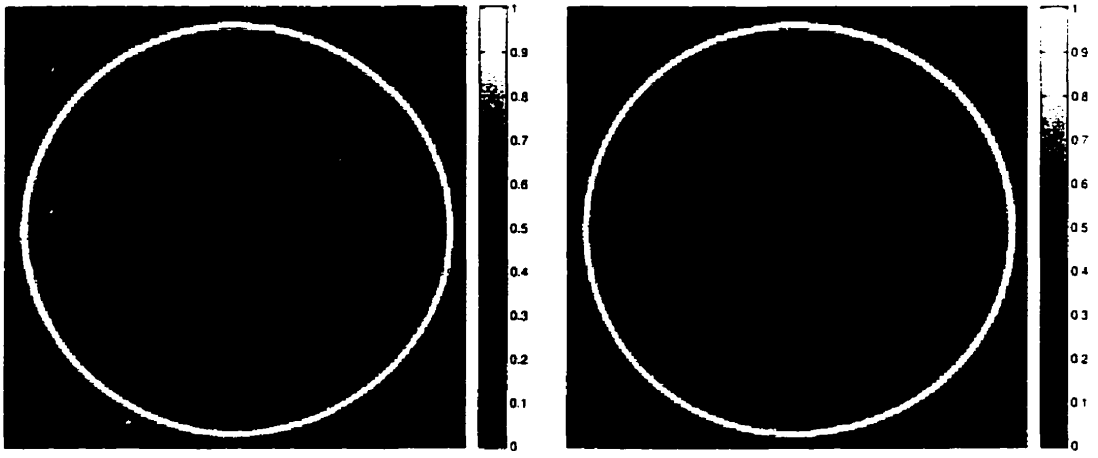

Figure 4.26: CC-MRI signal intensity fraction synthetic phantom images
The synthetic phantom consists of a disk of diameter d_p percent of the FOV (here d_p=25% and T_2=25ms) and centred within the FOV, and a concentric ring with an infinite T_2. The image on the left is the conventional SE CC-MRI image (TE=15ms), whereas the image on the right is the RARE-mode CC-MRI image with ETL=32 echoes, and ESP_0=ESP=15ms. Both images have N_a=192 projections, and N_r=128 points per projection. These images are at the same windowing level.

The CC-MRI signal intensity fraction was calculated from the ratio (at the centre of the disk) of the RARE image to that of the conventional SE image. The signal intensity fractions were found to agree with the theoretical expectations of Eq.(4.20) within ±2% for various ESP (15ms,25ms,40ms), ETL (4,8,16,32), d_p (10%,25%,50%), and N_r (64,96,128) combinations for T_2 values within 1–500ms.

The CC-MRI effective echo time TE_{cc} is given by the expected T_2-weighting at

time ESP_0 multiplied by $\mathcal{S}_{cc}$, namely $e^{-TE_{cc}/T_2} = \mathcal{S}_{cc} e^{-ESP_0/T_2}$, from which

$$\begin{aligned} TE_{cc} &= ESP_0 - T_2 \log \mathcal{S}_{cc} \\ &= ESP_0 - T_2 \log \left\{ 1 - \left[1 + \left(\frac{\pi N_r d_p T_2}{2ESPxETL} \right)^2 \right]^{-1/2} \right\} \end{aligned} \tag{4.21}$$

This is plotted in Figure 4.27 for the various signal intensity fraction curves of Figure 4.24 (ESP=15ms) and setting ESP_0=ESP. Note the increase in effective echo time and the 'hump' region for short T_2 species. This is expected since the $-T_2 \log \mathcal{S}_{cc}$ term involves the function T_2, which ranges from $[0,\infty)$, multiplied with the logarithmic function, which ranges from $(-\infty,0]$ as T_2 goes from zero to infinity. These competing effects result in a 'hump'-like region. Also note the 'flat' region (greater than ESP_0) at large T_2 values. The curves tend towards the asymptotic TE_{cc} limit for a given ESP_0, ESP, ETL, N_r, and d_p combination, as shown below.

Again, let us consider a few limiting cases. First, for a_0=0 we previously found that $\mathcal{S}_{cc}$ tends to unity. Consequently, $\log \mathcal{S}_{cc}$ tends to zero and TE_{cc}=ESP_0 for all T_2 values since TE_{cc} is independent of T_2 in this case. This is as expected since the a_0=0 echo case represents the conventional SE acquisition.

Second, in the limit of $T_2 \to 0$, the Taylor series expansion of the logarithmic term times T_2 reduces to $-2T_2 \log\{\beta T_2\}$, where β includes ESP, ETL, N_r, and d_p. In the limit of T_2 tending to zero, one can show using l'Hospital's rule that this tends to zero and TE_{cc}=ESP_0. Thus, all curves in Figure 4.27 start at TE_{cc}=ESP_0 and increase as a function of T_2.

Third, in the limit of $N_r \to \infty$, we previously found that $\mathcal{S}_{cc}$ tended to unity. Consequently, TE_{cc} tends to ESP_0 for N_r becoming large, as depicted in Figure 4.27.

Fourth, in the limit of $d_p \to 0$, $\mathcal{S}_{cc}$ tends to zero so that the $-T_2 \log\{\}$ term tends to infinity. Consequently, TE_{cc} tends to infinity for d_p tending to zero. This makes intuitive sense since for d_p=0, we expect no signal, and e^{-TE_{cc}/T_2} indeed tends to zero as TE_{cc} tends to infinity.

Fifth, in the limit of $[N_r d_p T_2] \gg$ ESPxETL, the Taylor series expansion of the

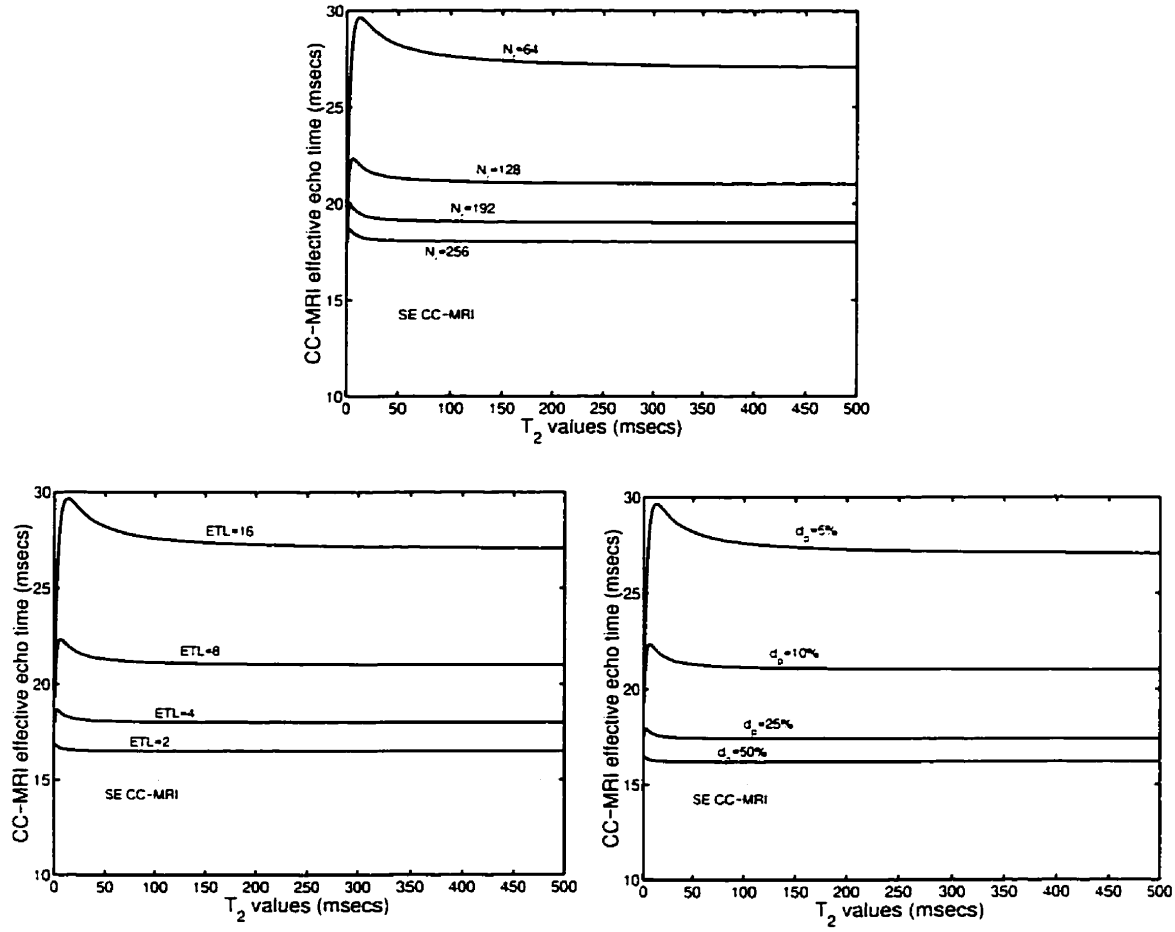

Figure 4.27: CC-MRI effective TE curves

The CC-MRI effective echo time curves are plotted assuming ESP_0=ESP=15ms. At the top, the TE_{cc} curves are for d_p=10% and ETL=8 echoes at various N_r values (64,128,192,256). The bottom left TE_{cc} curves are for d_p=10% and N_r=128 radial points at various ETL values (2,4,8,16). Finally, the bottom right TE_{cc} curves are for N_r=128 radial points and ETL=8 echoes for various d_p values (5%,10%,25%,50%). The conventional SE CC-MRI results are represented by the dashed line.

logarithmic term in Eq.(4.21) reduces to $-\frac{2\text{ESPxETL}}{\pi N_r d_p T_2}$, so that TE_{cc} tends to

$$\text{TE}_{cc} = \text{ESP}_0 + \frac{2\text{ESPxETL}}{\pi N_r d_p} \qquad \text{for } [N_r d_p T_2] \gg \text{ESPxETL} \tag{4.22}$$

This is the asymptotic limit seen in Figure 4.27. One can clearly observe that for large N_r (and large d_p), the CC-MRI effective echo time approaches ESP_0, as expected. The ETL dependence is also clearly obvious. Note the resemblance of the asymptotic echo time limits of PR-MRI and CC-MRI, which are $\text{TE}_{pr}=\text{ESP}_0+\frac{1}{2}\text{ESPxETL}$ and $\text{TE}_{cc}=\text{ESP}_0+\frac{2}{\pi N_r d_p}\text{ESPxETL}$, respectively.

Finally, by knowing the effective echo time TE_{cc}, one can calculate the effective signal intensity from $\epsilon^{-\text{TE}_{cc}/T_2}$. This is plotted in Figure 4.28 for the various effective echo time curves of Figure 4.27 with $\text{ESP}_0=\text{ESP}=15\text{ms}$. Note the small signal intensity for short T_2 species, as expected. The SE CC-MRI (dashed) curve is the conventional SE case and represents the T_2 contrast curve $\epsilon^{-\text{ESP}_0/T_2}$. Also note the clustering of the curves near the conventional SE CC-MRI case. This is somewhat different than the PR-MRI case of Figure 4.15.

The signal intensity fraction and effective echo time analysis for CC-MRI is similar to that for Cartesian RARE-mode acquisitions (see Appendix on page 146) in that the centre of **k**-space is acquired at time ESP_0. Recall that for PR-MRI, though, the centre of **k**-space was acquired at various times throughout the echo train.

Moreover, our CC-MRI signal intensity expectations are consistent with Melki's observation [7] (which pertained to a Cartesian acquisition) that if the object is large with respect to its T_2 impulse response function, namely $d_p T_2 \gg \text{ESPxETL}$, then the **k**-space signal intensity loss is minimal, *i.e.* $\mathcal{S}_{cc}$ is close to unity and $\text{TE}_{cc} \simeq \text{ESP}_0$. In this case, the effective echo time is governed solely by the acquisition of the central **k**-space data, namely ESP_0.

To substantiate the theoretical analysis set forth in the Theory section for both PR-MRI and CC-MRI, we confirmed our expectations via experimental verification. This is described in the next section.

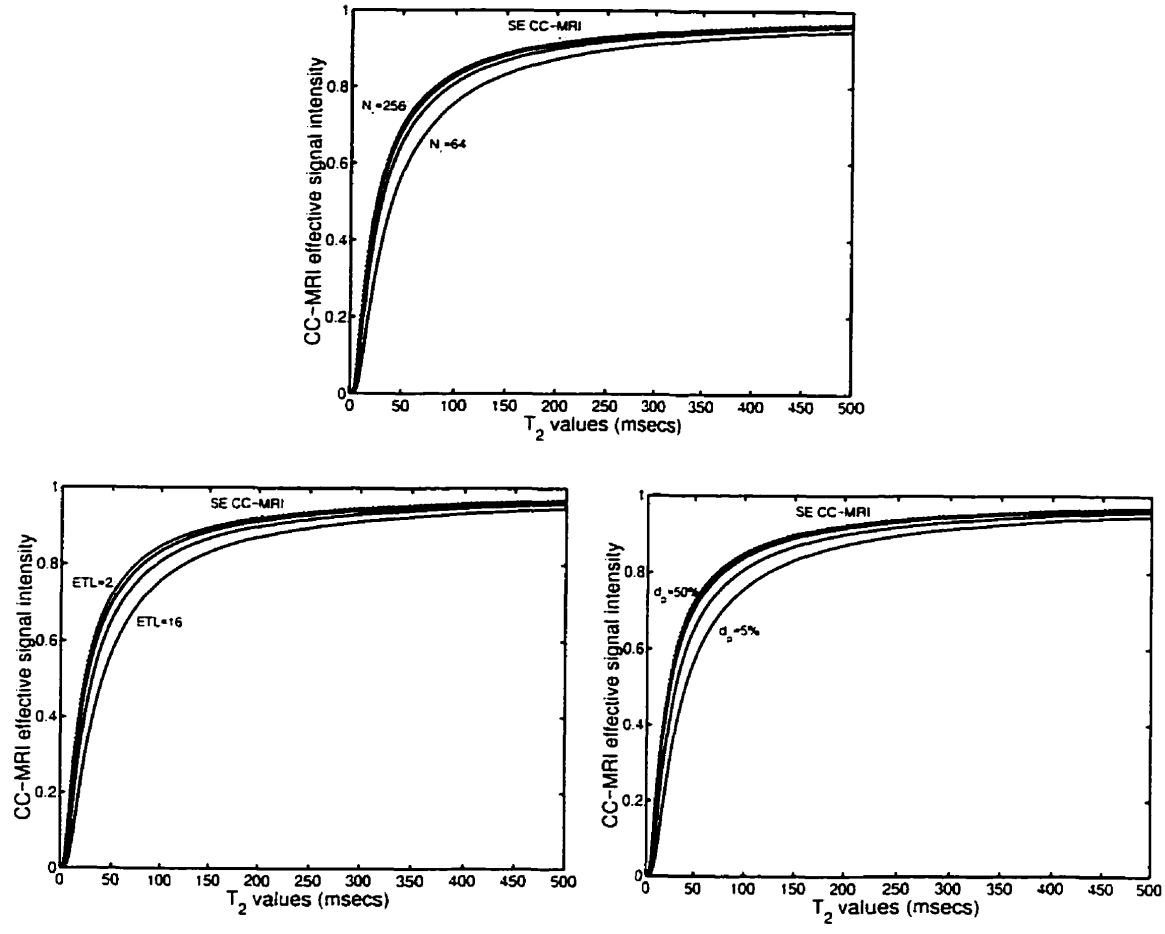

Figure 4.28: CC-MRI effective signal intensity curves

The CC-MRI effective signal intensity curves are plotted assuming $ESP_0=ESP=15ms$. *At the top, the effective signal intensity curves are for* $d_p=10\%$ *and* $ETL=8$ *echoes at various* N_r *values (64,128,192,256). The bottom left effective signal intensity curves are for* $d_p=10\%$ *and* $N_r=128$ *radial points at various ETL values (2,4,8,16). Finally, the bottom right effective signal intensity curves are for* $N_r=128$ *radial points and* $ETL=8$ *echoes for various* d_p *values (5%,10%,25%,50%). The conventional SE CC-MRI results are represented by the dashed line.*

4.3 Results

In the Theory section, we characterized the T_2-weighting functions and their Fourier conjugates, the T_2 impulse response functions, for both PR-MRI and CC-MRI multi-echo acquisitions. We also demonstrated some of the pitfalls of certain T_2 approaches and analyzed the effective echo times TE_{pr} and TE_{cc}. These are important parameters since the effective echo time is a global measure of the T_2 contrast between different T_2 species within the object.

The theoretical expectations were verified experimentally on a 0.5T GE Signa scanner (General Electric Medical Systems, Milwaukee, WI). The phantom consisted of 9 NMR glass tubes (1.0 cm diameter, 15 cm length) closely packed within a 4x4 cm^2 region. Each tube was filled with various concentrations of agarose doped with nickel chloride ($NiCl_2$) to generate T_1 values within the range 250ms-1250ms and T_2 values from 25ms-400ms as shown in Table 3.3 of the Reconstruction Effects chapter.

4.3.1 Projection Reconstruction

For projection reconstruction RARE-mode acquisitions, the one-sided interleaved approach was deemed to be a good compromise in minimizing smearing and star-like artifacts. Therefore, all PR-MRI experimental data used this approach.

The PR-MRI signal intensity fraction curves were verified using the tube phantoms with the following MR parameters: an echo spacing ESP of 15ms, ESP_0=15ms, a repetition time TR of 4000ms, a 5mm slice thickness, an acquisition matrix of 128×288 (namely 128 points per projection with 288 projections within 0-π), one excitation per image (1 NEX), a field of view FOV of 9cm, and a receive bandwidth RBW of ±16kHz. The k-space values were acquired for ETL values of {1,4,8,16,32} echoes using the GE extremity coil. All images were reconstructed (using convolution backprojection) onto a 256x256 image grid and normalized to unity at the brightest pixel. The ETL={1,4,8} echoes reconstructed PR-MRI phantom images are shown in Figure 4.29.

We measured the average signal (plus one standard deviation) within various regions of interest (ROI) of the phantoms. Since all the images were normalized to unity, we then renormalized each ETL image by the expected signal intensity fraction of the 408ms T_2 tube by calculating S_{pr} from Eq.(4.9) with ESP=15ms at the appropriate ETL values. The experimental signal intensity fractions were then calculated by dividing the average ROI signal intensity in the ETL>1 echo images by the average ROI signal intensity in the ETL=1 echo image (which represents the conventional SE PR-MRI acquisition).

In Tables 4.1-4.3, the experimental PR-MRI signal intensity fractions (plus or minus one standard deviation) are given, along with the theoretical expectations calculated from Eq.(4.9) with ESP=15ms at the appropriate ETL and T_2 values. In general, the experimental values agree to within ±5% of the theoretical predictions in the PR-MRI Theory section.

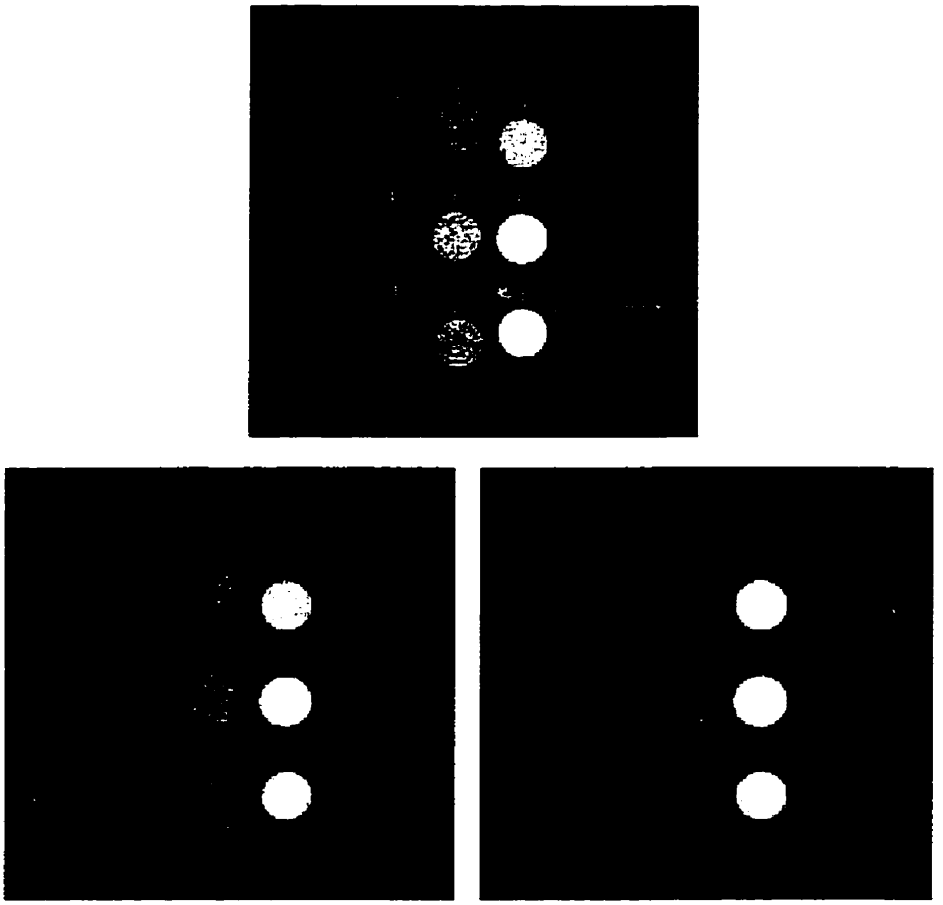

Figure 4.29: PR-MRI T_2 tube phantom images for ETL={1,4,8} echoes
The tube phantoms (1–9) have various T_1 and T_2 values, as given in Table 3.3. The MR parameters appear in the text. On the top is the ETL=1 echo image (TE=15ms) whereas on the bottom left and right appear the ETL=4 echoes and ETL=8 echoes images, respectively, for ESP_0=ESP=15ms. N_r=128 points per projection and N_a=288 projections. All images are at the same windowing level.

Table 4.1: PR-MRI signal intensity fraction verification (Tubes 1-3)

Echo Train Length	T_2	Measured $\mathcal{S}_{pr}$	Theoretical $\mathcal{S}_{pr}$
ETL=4	25ms	0.53 ± 0.04	0.504
	79ms	0.79 ± 0.03	0.769
	179ms	0.89 ± 0.03	0.885
ETL=8	25ms	0.29 ± 0.03	0.275
	79ms	0.59 ± 0.03	0.565
	179ms	0.76 ± 0.03	0.759
ETL=16	25ms	0.15 ± 0.03	0.139
	79ms	0.36 ± 0.02	0.344
	179ms	0.57 ± 0.02	0.573
ETL=32	25ms	0.07 ± 0.03	0.069
	79ms	0.19 ± 0.02	0.180
	179ms	0.36 ± 0.02	0.361

Table 4.2: PR-MRI signal intensity fraction verification (Tubes 4-6)

Echo Train Length	T_2	Measured $\mathcal{S}_{pr}$	Theoretical $\mathcal{S}_{pr}$
ETL=4	27ms	0.55 ± 0.04	0.523
	96ms	0.81 ± 0.04	0.803
	284ms	0.91 ± 0.03	0.925
ETL=8	27ms	0.31 ± 0.03	0.290
	96ms	0.63 ± 0.03	0.617
	284ms	0.81 ± 0.03	0.837
ETL=16	27ms	0.15 ± 0.03	0.147
	96ms	0.40 ± 0.03	0.397
	284ms	0.67 ± 0.03	0.693
ETL=32	27ms	0.07 ± 0.03	0.073
	96ms	0.22 ± 0.02	0.215
	284ms	0.48 ± 0.03	0.495

Table 4.3: PR-MRI signal intensity fraction verification (Tubes 7-9)

Echo Train Length	T_2	Measured S_{pr}	Theoretical S_{pr}
ETL=4	28ms	0.55 ± 0.04	0.532
	107ms	0.83 ± 0.04	0.820
	408ms	0.94 ± 0.04	0.947
ETL=8	28ms	0.31 ± 0.03	0.297
	107ms	0.65 ± 0.04	0.644
	408ms	0.86 ± 0.03	0.882
ETL=16	28ms	0.16 ± 0.03	0.151
	107ms	0.43 ± 0.03	0.427
	408ms	0.75 ± 0.03	0.770
ETL=32	28ms	0.10 ± 0.03	0.075
	107ms	0.24 ± 0.02	0.236
	408ms	0.56 ± 0.03	0.599

4.3.2 Concentric Circles

For concentric circles acquisitions, the smooth monotonically decreasing approach was deemed necessary in minimizing ring-like artifacts and edge enhancement artifacts in the reconstructed image.

The CC-MRI T_2 impulse response function is sensitive to junctions and non-monotonic T_2-weightings. In fact, we discovered that experimentally, for equal phase-encode locations, the first echo was at a lower signal intensity than the second echo. This effect is due to the stimulated echo present in the second (and subsequent) echoes but not in the first echo. This has the effect of violating the decaying monotonicity requirement of the T_2-weighting, and leads to some peculiar reconstruction artifacts, as shown in Figure 4.30. Consequently, in CC-MRI the first echo was not used for ETL$\geq$2, thereby increasing the minimum effective echo time to 2 ESP.

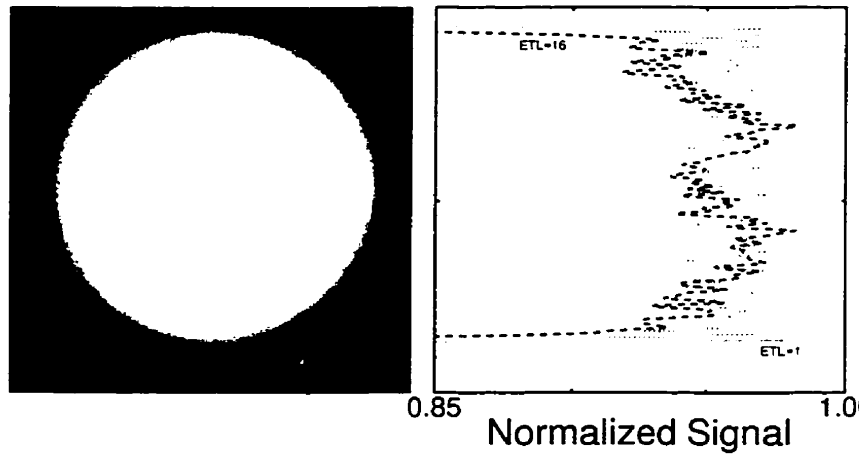

Figure 4.30: Stimulated echo artifact of CC-MRI acquisition
The expected uniform sphere phantom appears non-uniform for ETL=16 echoes if the first echo in the echo train is used (left). On the right, a vertical profile depicts the effect more clearly. The dotted light gray profile represents the conventional SE CC-MRI whereas the darker dashed curve is the profile of the disk on the left. Note the uniformity change near the centre and edges.

The CC-MRI signal intensity fraction curves were verified using the tube phantoms with the following MR parameters: an echo spacing ESP of 20ms, ESP_0=40ms.

a repetition time TR of 4000ms, a 5mm slice thickness, an acquisition matrix of 256×128 (namely 256 projections within 0–π with 128 points per projection), one excitation per image (1 NEX), a field of view FOV of 9cm, and a receive bandwidth RBW of ±16kHz. The k-space values were acquired for ETL values of {1,4,8,16,32} echoes using the GE extremity coil. All images were reconstructed (using convolution backprojection) onto a 256x256 image grid and normalized to unity at the brightest pixel. The ETL={1,4,8} echoes reconstructed CC-MRI phantom images are shown in Figure 4.31.

We measured the average signal (plus one standard deviation) within various regions of interest of the phantoms. Since all the images were normalized to unity, we then renormalized each ETL image by the expected signal intensity fraction of the 408ms T_2 tube by calculating S_{cc} from Eq.(4.20) with N_r=128, d_p=11.1%, and ESP=20ms at the various ETL values. The experimental signal intensity fractions were then calculated by dividing the average ROI signal intensity in the ETL>1 echo images by the average ROI signal intensity in the ETL=1 echo image (which is the conventional SE CC-MRI acquisition).

In Tables 4.4–4.6, the experimental CC-MRI signal intensity fractions (plus or minus one standard deviation) are given, along with the theoretical expectations calculated from Eq.(4.20) with ESP=20ms, N_r=128 points, d_p=11% at the appropriate ETL and T_2 values. In general, the experimental values agree to within experimental error of the theoretical predictions in the CC-MRI Theory section.

However, the experimental results for ETL=32 echoes and T_2 on the order of 25ms–30ms overestimate the theoretical signal intensity fraction by as much as 50%. This is postulated to be an effect due to stimulated echoes being present in the later echoes which produces a net signal increase. Note that the CC-MRI signal intensity fraction analysis of section 4.2.2 did not incorporate the effects of stimulated echoes. Therefore, the experimental results are expected to be slightly greater than the theoretical expectations; this is an observable trend in Tables 4.4–4.6.

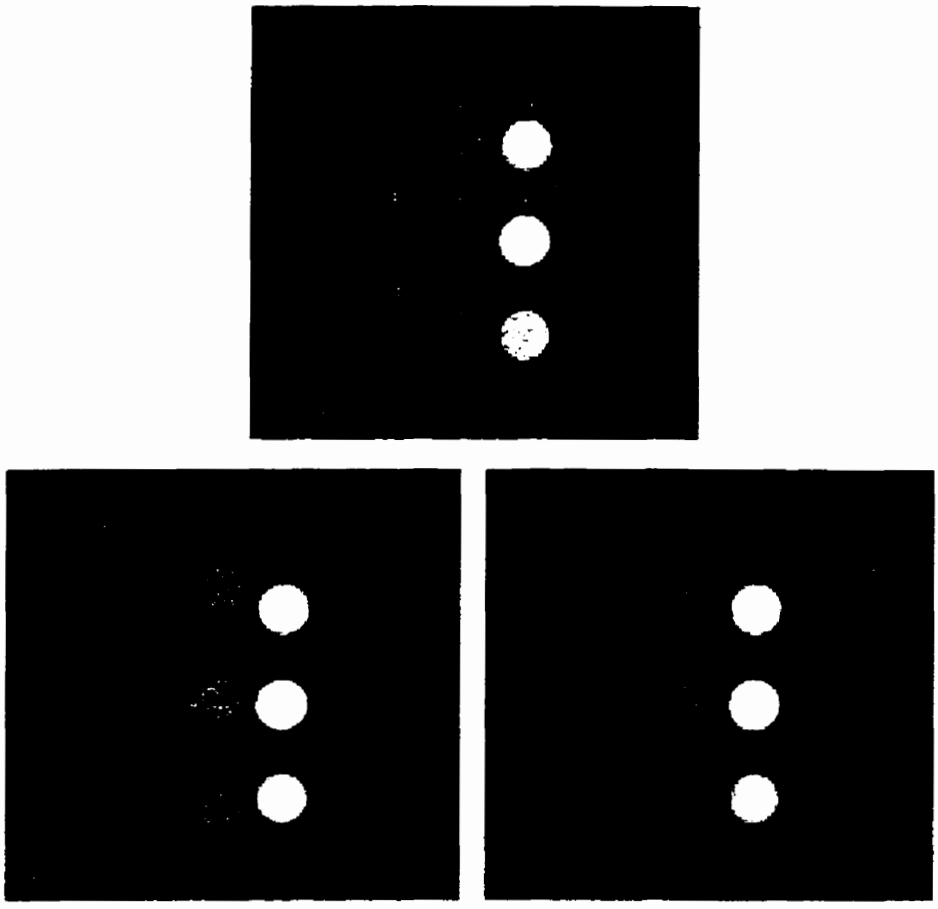

Figure 4.31: CC-MRI T_2 tube phantom images for ETL={1,4,8} echoes
The tube phantoms (1-9) have various T_1 and T_2 values, as given in Table 3.3. The MR parameters appear in the text. On the top is the ETL=1 echo image (TE=40ms) whereas on the bottom left and right appear the ETL=4 echoes and ETL=8 echoes images, respectively, for ESP_0=40ms, ESP=20ms. N_r=128 points per projection and N_a=256 projections. All images are at the same windowing level.

Table 4.4: CC-MRI signal intensity fraction verification (Tubes 1-3)

Echo Train Length	T_2	Measured $\mathcal{S}_{cc}$	Theoretical $\mathcal{S}_{cc}$
ETL=4	25ms	0.87 ± 0.12	0.858
	79ms	0.97 ± 0.05	0.955
	179ms	0.99 ± 0.04	0.980
ETL=8	25ms	0.78 ± 0.12	0.725
	79ms	0.93 ± 0.05	0.910
	179ms	0.96 ± 0.04	0.960
ETL=16	25ms	0.58 ± 0.11	0.503
	79ms	0.85 ± 0.05	0.822
	179ms	0.93 ± 0.04	0.920
ETL=32	25ms	0.41 ± 0.09	0.247
	79ms	0.73 ± 0.05	0.659
	179ms	0.87 ± 0.04	0.842

Table 4.5: CC-MRI signal intensity fraction verification (Tubes 4-6)

Echo Train Length	T_2	Measured $\mathcal{S}_{cc}$	Theoretical $\mathcal{S}_{cc}$
ETL=4	27ms	0.88 ± 0.12	0.869
	96ms	0.97 ± 0.05	0.963
	284ms	0.99 ± 0.05	0.987
ETL=8	27ms	0.78 ± 0.12	0.744
	96ms	0.93 ± 0.05	0.926
	284ms	0.98 ± 0.05	0.975
ETL=16	27ms	0.60 ± 0.10	0.531
	96ms	0.86 ± 0.05	0.852
	284ms	0.96 ± 0.05	0.950
ETL=32	27ms	0.44 ± 0.09	0.272
	96ms	0.77 ± 0.06	0.714
	284ms	0.91 ± 0.05	0.900

Table 4.6: CC-MRI signal intensity fraction verification (Tubes 7-9)

Echo Train Length	T_2	Measured $\mathcal{S}_{cc}$	Theoretical $\mathcal{S}_{cc}$
ETL=4	28ms	0.89 ± 0.12	0.873
	107ms	0.98 ± 0.05	0.967
	408ms	0.99 ± 0.04	0.991
ETL=8	28ms	0.77 ± 0.12	0.752
	107ms	0.93 ± 0.06	0.933
	408ms	0.98 ± 0.04	0.982
ETL=16	28ms	0.57 ± 0.11	0.545
	107ms	0.86 ± 0.06	0.867
	408ms	0.95 ± 0.04	0.965
ETL=32	28ms	0.40 ± 0.09	0.285
	107ms	0.76 ± 0.06	0.741
	408ms	0.92 ± 0.04	0.930

4.3.3 In Vivo Comparison

Finally, we show an *in vivo* example of PR-MRI *vs.* CC-MRI RARE-mode images of an axial slice through the head, and include the Cartesian acquisition for comparison.

The following MR parameters were used for both the PR-MRI and CC-MRI acquisitions: an echo spacing ESP of 20ms, an ESP_0 of 40ms, a repetition time TR of 2000ms, a 5mm slice thickness, an acquisition matrix of 320 projections within $0-\pi$ with 192 points per projection, one excitation per image (1 NEX), a field of view FOV of 24cm, and a receive bandwidth RBW of $\pm$16kHz. The first echo in the echo train was not used in the ETL>1 CC-MRI acquisitions to eliminate the artifact arising from the stimulated echo. The Cartesian acquisition had the same parameters except that the acquisition matrix consisted in 256 frequency encodes by 192 phase encodes.

The k-space values were acquired for ETL values of {1,4,8,16,32} echoes using the GE head coil. All PR-MRI and CC-MRI images were reconstructed using convolution backprojection and normalized to unity at the brightest pixel. The Cartesian images were reconstructed using the fast Fourier transform (FFT) algorithm. The ETL={1,8} echoes reconstructed images are shown in Figure 4.32.

Note that for ETL=1 echo, the PR-MRI and CC-MRI appear very similar, as expected. However, for ETL=8 echoes, one can observe the significant signal intensity decrease in the gray matter (whose T_2~100ms at 0.5T [8]) and white matter (two components with T_2~20ms and T_2~70ms at 0.5T [8]) for the PR-MRI acquisition. In CC-MRI, though, the image appears more blurry, although the white matter and gray matter are still at the same relative brightness level. In all cases, the cerebrospinal fluid is at maximum intensity since it is a long T_2 species (on the order of 2–3 seconds).

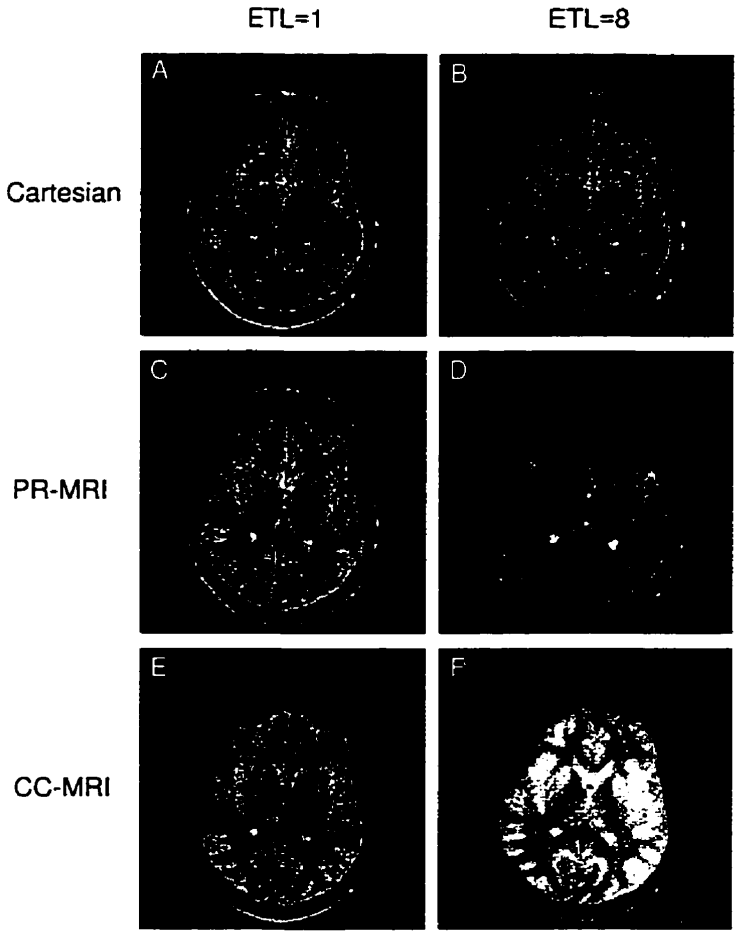

Figure 4.32: Cartesian, PR-MRI, and CC-MRI head images for ETL={1,8} echoes
Axial head images comparison for Cartesian, PR-MRI, and CC-MRI acquisitions. The MR parameters appear in the text. (a) Cartesian conventional SE image with ESP_0=40ms. (b) Cartesian RARE-mode image for ETL=8 echoes, ESP=20ms, and ESP_0=40ms. (c) PR-MRI conventional SE image with ESP_0=40ms. (d) PR-MRI RARE-mode image for ETL=8 echoes, ESP=20ms, and ESP_0=40ms. (e) CC-MRI conventional SE image with ESP_0=40ms. (f) CC-MRI RARE-mode image for ETL=8 echoes, ESP=20ms, and ESP_0=40ms. All images are normalized to unity at the brightest pixel, and appear at the same windowing level.

4.4 Discussion

In MR imaging, the tissue characterization and contrast using T_2-weighted images is of great clinical importance. However, proper T_2-weighted MR images require long acquisition times. Thus, RARE-mode sequences are clinically useful since they speed up data acquisition. Projection reconstruction and concentric circles MRI are easily modifiable k-space trajectories that lend themselves to RARE-mode acquisitions. Herein, we analyzed the ensuing ramifications of such schemes.

For projection reconstruction RARE-mode acquisitions, we showed that a good compromise in suppressing smearing and star-like artifacts is to use the one-sided interleaved T_2-weighted approach. This has the effect of maximizing the amplitude and number of junctions between different echoes. Moreover, no advantage was seen for a smoothly varying weighting. For concentric circles RARE-mode acquisitions, the smooth monotonically decaying approach was essential for minimizing both ring-like and edge enhancement artifacts in the reconstructed image.

The effective echo times were also analyzed. We showed that the signal intensity fraction (and the effective TE) of RARE-mode PR-MRI is highly T_2-dependent for different ESP/ETL combinations. By comparison, the effective TE of RARE-mode CC-MRI is not nearly as sensitive to various ESP/ETL combinations, especially for large objects within the field of view. However, in general, the effective echo time in CC-MRI depends on the echo spacing, the echo train length, the T_2 value, the size of the object, and the size of the acquisition matrix.

Although the theoretical analysis assumed ideal noiseless data, perfect reconstruction, and no stimulated echoes, the experimental projection reconstruction and concentric circles RARE-mode signal intensity fractions agreed quite well with theoretical expectations, although the effect of the stimulated echoes led to slight overestimates.

Stimulated echoes are generated for three or more successive radiofrequency (RF) pulses. Thus, the first echo in the spin echo train consists of the spin echo (*aka* Hahn echo) only, whereas subsequent echoes contain the Hahn echo plus stimulated

echoes. Since RARE-mode CC-MRI acquisitions are sensitive to non-monotonic T_2-weightings. it is best not to use the first echo in the train. unless one can suppress the stimulated echoes or design refocussing RF pulses for a smooth monotonic decay. Still. it may be advantageous to use this first echo as a navigator echo to correct for motion artifacts [9. 10].

In vivo head images showed that the T_2-weighted projection reconstruction and concentric circles MRI images have different T_2 contrasts for equal ESP/ETL parameters. Therefore. contrast characteristics can differ considerably for RARE-mode polar acquisitions depending on the k-space trajectory taken.

Although not shown herein. the motion artifacts using projection reconstruction are greatly reduced in comparison to concentric circles acquisitions. This can be explained by the fact that in PR-MRI. one samples the centre of k-space for each readout whereby phase discontinuities due to motion are averaged. But. in CC-MRI one samples the centre of k-space only once. analogous to Cartesian acquisitions. so that phase discontinuities due to motion are not averaged. Consequently. concentric circles (and Cartesian) RARE-mode acquisitions are more sensitive to motion effects in comparison to projection reconstruction RARE-mode acquisitions.

Our analysis and results indicate that RARE-mode projection reconstruction is a viable method of acquiring fast T_2-weighted images. Although the T_2 contrast is compromised somewhat. and especially so at larger ESP/ETL values. the RARE-mode projection reconstruction sequence appears to be more robust than concentric circles RARE-mode acquisitions in suppressing motion artifacts and minimizing blurring effects in the reconstructed image.

4.5 Appendix

4.5.1 Effective TE for Cartesian RARE-Mode

In this appendix, we derive the analytic expressions of the signal intensity fraction, the effective echo time, and the effective signal intensity for the Cartesian RARE-mode acquisition. It can be directly compared with the concentric circles RARE-mode effective TE analysis.

It is the time of acquisition of the *centre* of k-space that determines the overall contrast. In Cartesian spin-warp (SW-MRI), this is represented by the acquisition of the first echo at time ESP_0. However, short T_2 species are apodized more heavily than long T_2 species, which may well affect the effective echo time (TE_{sw}) since the signal intensity fraction of the RARE-mode acquisition is different than that of the conventional SE acquisition.

Let us consider a uniform rectangular phantom of size w_x by w_y in the x- and y-directions, respectively, and centred within the field of view so that the k-space signal is given by $\frac{1}{\pi^2 k_x k_y}\sin(\pi w_x k_x)\sin(\pi w_y k_y)$. The T_2-weighting is assumed to be smoothly decaying and symmetric in the k_y-direction, in analogy to the smoothly decaying approach in CC-MRI. The SW-MRI signal intensity fraction $\mathcal{S}_{sw}$ from a RARE-mode acquisition *relative* to a conventional SE acquisition is given by the ratio of their respective integrated k-space signals, namely

$$\begin{aligned}\mathcal{S}_{sw} &= \frac{\epsilon^{-\mathrm{ESP}_0/T_2}\int_{-\infty}^{+\infty}\int_{-\infty}^{+\infty}\frac{\sin(\pi w_x k_x)\sin(\pi w_y k_y)}{\pi^2 k_x k_y}\epsilon^{-a_o|k_y|}\,dk_x dk_y}{\epsilon^{-\mathrm{ESP}_0/T_2}\int_{-\infty}^{+\infty}\int_{-\infty}^{+\infty}\frac{\sin(\pi w_x k_x)\sin(\pi w_y k_y)}{\pi^2 k_x k_y}\,dk_x dk_y} \\ &= \frac{\int_0^{\infty}\frac{\sin(\pi w_y k_y)}{k_y}\epsilon^{-a_o k_y}\,dk_y}{\int_0^{\infty}\frac{\sin(\pi w_y k_y)}{k_y}\,dk_y} \qquad (4.23)\end{aligned}$$

where the integration over the k_x variable cancels out, and we have eliminated common terms. Both of these definite integrals are tabulated and can be found from

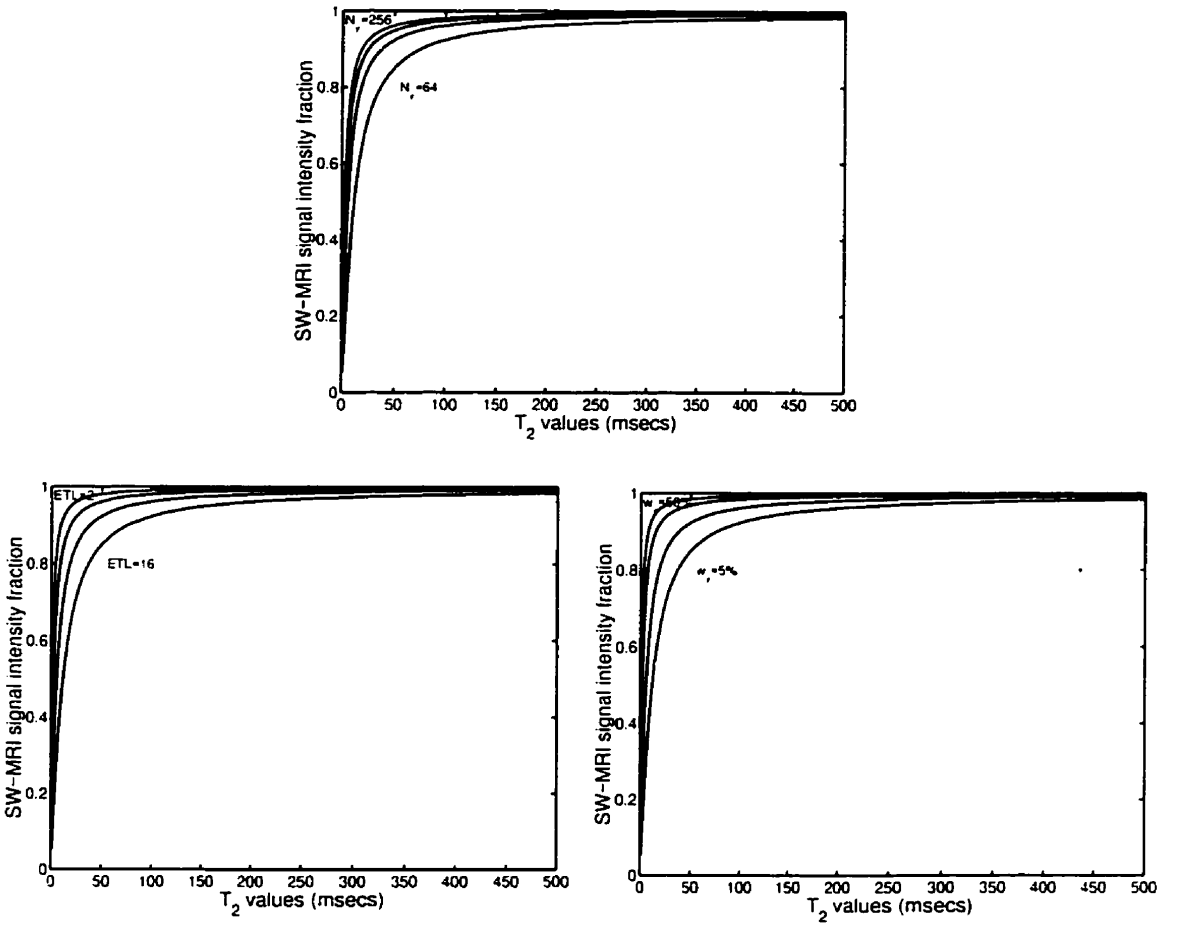

Figure 4.33: SW-MRI signal intensity fraction curves

The SW-MRI signal intensity fraction curves are plotted assuming an echo spacing ESP=15ms. At the top, the S_{sw} curves are for w_y=10% and ETL=8 echoes at various N_y values (64,128,192,256). The bottom left S_{sw} curves are for w_y=10% and N_y=128 phase encodes at various ETL values (2,4,8,16). Finally, the bottom right S_{sw} curves are for N_y=128 phase encodes and ETL=8 echoes for various w_y values (5%,10%,25%,50%).

Gradshteyn [6. p.405 (3.721)] and [6. p.489 (3.941)]. from which

$$\mathcal{S}_{sw} = \frac{2}{\pi}\tan^{-1}\left(\frac{\pi w_y}{a_o}\right) = \frac{2}{\pi}\tan^{-1}\left(\frac{\pi N_y w_y T_2}{2\text{ESPxETL}}\right) \tag{4.24}$$

where we have used $a_o = \dfrac{\text{ESPxETL}}{T_2\, k_y^{max}}$. Moreover. we assume that $k_y^{max}=N_y/2$ so that the FOV in image space is unity. Consequently. w_y is expressed as a percentage of the field of view.

Just like in the CC-MRI analysis. the SW-MRI signal intensity fraction is independent of ESP_0 since it is *relative* to that echo time. An important consequence is that $\mathcal{S}_{sw}$ depends not only on ESP. ETL. and T_2. but also on the width w_y of the rectangle and on the number N_y of phase encodes. Typical SW-MRI $\mathcal{S}_{sw}$ curves are plotted in Figure 4.33 for various N_y. ETL. and w_y values assuming ESP=15ms for T_2 values within the range 1–500ms.

It may be instructive to consider a few limiting cases. First. if a_o=0. then the arctan term tends to $\pi/2$ and $\mathcal{S}_{sw}$ is unity. This is as expected since the a_o=0 condition is met if (1) there is no T_2-weighting (the conventional SE acquisition). or (2) $T_2 \rightarrow \infty$ which also means that the object is not influenced by any T_2-weighting.

Second. in the limit of zero width. *i.e.* $w_y \rightarrow 0$. then the arctan term tends to zero so that $\mathcal{S}_{sw}$ tends to zero. This is also as expected since there is effectively no object to be imaged.

Third. in the limit of $T_2 \rightarrow 0$. the arctan term tends to zero and $\mathcal{S}_{sw}$ again tends to zero. This makes intuitive sense since the SW-MRI signal intensity fraction is defined over at least one echo spacing. and a short T_2 with respect to ESPxETL represents a significant signal loss: in this case. a complete signal loss.

Fourth. in the limit of $N_y \rightarrow \infty$. the arctan term tends to $\pi/2$ and $\mathcal{S}_{sw}$ is unity. This is as expected since this corresponds to $a_o \rightarrow 0$: recall that $a_o = \dfrac{\text{ESPxETL}}{T_2\, k_y^{max}}$. and $k_y^{max} \rightarrow \infty$ as $N_y \rightarrow \infty$.

The SW-MRI effective echo time TE_{sw} is given by the expected T_2-weighting at

time ESP_0 multiplied by $\mathcal{S}_{sw}$, namely $\epsilon^{-TE_{sw}/T_2} = \mathcal{S}_{sw}\epsilon^{-ESP_0/T_2}$, from which

$$\begin{aligned} TE_{sw} &= ESP_0 - T_2 \log \mathcal{S}_{sw} \\ &= ESP_0 - T_2 \log \left\{ \frac{2}{\pi} \tan^{-1} \left(\frac{\pi N_y w_y T_2}{2ESPxETL} \right) \right\} \end{aligned} \tag{4.25}$$

This is plotted in Figure 4.34 for the various signal intensity fraction curves of Figure 4.33 (ESP=15ms) and setting ESP_0=ESP. Note the increase in effective echo time and the 'hump' region for short T_2 species. This is expected since the $-T_2 \log \mathcal{S}_{sw}$ term involves the function T_2, which ranges from $[0,\infty)$, multiplied with the logarithmic function, which ranges from $(-\infty,0]$ as T_2 goes from zero to infinity. These competing effects result in a 'hump'-like region. Also note the 'flat' region (greater than ESP_0) at large T_2 values. The curves tend towards the asymptotic TE_{sw} limit for a given ESP_0, ESP, ETL, N_y, and w_y combination, as shown below.

Again, let us consider a few limiting cases. First, for a_0=0 we previously found that $\mathcal{S}_{sw}$ tends to unity. Consequently, $\log \mathcal{S}_{sw}$ tends to zero and TE_{sw}=ESP_0 for all T_2 values since TE_{sw} is independent of T_2 in this case. This is as expected since the a_0=0 echo case represents the conventional SE acquisition.

Second, in the limit of $T_2 \to 0$, the Taylor series expansion of the logarithmic term times T_2 reduces to $-T_2 \log\{\beta T_2\}$, where β includes ESP, ETL, N_y, and w_y. In the limit of T_2 tending to zero, one can show using l'Hospital's rule that this tends to zero and TE_{sw}=ESP_0. Thus, all curves in Figure 4.34 start at TE_{sw}=ESP_0 and increase as a function of T_2.

Third, in the limit of $N_y \to \infty$, we previously found that $\mathcal{S}_{sw}$ tended to unity. Consequently, TE_{sw} tends to ESP_0 for N_y becoming large, as depicted in Figure 4.34.

Fourth, in the limit of $w_y \to 0$, $\mathcal{S}_{sw}$ tends to zero so that the $-T_2 \log\{\}$ term tends to infinity. Consequently, TE_{sw} tends to infinity for w_y tending to zero. This makes intuitive sense since for w_y=0, we expect no signal, and ϵ^{-TE_{sw}/T_2} indeed tends to zero as TE_{sw} tends to infinity.

Fifth, in the limit of $[N_y w_y T_2] \gg$ ESPxETL, the $-T_2 \log S_{sw}$ term can be solved

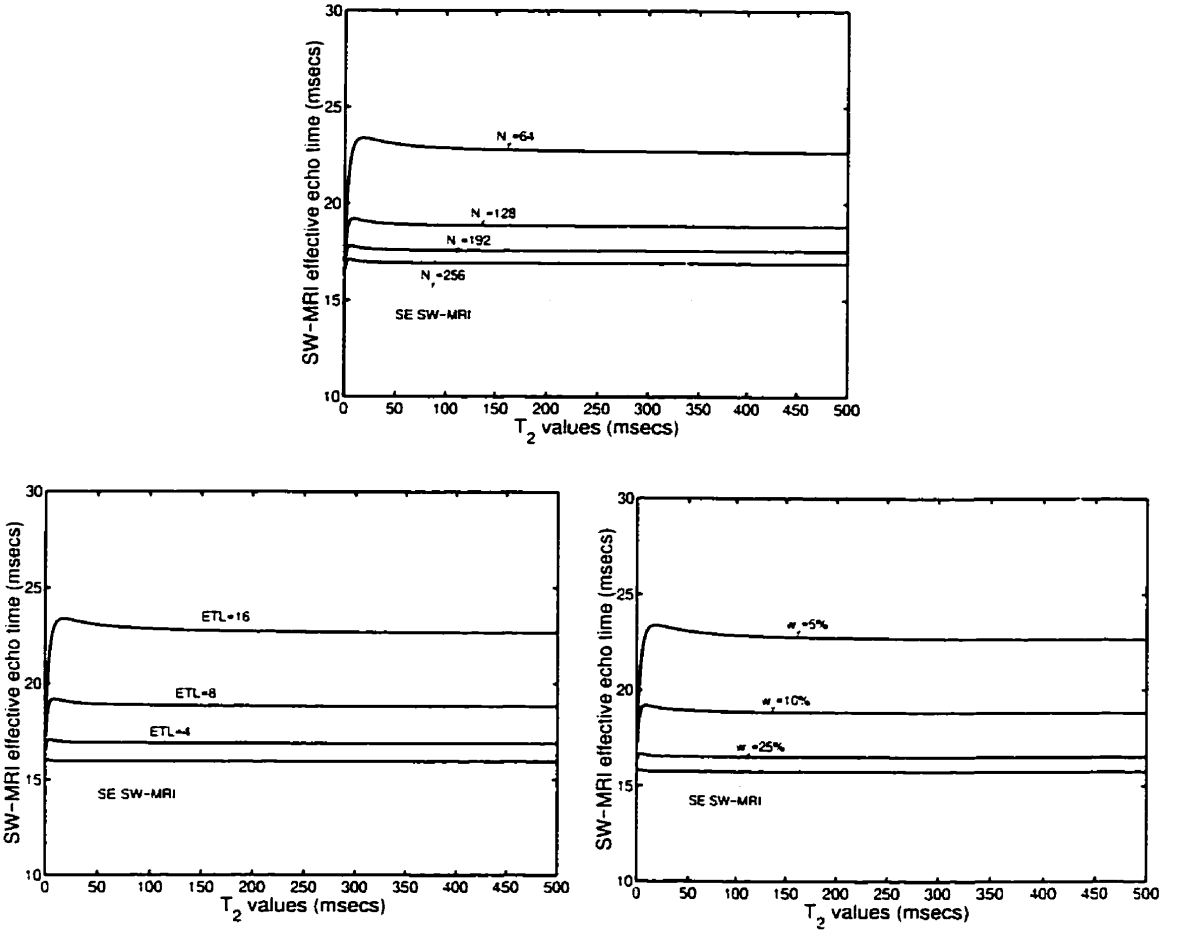

Figure 4.34: SW-MRI effective TE curves

The SW-MRI effective echo time curves are plotted assuming ESP_0=ESP=15ms. At the top, the TE_{sw} curves are for w_y=10% and ETL=8 echoes at various N_y values (64,128,192,256). The bottom left TE_{sw} curves are for w_y=10% and N_y=128 phase encodes at various ETL values (2,4,8,16). Finally, the bottom right TE_{sw} curves are for N_y=128 phase encodes and ETL=8 echoes for various w_y values (5%,10%,25%,50%). The conventional SE SW-MRI results are represented by the dashed line.

using l'Hospital's rule whereby in the limit it tends to $\frac{4\text{ESPxETL}}{\pi^2 N_y w_y}$, so that TE_{sw} is

$$\text{TE}_{sw} = \text{ESP}_0 + \frac{4\text{ESPxETL}}{\pi^2 N_y w_y} \qquad \text{for } [N_y w_y T_2] \gg \text{ESPxETL} \tag{4.26}$$

This is the asymptotic limit seen in Figure 4.34. One can clearly observe that for large N_y (and large w_y), the SW-MRI effective echo time approaches ESP_0, as expected. The ETL dependence is also clearly obvious. Note the resemblance of the asymptotic echo time limits of both SW-MRI and CC-MRI, which are respectively given by $\text{TE}_{sw}=\text{ESP}_0+\frac{4}{\pi^2 N_y w_y}\text{ESPxETL}$, and $\text{TE}_{cc}=\text{ESP}_0+\frac{2}{\pi N_r d_p}\text{ESPxETL}$.

Finally, by knowing the effective echo time TE_{sw}, one can calculate the effective signal intensity from $\epsilon^{-\text{TE}_{sw}/T_2}$. This is plotted in Figure 4.35 for the various effective echo time curves of Figure 4.34 with $\text{ESP}_0=\text{ESP}=15\text{ms}$. Note the small signal intensity for short T_2 species, as expected. The SE SW-MRI (dashed) curve is the conventional SE case and represents the T_2 contrast curve $\epsilon^{-\text{ESP}_0/T_2}$. Also note the clustering of the curves near the conventional SE SW-MRI case. This is reminiscent of the CC-MRI analysis.

The signal intensity fraction and effective echo time analysis for SW-MRI is similar to that for CC-MRI RARE-mode acquisitions in that the centre of k-space is acquired at time ESP_0. Moreover, our SW-MRI signal intensity expectations are consistent with Melki's observation [7] (which pertained to a Cartesian acquisition) that if the object is large with respect to its T_2 impulse response function, namely $w_y T_2 \gg \text{ESPxETL}$, then the k-space signal intensity loss is minimal, *i.e.* $\mathcal{S}_{sw}$ is close to unity and $\text{TE}_{sw}\simeq\text{ESP}_0$. In this case, the effective echo time is governed solely by the acquisition of the central k-space data, namely ESP_0.

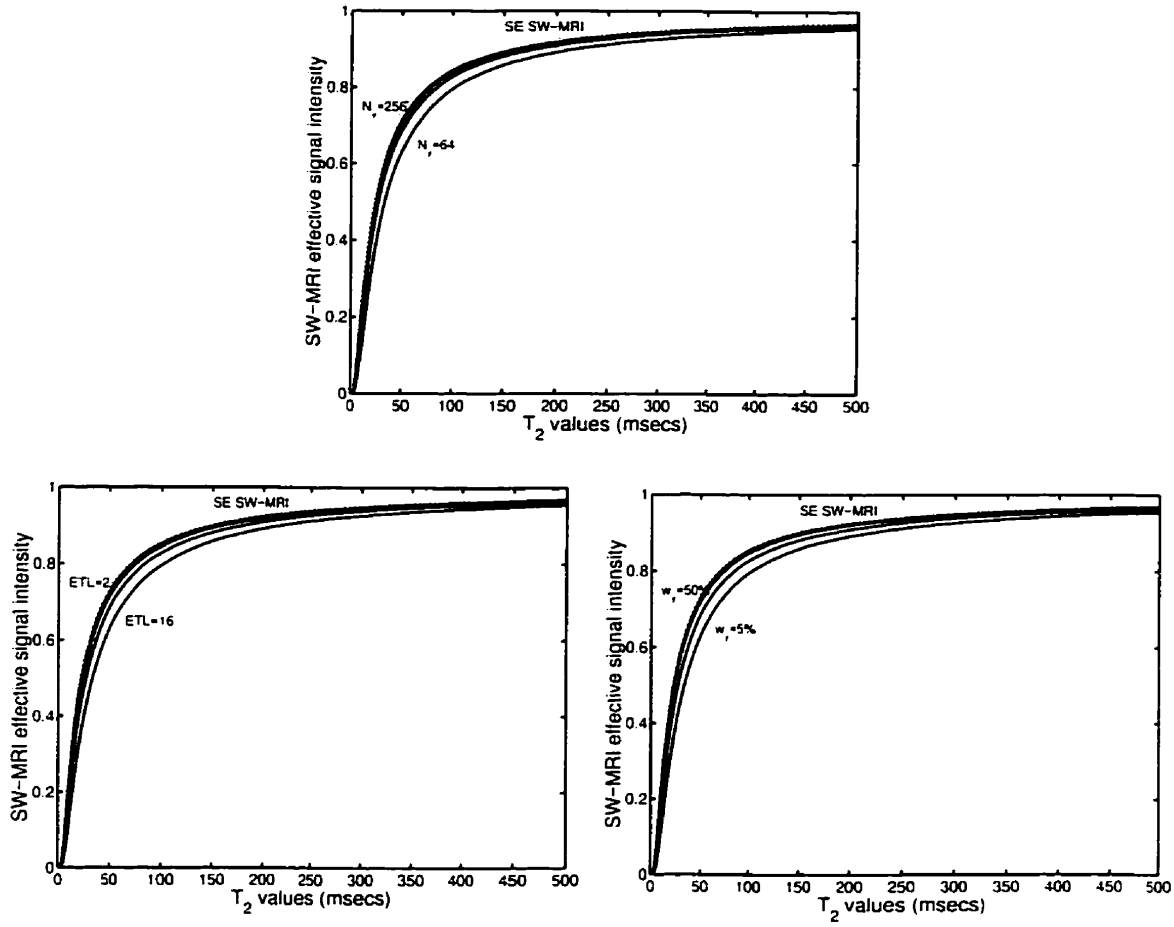

Figure 4.35: SW-MRI effective signal intensity curves

The SW-MRI effective signal intensity curves are plotted assuming ESP_0=ESP=15ms. At the top, the effective signal intensity curves are for w_y=10% and ETL=8 echoes at various N_y values (64,128,192,256). The bottom left effective signal intensity curves are for w_y=10% and N_y=128 phase encodes at various ETL values (2,4,8,16). Finally, the bottom right effective signal intensity curves are for N_y=128 phase encodes and ETL=8 echoes for various w_y values (5%,10%,25%,50%). The conventional SE SW-MRI results are represented by the dashed line.

4.6 References

[1] J. Hennig, A. Nauerth, H. Friedburg, RARE imaging: a fast imaging method for clinical MR. *Magn. Reson. Med.* **3**, 823–833 (1986).

[2] J. Listerud, S. Einstein, E. Outwater, H.Y Kressel, First principles of fast spin echo. *Magn. Reson. Quart.* **8(4)**, 199–244 (1992).

[3] V. Rasche, D. Holz, W. Schepper, Radial turbo spin echo imaging. *Magn. Reson. Med.* **32**, 629–638 (1994).

[4] R.N. Bracewell, "The Fourier Transform and its Applications", McGraw Hill, New York, 1986.

[5] W. Block, J. Pauly, D. Nishimura, RARE spiral T_2-weighted imaging. *Magn. Reson. Med.* **37**, 582–590 (1997).

[6] I.S. Gradshteyn, I.M. Ryzhik, "Table of Integrals, Series, and Products", Academic Press, New York, 1980.

[7] P.S. Melki, F.A. Jolesz, , R.V. Mulkern, Partial RF echo planar imaging with the FAISE method: contrast equivalence with spin echo sequences. *Magn. Reson. Med.* **26**, 342–354 (1992).

[8] H.W. Fischer, P.A. Rinck, Y. Van Haverbeke, R.N. Muller, Nuclear relaxation of human brain gray and white matter: analysis of field dependence and implications for MRI. *Magn. Reson. Med.* **16**, 317–334 (1990).

[9] R.L. Ehman, J.P. Felmlee, Adaptive technique for high-definition MR imaging of moving structures. *Radiology* **173(1)**, 255–263 (1989).

[10] J.P. Felmlee, R.L. Ehman, S.J. Riederer, H.W. Korin, Adaptive motion compensation in MRI: accuracy of motion measurement. *Magn. Reson. Med.* **18**, 207–213 (1991).

Chapter 5

Conclusions and Discussion

Magnetic resonance imaging is a powerful imaging modality in that the tissue can be characterized according to various contrast mechanisms, most notably T_2-weighted contrast. The T_2-weighted images are very useful clinically, but the major disadvantage is that these high-quality images often require long imaging times.

The Cartesian RARE-mode acquisition sequence proposed by Hennig [1] retains the soft-tissue contrast and signal-to-noise ratio (SNR) of T_2-weighted images, but at a reduced acquisition time in comparison to conventional T_2-weighted images. Moreover, non-Cartesian sampling schemes offer further advantages in motion and flow artifact suppression, and efficient use of gradients.

In this treatise, the viability of fast T_2-weighted polar k-space sampling acquisitions was assessed and compared for projection reconstruction (PR-MRI) and concentric circles (CC-MRI). Both of these sequences are easily modifiable k-space trajectories that lend themselves to RARE-mode acquisitions. We therefore analyzed the fundamental aspects of polar k-space acquisitions, including sampling and image reconstruction effects such as aliasing, image resolution and SNR, and investigated the T_2-weighted contrast effects when imaging in RARE-mode.

Herein, a summary of the salient conclusions of chapters 2–4, namely the Sampling Effects, Reconstruction Effects, and T_2 Modulation Effects chapters is given. Possible future directions of rapid T_2-weighted MR imaging are also presented.

5.1 Sampling Effects

In the Sampling Effects chapter, the Fourier aliasing effects of uniform polar sampling (*i.e.* equally-spaced radial and azimuthal samples) were analyzed and explained. The primary focus rested on the radial effects of polar k-space sampling which were treated from a two-dimensional (2D) formalism.

The principal point spread function (PSF) of polar k-space sampling schemes was analyzed by assuming equally-spaced *ring* samples. We followed Bracewell and Thompson's [2] formalism and decomposed the PSF into its main lobe (whose behaviour is jinc-like), and a series of asymmetric ringlobes peaked near $j/\Delta k_r$ (whose amplitudes decay as j increases), where j is the ringlobe number and Δk_r is the radial sample spacing in k-space.

Since the first ringlobe occurs at a *radius* of $1/\Delta k_r$, the object's extent must be space-limited to within a *diameter* of $1/\Delta k_r$, in analogy to the Cartesian Nyquist sampling criterion. However, due to sampling on a finite polar grid, the ringlobes are asymmetric, oscillatory, non-periodic, and extend to the origin. Thus, when we consider the full 2D sampling effects, aliasing artifacts occur even if the radial Nyquist criterion is satisfied. This aliasing leads to a small non-zero background signal within the baseband and affects the overall intensity pattern of the object. The deviation from the true intensity increases as the object size increases relative to the FOV.

The full two-dimensional PSF includes the main lobe and the ringlobes, the latter leading to aliasing effects. However, unlike Cartesian sampling, the aliasing is not merely just a fold-over at the edges of the image, but a fold-over at the FOV radius, which represents a continuous folding. Moreover, unlike Cartesian sampling, the ringlobes are asymmetric and not purely periodic, which leads to a more complicated Gibb's-like ringing artifact and perturbs the expected signal intensity pattern.

The concepts of aliasing and leakage are well understood for Cartesian sampling. However, for polar sampling (and perhaps most if not all non-Cartesian sampling acquisitions), this distinction is no longer clearly obvious. Even if we sample with

δ-rings out to infinity, it is not apparent that its 2D PSF is itself a series of concentric δ-rings. Recall that in Cartesian sampling, the concept of aliasing is properly defined because the FT of an infinite series of δ-functions is itself a series of δ-functions. Leakage effects are easily explained and are due to truncation effects, *i.e.* due to the fact that we've sampled only over a finite extent. For polar sampling, however, these two concepts are not readily separable. Consequently, the 2D PSF of polar sampling encompasses a "mixing" of both aliasing and leakage effects, as defined for Cartesian acquisitions. Here, we've opted to call this simply aliasing.

But, the reader is cautioned that, herein, the term aliasing is used in the broadest sense of the word: any high frequency (or spatial) component going under an assumed low frequency (or spatial) component. In Cartesian sampling, leakage (and ringing) effects are remedied via the application of suitable filters (*e.g.* the Hamming window) prior to IFT. However, for polar sampling, these same filters did not correct the observed non-uniform intensity pattern of the reconstructed disk objects. Therefore, we attribute the effect as an aliasing phenomenon, where aliasing is now used in its most general and all-encompassing meaning.

In Cartesian sampling, the effective FOV is a *square* region of full-width $1/\Delta k_r$ for a sample spacing of Δk_r in both the k_x- and k_y-directions. In polar sampling, though, it is a *circular* region of diameter $1/\Delta k_r$. This means that the polar FOV area is about 78.5% that of the Cartesian FOV for commensurate sample spacing and image pixel size. For comparable fields of view, the number of polar samples may have to be increased. On the other hand, certain polar sampling schemes (*e.g.* spiral acquisitions) allow more efficient coverage of **k**-space for a fixed gradient capability which may offset the increase in samples required.

Although the 2D polar sampling PSF leads to some subtle aliasing effects and/or artifacts, these effects can be suppressed depending on the choice of reconstruction algorithm one uses. This was the subject of the subsequent chapter in this treatise.

5.2 Reconstruction Effects

In the Reconstruction Effects chapter, the resolution, signal-to-noise ratio and aliasing characteristics of the gridding (GRD) and convolution backprojection (CBP) reconstruction algorithms were compared and contrasted for polar k-space sampling.

Gridding is primarily a Fourier domain algorithm while CBP is an image domain technique. Still, both of these algorithms perform *identically* in terms of image SNR and resolution provided that these two image characteristics are considered together. In their most basic implementations, where the sampling density correction is based on ramp filters, GRD maximizes resolution at the expense of SNR, while CBP sacrifices resolution to increase the SNR.

More generally, for a given choice of k-space trajectory and sample locations, the SNR and resolution are intimately related: the increase of one of these characteristics engenders a commensurate decrease in the other. The choice of reconstruction algorithm merely opts for a different balance between these two effects.

The GRD algorithm offers the advantage of direct manipulation of the k-space data via multiplication. This gives the user flexibility in trading off resolution for SNR (and vice versa) for a given acquisition. Moreover, due to its generality, GRD allows for the possibility of non-equidistant azimuthal polar sampling whereby one can maximize resolution and SNR *simultaneously*. This is achieved if the sampling density in k-space is uniform.

One important difference between GRD and CBP is their different PSFs which lead to different aliasing behaviour. The polar PSF using GRD includes the main lobe and the ringlobes, as given in the Sampling Effects chapter, where the main lobe describes the blurring effect of finite sampling, and the ringlobes are a measure of the expected aliasing. The gridding PSF retains the inherent 2D polar PSF characteristics. In fact, the gridding algorithm is nothing more than a computationally efficient discrete Fourier transform for non-Cartesian data. Consequently, the full 2D sampling effects are not altered by gridding.

By comparison, the convolution backprojection PSF eliminates the ringlobes altogether since the radial effects of the PSF are calculated from a 1D Fourier inversion instead of a 2D Fourier inversion. The 1D projections are then convolved with the CBP convolution function to compensate for the variable sampling density in **k**-space. Since this process is applied to the baseband projections only, there are no ringlobes arising from the replicates. Thus, provided that the radial sampling satisfies the Nyquist criterion, *i.e.* that the object's radial extent is within a circular FOV of diameter $1/\Delta k_r$, the aliasing using CBP will be minimal.

Having characterized the fundamental sampling and reconstruction effects of polar sampling, we then analyzed the T_2 modulation and resultant T_2-weighted contrast of polar **k**-space sampling schemes acquired in RARE-mode.

5.3 T_2 Modulation Effects

In the T_2 Modulation Effects chapter, the amplitude modulation effects of RARE-mode polar sampling were analyzed and compared for projection reconstruction and concentric circles acquisitions. The T_2-weighting and T_2 impulse response function formalism was presented. More importantly, the effective echo times of each sequence were derived, allowing one to characterize the effective T_2-weighted contrast curves.

For projection reconstruction RARE-mode MRI acquisitions, a good compromise in suppressing both smearing and star-like artifacts is to use the one-sided interleaved T_2-weighted approach. Conversely, for concentric circles RARE-mode acquisitions, the smooth monotonically decaying approach was deemed to be essential in minimizing both ring-like and edge enhancement artifacts in the reconstructed image.

The signal intensity fraction and the effective echo time of RARE-mode PR-MRI were found to be highly T_2-dependent for different echo spacing (ESP) and echo train length (ETL) combinations. By comparison, the effective echo time of RARE-mode CC-MRI was found not to be nearly as sensitive to various ESP/ETL combinations, especially for large objects within the field of view. In general, the effective echo time in RARE-mode PR-MRI depends on ESP, ETL, and T_2, while in CC-MRI it depends on ESP, ETL, T_2, the object size, and the acquisition matrix size.

In vivo head images showed that the RARE-mode projection reconstruction and concentric circles MRI images have different T_2 contrasts for equal ESP and ETL parameters. Therefore, contrast characteristics can differ considerably for RARE-mode polar acquisitions depending on the k-space trajectory taken.

Moreover, motion artifacts using projection reconstruction are greatly reduced in comparison to concentric circles acquisitions since in PR-MRI one samples the centre of k-space repeatedly. By comparison, in CC-MRI one samples the centre of k-space only at the beginning of the acquisition. The PR-MRI sequence has the advantage of averaging out the effects of motion near the centre of k-space. Since it is the low spatial frequencies which define the overall characteristics of the image, the motion

averaging leads to slight image blurring but minimal ghosting artifacts. In CC-MRI, though, motion effects lead to significant smearing, blurring, and ghosting artifacts in the reconstructed image.

Our analysis and results indicate that RARE-mode PR-MRI is a viable method of acquiring fast T_2-weighted images. Although the T_2 contrast is compromised somewhat, and especially so at larger ESP/ETL values, the RARE-mode projection reconstruction MRI sequence appears to be more robust than concentric circles RARE-mode acquisitions in minimizing blurring and/or smearing effects in the reconstructed MR image. Moreover, PR-MRI acquisition schemes are less sensitive to motion and flow effects and artifacts.

5.4 Future Perspectives

Our hypothesis was that polar sampling schemes, and more specifically RARE-mode polar sampling, are a viable alternative to acquiring high contrast, high SNR, proper T_2-weighted MR images. Indeed, we demonstrated this theoretically and substantiated the analytical claims with experimental verification.

The time savings of acquiring T_2-weighted images can be increased further by using longer echo train lengths. However, one can appreciate that for large ETL the image blurring and/or smearing may become severe, or the T_2-weighted contrast may be significantly compromised. But, what if one were somehow able to "deconvolve" the effect of the various T_2 impulse response functions from the resultant image ?

In general, deconvolution is a difficult process. But, recall that the T_2-weighting is multiplicative in k-space. This suggests that the solution to this problem may be more easily manageable in k-space (*i.e.* a demodulation) than in image space.

As in the T_2 Modulation Effects chapter, we assume that the object is composed of N_s different T_2 species. Therefore, the T_2-weighted RARE-mode image, which may be collected with *any* desired k-space trajectory, is given by

$$M_{rare}(\mathbf{k}) = \sum_{j=1}^{N_s} e^{-t(\mathbf{k})/T_{2,j}} M_o^j(\mathbf{k}) \tag{5.1}$$

where $M_o^j(\mathbf{k})$ and $T_{2,j}$ are the spin-density k-space magnetization and T_2 value, respectively, of the j^{th} T_2 species, and $t(\mathbf{k})$ reflects the acquisition trajectory used. Since there are N_s different T_2 species to be demodulated, we assume that N_s different RARE-mode data sets are acquired at the *same* spatial frequency locations, but with *different* T_2-weighting functions:

$$\begin{aligned} M_{rare,1}(\mathbf{k}) &= \sum_{j=1}^{N_s} e^{-t_1(\mathbf{k})/T_{2,j}} M_o^j(\mathbf{k}) \\ &\vdots \\ M_{rare,N_s}(\mathbf{k}) &= \sum_{j=1}^{N_s} e^{-t_{N_s}(\mathbf{k})/T_{2,j}} M_o^j(\mathbf{k}) \end{aligned} \tag{5.2}$$

This can be written in matrix notation, namely

$$\begin{pmatrix} M_{rare,1}(\mathbf{k}) \\ \vdots \\ M_{rare,N_s}(\mathbf{k}) \end{pmatrix} = \begin{pmatrix} \epsilon^{-t_1(\mathbf{k})/T_{2,1}} & \cdots & \epsilon^{-t_1(\mathbf{k})/T_{2,N_s}} \\ \vdots & \ddots & \vdots \\ \epsilon^{-t_{N_s}(\mathbf{k})/T_{2,1}} & \cdots & \epsilon^{-t_{N_s}(\mathbf{k})/T_{2,N_s}} \end{pmatrix} \bullet \begin{pmatrix} M_o^1(\mathbf{k}) \\ \vdots \\ M_o^{N_s}(\mathbf{k}) \end{pmatrix}$$

$$\widetilde{\mathbf{M}}_{rare}(\mathbf{k}) = \widetilde{\mathbf{E}}(\mathbf{k})\,\widetilde{\mathbf{M}}_o(\mathbf{k}) \tag{5.3}$$

where the definition of the column vectors $\widetilde{\mathbf{M}}_{rare}(\mathbf{k})$ and $\widetilde{\mathbf{M}}_o(\mathbf{k})$ are obvious, and the ij^{th} term of $\widetilde{\mathbf{E}}(\mathbf{k})$ is given by $\epsilon^{-t_i(\mathbf{k})/T_{2,j}}$. The inversion of Eq.(5.3) leads to

$$\begin{aligned} \widetilde{\mathbf{E}}^{-1}(\mathbf{k})\,\widetilde{\mathbf{E}}(\mathbf{k})\,\widetilde{\mathbf{M}}_o(\mathbf{k}) &= \widetilde{\mathbf{E}}^{-1}(\mathbf{k})\,\widetilde{\mathbf{M}}_{rare}(\mathbf{k}). \qquad \text{so that} \\ \widetilde{\mathbf{M}}_o(\mathbf{k}) &= \widetilde{\mathbf{E}}^{-1}(\mathbf{k})\,\widetilde{\mathbf{M}}_{rare}(\mathbf{k}) \end{aligned} \tag{5.4}$$

where $\widetilde{\mathbf{E}}^{-1}(\mathbf{k})$ is the matrix inverse of $\widetilde{\mathbf{E}}(\mathbf{k})$. Note that this inversion process must be carried out for each acquired k-space sample location.

Also note that we have effectively isolated the N_s different spin-density k-space magnetization T_2 species, $M_0^j(\mathbf{k})$. Their inverse Fourier transform yields N_s different $I_o^j(\mathbf{r})$ images, *i.e.* the images of each T_2 species *without* any T_2-weighting. The resultant MR image is simply the superposition of these individual T_2 species images.

In theory, the resultant image is free from any T_2 modulation effects. It is surmised that the signal-to-noise ratio will be different (most probably lower) in comparison to a conventional SE acquisition. This is because the T_2-weighting correction is calculated from lower SNR k-data that are apodized by the T_2-weighting. But, some of the loss in SNR may be replenished by the fact that one uses N_s multiple sets of acquisitions.

The difficulty lies in determining the terms of the $\widetilde{\mathbf{E}}(\mathbf{k})$ matrix. The $t(\mathbf{k})$ is easily characterized from the trajectory of acquisition, but one also needs to determine the N_s different T_2 values. One could assume typical T_2 values for, say, short, medium, and long T_2 species. Otherwise, it may be advantageous to acquire a rapid, low-resolution multi-echo scout image to approximately determine the N_s different T_2 values in the imaged object.

More generally, it might be possible to solve for $\widetilde{\mathbf{M}}_o(\mathbf{k})$ using a minimized least-squares type of solution: since there are P sample locations and N_s different data

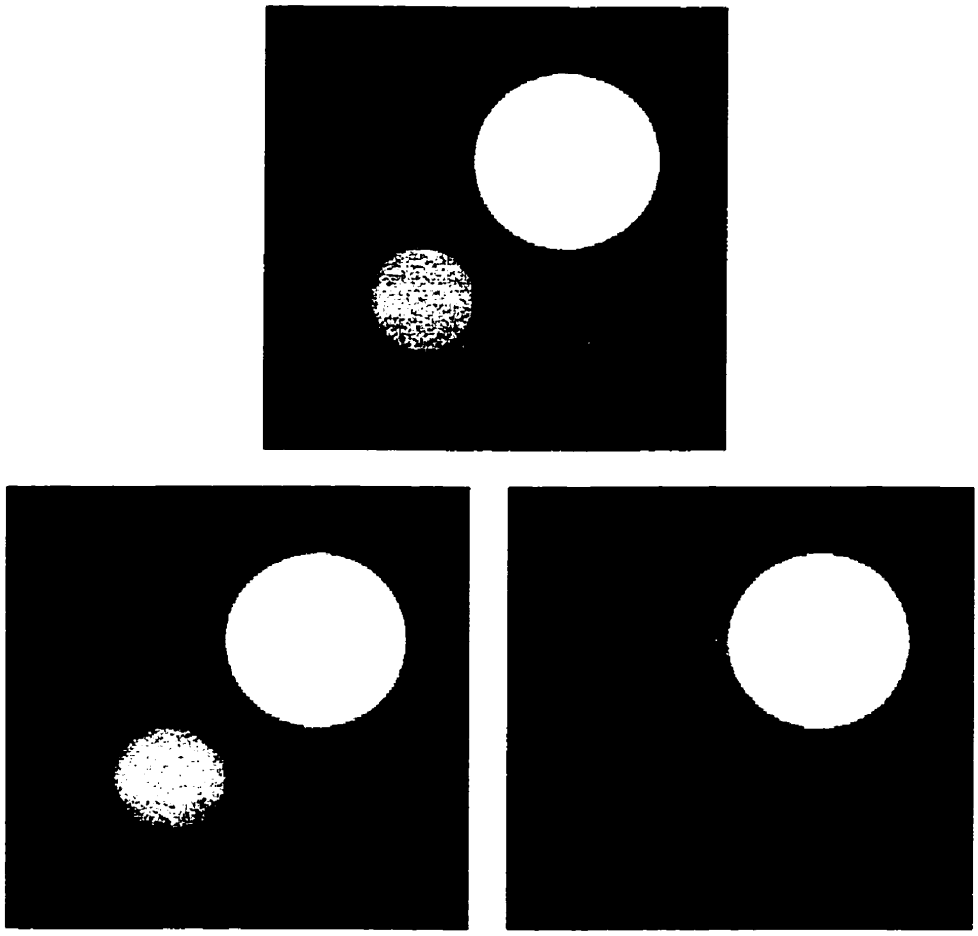

Figure 5.1: Synthetic conventional SE and RARE-mode SW-MRI images
The two disks of diameter 25% and 40% of the FOV with T_2 values of 40ms and 120ms, respectively, are shown at the top for a conventional Cartesian SE acquisition. On the bottom are the two different RARE-mode images for ESP=10ms and ETL=4 echoes (see text for details) with symmetric T_2-weighting at ESP_0=10ms appearing on the left and symmetric T_2-weighting at ESP_0=50ms appearing on the right. The images are normalized to unity at the brightest pixel, and all images are at the same windowing level.

acquisition sets, one may be able to determine $\tilde{\mathbf{E}}(\mathbf{k})$ and $\tilde{\mathbf{M}}_o(\mathbf{k})$ by solving for all the k-locations simultaneously. Only further work in this area will clarify these issues.

We present a proof by concept of Eq.(5.4) with a simple simulation carried out in the following manner. We generated a synthetic phantom consisting of two disks with diameters of 25% and 40% of the FOV, with T_2 values of 40ms and 120ms, respectively, as shown on the top of Figure 5.1. The Cartesian k-space data (128x128) were synthesized for each disk, and two RARE-mode acquisitions were synthesized with ESP=10ms and ETL=4 echoes. The k-space data included additive, zero-mean, Gaussian noise yielding an SNR of about 200 in the conventional SE image, and commensurately lower in the RARE-mode images.

The first RARE-mode acquisition had a symmetric T_2-weighting with ESP_0 set at 10ms, while the second acquisition also had a symmetric T_2-weighting but with ESP_0=50ms. The respective RARE-mode images are shown in Figure 5.1.

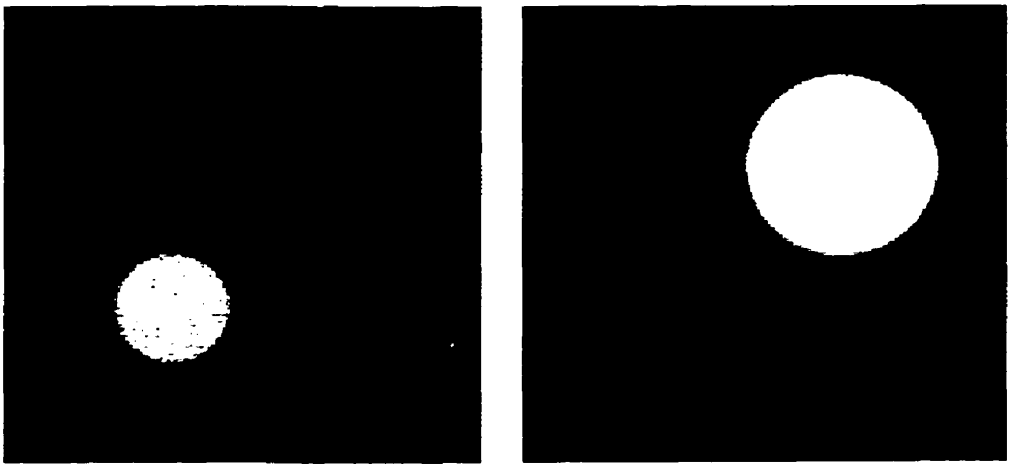

Figure 5.2: Isolated T_2 species from two RARE-mode acquisitions
The image on the left is the isolated T_2=40ms disk phantom of diameter 25% of the FOV, and that on the right is the T_2=120ms disk phantom. The images are normalized to unity at the brightest pixel, and both images are at the same windowing level.

In Figure 5.2, we show the normalized images of the two isolated T_2 species when demodulating the T_2-weighting using the proposed correction scheme. Note that we

used the proper T_2 values, namely 40ms and 120ms, in evaluating the $\widetilde{\mathbf{E}}$ matrix. Also note that the disks appear somewhat noisier than the respective conventional SE or RARE-mode images.

Clearly, there are many issues to be resolved: a noise propagation analysis, a sensitivity analysis of the $\widetilde{\mathbf{E}}$ matrix, the accuracy requirements of the T_2 values, the required number N_s to properly characterize the different T_2 species, and the optimal k-space RARE-mode trajectories, to name but a few. Still, these preliminary results are very promising. In fact, simulations with an infinite SNR (*i.e.* no noise) allow one to perfectly extract the N_s different T_2 species for T_2 as low as 5ms or so, and for the T_2 species separated by no more than 1ms from one another.

In general, MR k-space data contain both spatial *and* temporal information that are collapsed onto each other. Consequently, there is a tradeoff to be made. Furthermore, the spatial information alone arising from a particular choice of sampling trajectory offers a number of tradeoffs (resolution, SNR, aliasing, CNR, for example) which may affect the reconstructed image.

To optimize the image quality and minimize any image artifacts, one must understand both the fundamental aspects of the data acquisition process, and the MR physics associated with it. This is why we so painstakingly established firm theoretical foundations to analyze the sampling, reconstruction, and T_2 modulation effects. Although we dealt only with polar k-space acquisitions, the intention is that the concepts herein be applied to other MRI acquisition schemes to find an optimal compromise between spatial and temporal effects in the image.

In clinical applications, polar sampling and other non-rectilinear sampling schemes offer significant advantages in motion artifact and flow suppression. The image resolution, signal-to-noise ratio, aliasing, and amplitude modulation effects are all important considerations. The MR scientist is often trading off the spatial and temporal effects. With the T_2-weighting "demodulation" scheme proposed herein, it may be possible to separate these effects and better optimize the reconstructed MR images.

5.5 References

[1] J. Hennig, A. Nauerth, H. Friedburg, RARE imaging: a fast imaging method for clinical MR. *Magn. Reson. Med.* **3**, 823–833 (1986).

[2] R.N. Bracewell, A.R. Thompson, The main beam and ringlobes of an east-west rotation-synthesis array. *Astrophys. J.* **182**, 77–94 (1973).

Glossary

1D/2D	One-dimensional/two-dimensional
2DFT	Two-dimensional Fourier transform imaging (see SW-MRI)
B	Backprojection operator
$\mathbf{B}(\mathbf{r}, t)$	Magnetic field strength vector
Baseband	Effective FOV
BW	Analog-to-digital filter bandwidth
CBP	Convolution backprojection reconstruction algorithm
CC-MRI	Concentric circles MRI acquisition
CNR	Contrast-to-noise ratio
CT	Computed tomography
ESP	Echo spacing when imaging in RARE-mode
ETL	Echo train length when imaging in RARE-mode
$\mathcal{F}$	Fourier transform operator
$\mathcal{F}^{-1}$	Inverse Fourier transform operator
FFT	Fast Fourier transform
FID	Free induction decay
fMRI	Functional MRI
FOV	Field of view
FSE	Fast Spin Echo (same as RARE)
FT	Fourier transform
$\mathbf{G}(t)$	Magnetic field gradient vector
GRD	Gridding reconstruction algorithm

$\mathbf{k}$	Fourier domain spatial frequency coordinate
$I(\mathbf{r})$	Reconstructed MR image
IFT	Inverse Fourier transform
$J_0(r)$	Zeroth-order Bessel function of the first kind
$J_1(r)$	First-order Bessel function of the first kind
$\mathbf{m}(\mathbf{r}, t)$	Magnetization spin-density vector
$M(\mathbf{k}, t)$	Acquired MRI signal
MRI	Magnetic resonance imaging
MTF	Modulation transfer function
NEX	Number of averages in an MR experiment
NMR	Nuclear magnetic resonance
PR-MRI	Projection reconstruction MRI acquisition
PSF	Point spread function
$\mathbf{r}$	Image domain spatial coordinate whose Fourier conjugate is $\mathbf{k}$
RARE	Rapid Acquisition with Relaxation Enhancement
RF	Radiofrequency pulse
$\mathcal{Q}$	Spin integration operator
$\mathcal{S}_{cc}/\mathcal{S}_{pr}/\mathcal{S}_{sw}$	K-space signal fraction of RARE-mode CC-MRI/PR-MRI/SW-MRI
SE	Conventional spin echo MR acquisition
SNR	Signal-to-noise ratio
SW-MRI	Cartesian (spin-warp) MRI acquisition
T_1	Characteristic MR spin-lattice relaxation time
T_2	Characteristic MR spin-spin relaxation time
TE	Echo time
TR	Repetition time
TSE	Turbo Spin Echo (same as RARE)
UWO	University of Western Ontario

IMAGE EVALUATION
TEST TARGET (QA-3)

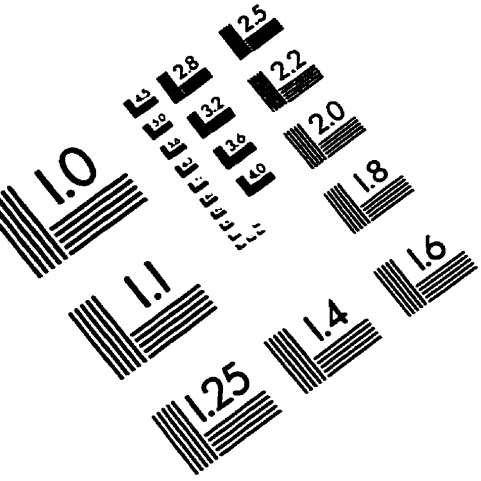

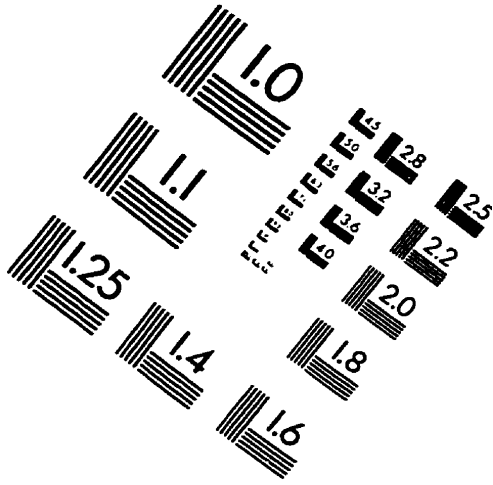

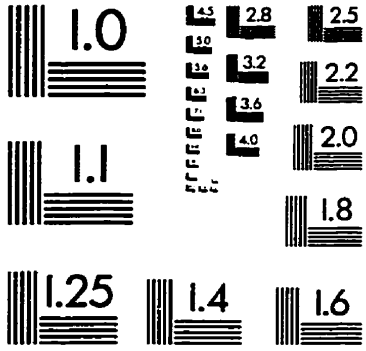

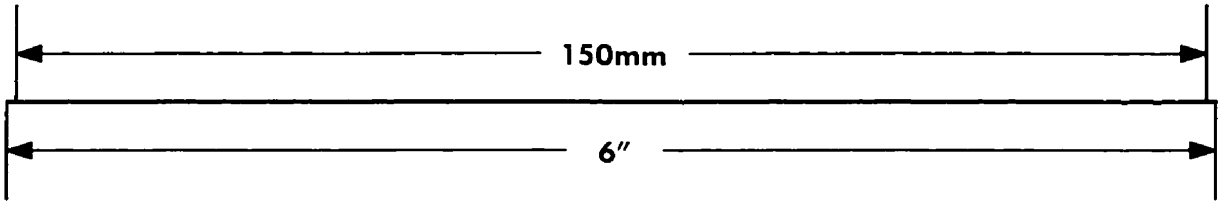

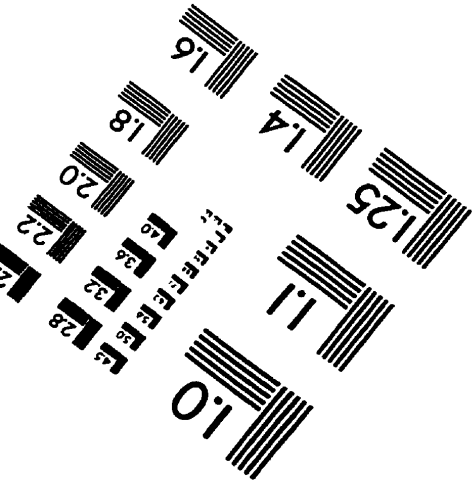

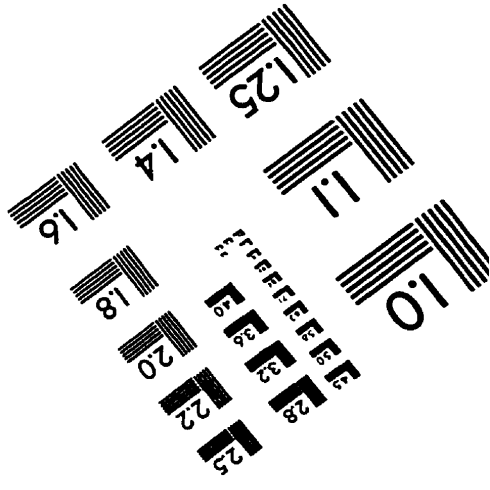

APPLIED IMAGE, Inc
1653 East Main Street
Rochester, NY 14609 USA
Phone: 716/482-0300
Fax: 716/288-5989